CryoEM structures of the human CLC-2 voltage gated chloride channel reveal a ball and chain gating mechanism

Mengyuan Xu[1], Torben Neelands[1], Alexander S. Powers[2.3,4,5], Yan Liu[6], Steven D. Miller[2], Grigore Pintilie[7], J. Du Bois[2], Ron O. Dror[1,3,4,5], Wah Chiu[6,7], Merritt Maduke[1]

[1]Department of Molecular and Cellular Physiology, Stanford University, Stanford, CA 94305

[2]Department of Chemistry, Stanford University, Stanford, CA 94305

[3]Department of Computer Science, Stanford University, Stanford, CA 94305

[4]Department of Structural Biology, Stanford University, Stanford, CA 94305

[5]Institute for Computational and Mathematical Engineering, Stanford University, Stanford, CA 94305

[6]Division of CryoEM and Bioimaging, SSRL, SLAC National Accelerator Laboratory, Stanford University, Menlo Park 94025

[7]Department of Bioengineering and Department of Microbiology and Immunology, Stanford University, Stanford, 94305

Correspondence:

Dr. Merritt Maduke

279 Campus Drive West

Stanford, CA 94035

Tel: 650-723-9075

Email: maduke@stanford.edu

Keywords: chloride channel, cryo-electron microscopy, electrophysiology

ABSTRACT:

CLC-2 is a voltage-gated chloride channel that contributes to electrical excitability and ion homeostasis in many different mammalian tissues and cell types. Among the nine mammalian CLC homologs, CLC-2 is uniquely activated by hyperpolarization, rather than depolarization, of the plasma membrane. The molecular basis for the divergence in polarity of voltage gating mechanisms among closely related CLC homologs has been a long-standing mystery, in part because few CLC channel structures are available, and those that exist exhibit high conformational similarity. Here, we report cryoEM structures of human CLC-2 at 2.46 – 2.76 Å, in the presence and absence of the potent and selective inhibitor AK-42. AK-42 binds within the extracellular entryway of the Cl^--permeation pathway, occupying a pocket previously proposed through computational docking studies. In the apo structure, we observed two distinct apo conformations of CLC-2 involving rotation of one of the cytoplasmic C-terminal domains (CTDs). In the absence of CTD rotation, an intracellular N-terminal 15-residue hairpin peptide nestles against the TM domain to physically occlude the Cl^--permeation pathway from the intracellular side. This peptide is highly conserved among species variants of CLC-2 but is not present in any other CLC homologs. Previous studies suggested that the N-terminal domain of CLC-2 influences channel properties via a “ball-and-chain” gating mechanism, but conflicting data cast doubt on such a mechanism, and thus the structure of the N-terminal domain and its interaction with the channel has been uncertain. Through electrophysiological studies of an N-terminal deletion mutant lacking the 15-residue hairpin peptide, we show that loss of this short sequence increases the magnitude and decreases the rectification of CLC-2 currents expressed in mammalian cells. Furthermore, we show that with repetitive hyperpolarization WT CLC-2 currents increase in resemblance to the hairpin-deleted CLC-2 currents. These functional results combined with our structural data support a model in which the N-terminal hairpin of CLC-2 stabilizes a closed state of the channel by blocking the cytoplasmic Cl^--permeation pathway.

INTRODUCTION

Ion transport across the cell membrane establishes and exploits ion gradients to store energy and regulate electrical signaling. Ion transport is catalyzed by two classes of membrane proteins: ion channels and active transporters. The CLC "Chloride Channel" family encompasses both major ion-transport mechanisms: half of the CLC homologs are electrodiffusive chloride (Cl^-) channels, and half are secondary active transporters that stoichiometrically exchange Cl^- for protons (H^+) (Jentsch and Pusch, 2018). The occurrence of two mechanisms in one family suggests they operate by variations on a common theme (Miller, 2006), and experimental results revealed that CLC channels are "broken" transporters (Lisal and Maduke, 2008).

In both CLC channels and transporters, a conserved glutamate residue referred to as the "gating glutamate" (E_{gate}) plays a central mechanistic role. High resolution CLC transporter structures show that this residue can adopt four different conformations (Dutzler et al., 2002; Dutzler et al., 2003; Feng et al., 2010; Chavan et al., 2020; Schrecker et al., 2020) (**Figure 1A**), which contribute to the Cl^-/H^+ exchange mechanism (Accardi and Miller, 2004; Feng et al., 2012; Chavan et al., 2020; Leisle et al., 2020). Due to the small number of CLC channel structures relative to transporters, characterization of the central role for the E_{gate} residue in CLC channels has primarily relied on extensive functional studies of channel gating rather than observed E_{gate} side chain conformations (Jentsch and Pusch, 2018). The first CLC channel structure reported was of bovine CLC-K (Park et al., 2017), a kidney-expressed homolog that is the lone CLC homolog lacking the E_{gate} (Kieferle et al., 1994). The only other CLC channel structures reported prior to 2023 are of the human CLC-1: one of these cryoEM structures shows E_{gate} in the "out" position (Park and MacKinnon, 2018) while the other lacked density for E_{gate} (Wang et al., 2019). The E_{gate} "out" position was originally posited to be exclusive to the CLC channel homologs, as its positioning off to the side widens the Cl^--permeation pathway and, in CLC-1, results in a continuous pathway (Park and MacKinnon, 2018). Such a continuous pathway precludes exchange coupling (Jardetzky, 1966; Miller, 2021). The open Cl^--permeation pathway in the CLC-1 structure is consistent with the known functional properties of CLC-1 in the absence of an applied transmembrane

voltage. CLC-1 is a voltage-gated channel that is predominantly in the open state at zero mV (Altamura et al., 2020) (**Figure 1B**). At negative transmembrane voltages that favor CLC-1 closing, the E_{gate} sidechain presumably moves to either the “middle” or “down” positions, or both, to occlude the channel pore.

CLC-2, like CLC-1, is a voltage-gated channel, but with opposite voltage dependence, opening instead of closing in response to hyperpolarization (Thiemann et al., 1992; Wang et al., 2017). CLC-2 chloride channels are expressed in every mammalian organ, where they play diverse physiological functions (Thiemann et al., 1992; Lein et al., 2007; Duan, 2013; Stolting et al., 2014; Jentsch and Pusch, 2018). Perturbation of CLC-2 function is associated with human disease including leukodystrophies (Jentsch and Pusch, 2018), blindness (Xu et al., 2023), primary aldosteronism (Fernandes-Rosa et al., 2018; Scholl et al., 2018), and atrial fibrillation (Hansen et al., 2020). Despite their importance in human physiology, our understanding of CLC-2 molecular and physiological mechanisms is incomplete. A mystery concerning CLC-2 is why electrophysiological recordings of natively expressed channels reveal tremendous variation in voltage-dependent gating. CLC-2 currents are typically inwardly rectifying and activated by hyperpolarization, but the kinetics and degree of rectification are highly variable (Bosl et al., 2001; Jentsch and Pusch, 2018). In some cases, this variability is understood – for example interactions between CLC-2 and the astrocytic GlialCAM protein yields voltage-independent currents (Jeworutzki et al., 2012; Maduke and Reimer, 2012). Yet many questions about CLC-2 gating remain.

Like CLC-1, CLC-2 gating depends critically on E_{gate} (Niemeyer et al., 2003; Cederholm et al., 2010). At zero mV, CLC-2 is predominantly in the closed state (Stolting et al., 2013; Stolting et al., 2014; Jentsch and Pusch, 2018), presumably with E_{gate} blocking the pore. Such pore localization for E_{gate} was modeled in a recent CLC-2 cryoEM structure (Ma et al., 2023); however, experimental density for the sidechain was lacking, and therefore the precise structure of this gate remains uncertain (**Figure 1B**). Structures with improved resolution will be crucial to understanding CLC-2 gating, which involves interactions between E_{gate}, Cl^- and H^+, with differential effects of external vs internal ions (Pusch et al.,

1999; Niemeyer et al., 2003; Sanchez-Rodriguez et al., 2010; Sanchez-Rodriguez et al., 2012; De Jesus-Perez et al., 2016). In addition to the E_{gate} mechanism, a “ball-and-chain” gating mechanism, in which the tethered N-terminus blocks the pore, has been proposed for CLC-2 (Grunder et al., 1992). However, this idea has been controversial (Varela et al., 2002) and the mechanism by which mutations in the N-terminal domain influence gating remains unknown. Because a structural foundation for understanding CLC-2 gating has been lacking, we determined cryoEM structures of CLC-2, in the presence and absence of the selective inhibitor AK-42 (Koster et al., 2020). The structures and complementary electrophysiology data presented here provide atomic insight into an N-terminal hairpin gating mechanism for CLC-2 channels.

RESULTS

Overview of cryoEM structure determination

Human CLC-2 (hCLC-2) protein was purified from cultured HEK293 GnTI$^-$ cells and further examined by cryoEM single particle analysis. Selected two-dimensional class averages showed a clear transmembrane domain embedded in a detergent micelle and features indicating an intracellular domain. Further refinement revealed a well-resolved transmembrane (TM) domain density at 2.46 Å, “CLC2-TM" (**Figure 2; Figure 2 - figure supplements 1-3**). Density for the C-terminal intracellular domain (CTD) is less well resolved. Such relatively weak density for the CTD relative to the TM domain was also observed in the cryoEM analysis of human CLC-1 (Park and MacKinnon, 2018; Wang et al., 2019), which is hCLC-2’s closest homolog. The CTD of CLC-0, a CLC-1 ortholog from *Torpedo mamorata* (Steinmeyer et al., 1991) displays large movements in spectroscopic studies (Bykova et al., 2006; Alioth et al., 2007). Thus, conformational flexibility in the CTD appears to be a shared feature within this branch of the CLC family. To further characterize CTD map density, 3D classification was performed. Amongst ten 3D classes identified, two showed significantly improved density for the CTD. With non-uniform refinement and further local refinement, we determined two conformations of CLC-2 structures at 2.75 and 2.76 Å, respectively (**Figure 2 - figure supplement 2**).

Structure of the transmembrane domain

The TM region of CLC-2 displays a typical CLC family symmetric homodimeric structure, with each subunit containing an independent Cl^- pathway (**Figure 2A, B**). In the cryoEM map, clear density for the E_{gate} residue (E205 in CLC-2) reveals it occupying the "down" position, at the S_{cen} Cl^- binding site (**Figure 2C**). This downward E_{gate} positioning has previously been observed only in the x-ray crystallographic structure of the *C. merolae* CLC transporter homolog (cmCLC) (Feng et al., 2010), but not in any CLC channel homolog (**Figure 2 – figure supplement 4A,B**). In the recent CLC-2 structure by Ma et al., E_{gate} lacked density and was modeled in two different conformations (Ma et al., 2023) (**Figure 2 – figure supplement 4C**). Our cryoEM map also reveals a density feature at the S_{ext} site, consistent with a bound Cl^- ion (**Figure 2C**). The ion at the S_{ext} site is stabilized by surrounding backbone nitrogen atoms, a characteristic feature of CLCs (Dutzler et al., 2003; Picollo et al., 2009; Feng et al., 2010; Park and MacKinnon, 2018).

Two lines of evidence point to the structure representing a closed state, as expected at zero mV. First, E_{gate} physically occupies the S_{cen} Cl^- binding site (**Figures 1A, 2C**), thus blocking the permeation pathway. Second, we used Caver (Chovancova et al., 2012) to detect pathways through the protein. A continuous pathway through the protein could only be detected with a very small probe radius of 0.5 Å. In this case, the route detected follows the canonical Cl^- transport pathway from the extracellular side to S_{cen}, but then circumnavigates E_{gate} to reach the intracellular pathway (**Figure 3A, Video 1**). The pinch point of ~0.7 Å near the E_{gate} residue is too narrow for a Cl^- ion and thus indicates a closed conformational state. The CLC-2 pathway is constricted compared to that in CLC-1, where the location of E_{gate} in the "out" position permits a wider Cl^- diffusion pathway (**Figure 3B, Video 2**). Close-up views of the canonical Cl^- pathway in CLC-2 and CLC-1 are shown in **Figure 3 – figure supplement 1.** The two lines of evidence just discussed – E_{gate} at the S_{cen} site and the Caver pinch point – argue that E_{gate} is in the deprotonated state: (1) the location of E_{gate} in an anion-binding site is most consistent with the sidechain being negatively charged; (2) neutralization of E_{gate} leads to an

open-channel phenotype (Niemeyer et al., 2003; de Santiago et al., 2005), which is incompatible with the observed pinched-closed pore.

At the CLC inner-gate region, near conserved residues Tyr_C (Y553) and Ser_C (S162), the canonical (primary) Cl^-permeation pathway is similar for CLC-2 and CLC-1 and wider than that seen in the CLC transporters (**Figure 3 – figure supplement 2A, B, Video 3**). CLC-2 also displays a bifurcated pore, with a secondary pathway to the intracellular side, distinct from the primary pathway common to CLC family members. The secondary pathway is shared with CLC-1 but not seen in other CLC homologs of known structure. While the functional role of this distinctive secondary pore is not yet known, it is intriguing to note it is located near the region thought to act as a conduit for H^+ in the CLC transporters (**Figure 3 – figure supplement 2C**).

Two conformations of the intracellular domain

All eukaryotic CLCs contain a pair of “cystathionine β-synthase” (CBS) domains in their intracellular C-terminal domain (Jentsch and Pusch, 2018). CBS domains are found in a wide variety of functionally unrelated protein families, in all kingdoms of life, where they serve to regulate the activity of the attached protein (Ereno-Orbea et al., 2013; Anashkin et al., 2017). In the CLCs, mutations in or near the CBS domains alter channel gating and are associated with human disease, including myotonia, Dent’s disease, Bartter syndrome, osteopetrosis, leukoencephalopathy, retinal degeneration, lysosomal storage disease, and neurodevelopmental disorders (Estevez et al., 2004; Giorgio et al., 2017; Jentsch and Pusch, 2018; Guo et al., 2019; Nicoli et al., 2019; Altamura et al., 2020; Gianesello et al., 2020; Duncan et al., 2021; Zifarelli, 2022; Palmer et al., 2023; Xu et al., 2023). Structurally, the CLC CBS domains interact across subunits, forming dimers of dimers and thus increasing the overall interaction area of the homodimer (Feng et al., 2010; Park et al., 2017; Park and MacKinnon, 2018; Wang et al., 2019; Schrecker et al., 2020). Structural rearrangement of the C-terminal domains is thought to occur during channel gating (Yamada et al., 2016; Jentsch and Pusch, 2018) and has been observed spectroscopically (Bykova et al., 2006; Ma et al., 2011), but no rearrangements have yet

been observed at high resolution. The physiological relevance of C-terminal domain rearrangements is suggested by disease-causing mutations that alter channel gating (Estevez et al., 2004; Brenes et al., 2023).

During the 3D classification data processing with a C1 reconstruction (no symmetry imposed), two distinct conformations were separated from the same CLC-2 dataset (**Figure 2 - figure supplement 2**). Structural comparison of these two classes reveals that they are very similar in the transmembrane domain, with RMSD of 0.58 Å and 0.42 Å for the two subunits. The main structural differences occur at the intracellular domain, with one class exhibiting a symmetric arrangement and the other, asymmetric. These two conformations are named as CLC2-CTDsym and CLC2-CTDasym, respectively (**Figure 4, Figure 4 - figure supplements 1,2**). In both classes, the CBS domains can be fit to the density; however residues 645-743 in the CLC-2 C-terminal domain are not resolved and thus are omitted from the models and from the Q-score calculation (Pintilie et al., 2020) (**Figure 4 – figure supplement 1**). In the asymmetric arrangement (CLC2-CTDasym), one of the CTDs rotates toward the TM region approximately 35° relative to the conformation in the symmetric structure (**Figure 4B**). Structural comparison focused on individual CTDs within the two classes reveals low RMSD values (~1 Å), which indicates that the CTD undergoes a rigid body movement to accomplish the conformational change (**Figure 4C**, **Video 4**). Molecular dynamics (MD) simulations confirm conformational dynamics consistent with a domain rotation (**Figure 4 – figure supplement 3**). In both structures, the orientation of the CTD relative to the membrane is substantially different from that observed in other CLC structures (**Figure 4 - figure supplement 4**).

The hairpin structure corresponds to the N-terminal region

Another new feature of the determined CLC-2 structure is a hairpin density blocking the main Cl^- pathway on the intracellular side (**Figure 4A**). This feature is not continuous with any other protein density in the map. In theory, such density could arise from a protein sequence on CLC-2 (from the

unstructured N- or C-terminal regions) or from a separate protein carried along in the purification. Given the history of studies on CLC-2 gating, we first considered the CLC-2 N-terminal region.

Shortly after the initial cloning of CLC-2 (Thiemann et al., 1992), experiments on CLC-2 expressed in *Xenopus* oocytes demonstrated that deletion of an 18-residue segment of the N-terminus yielded a constitutively open channel, lacking the characteristic voltage-dependent gating of CLC-2, and that transplantation of this segment to the C-terminal domain restored gating (Grunder et al., 1992). Further, mutation of certain residues in the transmembrane domain (at a putative “receptor” site for the N-terminal blockade) also yielded an open-channel phenotype (Jordt and Jentsch, 1997). Based on these results, it was argued that CLC-2 has a “ball-and-chain” type gating mechanism reminiscent of that occurring in the *Shaker* potassium channel (Zagotta et al., 1990). However, experiments performed using the inside-out patch clamp configuration (Pusch et al., 1999) or using whole-cell recording with CLC-2 expressed in mammalian cells (Varela et al., 2002) failed to recapitulate the gating phenotype and called into question a ball-and-chain mechanism. Thus, while mutations in the N-terminus of CLC-2 influence gating, the precise mechanism-of-action has been uncertain.

Our cryoEM map allowed continuous modeling of the CLC-2 sequence starting from the first TM helix (residue 88). The lack of sufficient density for modeling residues 1-87 suggests that the N terminal cytoplasmic region of CLC-2 is intrinsically disordered. However, our observation of a resolvable hairpin density at the intracellular pore, together with the previous hypothesis of N-terminal ball-and-chain gating for CLC-2, prompted us to consider whether the hairpin density corresponds to N-terminal residues. We tested several candidate fragments from the CLC-2 N-terminal region and found that the hairpin density fits perfectly with residues corresponding to 14-28 (**Figure 5A**). Inspection of the Q-score validation plot for these residues shows they have higher values than the Q-score expected for the corresponding resolution (**Figure 5B**), which indicates reliable model building at this resolution (Pintilie et al., 2020). In contrast, the best-fitting peptide from disordered regions of the C-terminal cytoplasmic region yielded poorer Q scores, generally lower than the Q-score expected for the corresponding resolution (**Figure 5 – figure supplement 1**). The N-terminal residues corresponding to

the hairpin peptide are conserved throughout the mammalian CLC-2 homologs and partially conserved in *Drosophila* CLC-2 (**Figure 5 - figure supplement 2**).

Interestingly, the presence of the N-terminal hairpin is associated with conformational changes in the CTD and TM domains. In CLC2-CTDsym, N-terminal density was observed on both subunits. In CLC2-CTDasym, only the subunit whose CTD adopts the "symmetric" orientation (seen in CLC2-CTDsym) contains the hairpin density; in the subunit with the rotated CTD, no hairpin density is observed (**Figure 4, Figure 5A**). Along with the absence of hairpin density, the subunit with the rotated CTD exhibits a difference in the linker connecting transmembrane helices J and K, which is poorly resolved and insufficient for model building. In contrast, the subunits with the hairpin density contain reliable density in the JK-linker region, allowing confident modeling of an alpha helix ("JK-helix", **Figure 5A**). This observation suggests that the JK-helix stabilizes the N-terminal hairpin peptide. Indeed, residues on the JK-helix interact directly with residues at the peptide's hairpin turn (**Figure 5C**). Interactions with other regions in the TM domain (near helices C, D, J, and R) appear to further stabilize the hairpin in its binding site. In addition, the negative surface potential of the hairpin likely contributes to its interaction with the positive TM domain (**Figure 5 – figure supplement 3; Video 5**). MD simulations help separately validate the assignment and stability of the hairpin: in MD simulations initiated from the structure, we found that the N-terminus remained tightly associated with the channel in all simulations (**Figure 5 – figure supplement 4**).

Functional support for pore block by the N-terminal hairpin structure

The hairpin structure appears to directly block the pore (**Figure 5 – figure supplement 5**). To evaluate the potential functional effect of pore block by the N-terminal hairpin, we performed whole-cell patch clamp recording on CLC-2, both WT and a deletion mutant lacking the hairpin residues ("Delta-N"), expressed in CHO cells. Delta-N CLC-2 exhibits currents that display less rectification and faster activation kinetics than WT CLC-2 (**Figure 6A-B, Figure 6 – figure supplement 1**). This gating phenotype is intermediate between the non-rectifying phenotype of N-deletion constructs from whole-

cell recordings in oocytes (Jordt and Jentsch, 1997) and the highly rectifying phenotype from whole-cell recordings in HEK 293 cells (Varela et al., 2002). The Discussion section addresses the variability observed in CLC-2 current recordings. As was reported for N-deletion currents in oocytes, our delta-N currents are substantially larger than WT currents, ~6-fold on average when identical transfection conditions are used (**Figure 6C**). This difference cannot be explained by a difference in plasma-membrane expression, as surface biotinylation experiments revealed that expression levels of the two constructs are within 30% of one another (**Figure 6D, E**).

Strikingly, WT but not delta-N CLC-2 currents “run up” during recording sessions. In patch-clamp recording experiments, the term “run-up” describes a progressive increase in current that occurs after the initial measurement. To quantify CLC-2 run-up, we developed the following protocol: (1) on acquisition of whole-cell recording mode, an initial voltage-family of currents was recorded, as in **Figure 6A**; (2) from a holding potential of 0 mV, a single 1-s test pulse to -100 mV was repeated every 5 seconds to monitor time-dependent changes in current amplitude over 5 minutes, after which a second voltage-family of currents was recorded; (3) 300 nM AK-42 was added to selectively block all CLC-2 current (Koster et al., 2020), and the steady state inhibition current was used for leak subtraction. In contrast to chloride-channel inhibitors historically used in electrophysiological experiments (Sepela and Sack, 2018), AK-42 is potent and highly selective for CLC-2 over other anion channels (Koster et al., 2020). Representative current traces and summary data for this set of experiments are shown in **Figure 6F, G**; individual I-V traces are shown in **Figure 6 – figure supplement 1**. The increase in WT but not delta-N CLC-2 currents over time is consistent with an “unblocking” of the pore by release of the N-terminal hairpin peptide.

The increase in WT currents is accompanied by an apparent decrease in channel rectification, towards the level displayed by Delta-N CLC-2. WT CLC-2 currents recorded in heterologous and native expression systems are generally highly inwardly rectifying. Analogous to a rectifier in an electrical circuit, WT CLC-2 acts as a directional current valve, allowing much larger absolute currents to flow at negative membrane potentials compared to positive ones. At the beginning of each recording, our WT

CLC-2 currents display such inward rectification, but this characteristic appears to diminish during five minutes of repeated voltage pulsing to -100 mV, as substantial currents at positive voltages appear. For the experiment shown in **Figure 6F**, the steady-state current at +80 mV increases from 161 pA to 902 pA, almost six-fold, compared to a 2.4-fold increase at -100 mV. This observation is surprising because WT CLC-2 has been characterized as passing little to no current at positive voltages (Park et al., 1998; Arreola et al., 2002). We initially considered that the increase in current at +80 mV could be due to the patch-clamp seal becoming leaky over time or that a background channel is being activated; however, such 'leak' currents would not be expected to be blocked by the small molecule inhibitor AK-42, which is highly selective for CLC-2 over all other CLCs and anion channels (Koster et al., 2020). AK-42 block of the augmented +80 mV currents seen at the end of each WT CLC-2 recording supports the idea that the hairpin peptide may contribute to the inward rectification of CLC-2 (**Figure 6F**, **Figure 6 – figure supplement 2**).

AK-42 bound structure

AK-42's selectivity empowered our biophysical studies of CLC-2 and will also be invaluable for studies of CLC-2's physiological function. We determined the structure of CLC-2 in complex with AK-42 (**Figure 7**). While the TM domain could be resolved to 2.7 Å, the CTD exhibited poor density compared to the apo sample and did not allow us to confidently model the CTD when masking the whole protein for refinement. To improve the density quality, we masked the CTD only for refinement; this masking provided an acceptable density map at 4 Å and allowed us to confidently dock the CTD from apo structure (**Figure 7 – figure supplements 1-4**).

Like the apo CLC-2 structure, the TM domain of CLC2-TM-AK42 is well-resolved with clear densities for AK-42 and for CLC-2 sidechains, including the E_{gate} sidechain (**Figure 7 – figure supplements 5,6**). The overall density for CLC2-TM-AK42 is very similar to that observed in apo CLC-2, but with an extra density that fits very well to the AK-42 molecule (**Figure 7B, Video 6**). Residues in the AK-42 binding pocket exhibit little conformational change between the apo and AK-42 bound CLC-2

structures. The exception is residue M460, which moves ~3 Å to avoid a clash with AK-42's phenyl ring (**Figure 7 - figure supplement 7**). Located at the extracellular side of Cl^- pathway, the bound AK-42 appears to directly block Cl^- permeation (**Figure 7C**). This AK-42 binding pocket is the same as observed in the docking prediction we previously made using a CLC-2 homology model (Koster et al., 2020). In that docking study, the top docking poses varied in detail, and therefore the specific interactions were not certain, but the general position of the binding site is confirmed by our cryoEM structure. Two conformations were found to fit the density well with the carboxyl group on opposite sides. They were tested using the Quantum Mechanical Restraints (QMR) method (Liebschner et al., 2023); one had significantly lower energy (~17 kcal/mol) and strain on the ligand (10.2 kcal/mol), considering the ligand and nearby residues only. For the lower energy conformation, the Q-scores of AK-42 in the map are 0.74 and 0.76 in the two subunits, respectively. Both are higher than the expected Q-score at this resolution (0.64), which indicates a good fit of AK-42 to the cryoEM density (Pintilie et al., 2020). A similar AK-42 binding pose was observed in another recently published structure of CLC-2 (Ma et al., 2023). The RMSD between our CLC2-TM-AK42 structure and that of Ma et al. is 0.655 Å, and the RMSD between the apo TM structures is 0.756 Å .

In the binding site, AK-42's phenyl ring nestles into a hydrophobic pocket lined by F306, F463, F459, M460 and L524 (**Figure 7B**). The carboxyl group of AK-42 forms hydrogen bonds with the side chain of S392 and backbone of K394 (**Figure 7B**). These polar interactions are consistent with mutagenesis data. At 30 nM AK-42, inhibition of S392A is reduced ~50% compared to WT, consistent with disruption of the observed hydrogen bond, while inhibition of K394A is not significantly different from WT, consistent with a backbone rather than a side-chain interaction (Koster et al., 2020; Ma et al., 2023). A third hydrogen bond – between K204 and the pyridine nitrogen of AK-42 – also contributes to AK-42's stability in the binding pocket. A pivotal role for the pyridine nitrogen was discovered during the development of AK-42, where it was found that inhibitor potency is increased by over two orders of magnitude by addition of a nitrogen at this position but not by addition of a nitrogen at any other position in the ring (Koster et al., 2020). The interaction of this pyridine nitrogen with K204 is supported

by mutagenesis data, which shows that inhibition of K204M and K204R (K210M and K210R in rat CLC-2) is reduced ~3-fold compared to WT (Koster et al., 2020; Ma et al., 2023). The distance between the nitrogen atoms on K204 and AK-42 is 3.6 Å, within acceptable hydrogen bond distance, while the distances between K204 and any other atoms on AK-42 are too far to allow hydrogen bond formation.

Notably, density corresponding to the N-terminal hairpin structure is not seen in the AK-42 bound structure. After intensive 3D classification, only very minimal hairpin density was observed in a few classes. It thus appears that the majority of AK-42 bound CLC-2 particles have a flexible N-terminus that is not blocking the Cl^- pathway. There is no obvious explanation for this difference compared to the apo structure. The orientation of the CTD in the AK-42 bound structure is the same as observed in the apo structure that shows N-terminal hairpin binding; the density for the J-K helix is weaker than in the apo dataset, but still sufficient to allow modeling of the helix. The TM regions also appear similar. To scrutinize for subtle conformational changes, we calculated a distance difference matrix (Nishikawa, 1972) comparing CLC2-TM and AK-42 bound CLC-2 (**Figure 7 – figure supplement 8**). The minor changes observed do not readily suggest a structure-based hypothesis for the observed difference in N-terminus. It could be that AK-42 inhibits dynamics that are essential for hairpin peptide binding.

DISCUSSION

Our CLC-2 channel structures display quintessential CLC characteristics, including a homodimeric arrangement of subunits, transmembrane domains composed of 18 helical segments, and conserved residues surrounding central anion-binding sites S_{ext} and S_{cen} (Jentsch and Pusch, 2018). At 2.5 Å resolution, we observe clear density for critical features, including a Cl^- ion at S_{ext} and the E_{gate} residue at S_{cen} (**Figure 2C**). In this position, E_{gate} blocks the pore, generating a closed conformational state – as expected for CLC-2 at 0 mV (**Figure 1**).

AK-42 binding site and inhibition potency

A distinctive feature of AK-42—unique amongst CLC inhibitors—is its high selectivity for CLC-2 versus other channels, transporters, and receptors (Koster et al., 2020). The IC_{50} for inhibition of CLC-2 by AK-42 (17 nM) is more than four orders of magnitude lower than the IC_{50} for inhibition of CLC-1, CLC-2's closest homolog. CLC-1 and CLC-2 are 50% identical overall, and within the AK-42 binding site only five residues are different (**Figure 7 – figure supplement 9**). Structural comparison of CLC-1 (PDB ID:6coy) with CLC2-AK42 reveals that these five residues (I112 (S139), S392 (M419), Q393 (P420), K394 (R421), and L397 (I424)) exhibit only relatively minor differences in backbone conformation. While the S392 side chain contributes to a hydrogen-bond interaction with AK-42 (**Figure 7B)**, which M419 in CLC-1 cannot provide, this interaction alone cannot explain the four orders of magnitude difference in AK-42 potency. Indeed, the mutation S392A reduces inhibition by 30 nM AK-42 only ~3-fold (Ma et al., 2023). Similarly, Q393P (Q399P in rat CLC-2) reduces inhibition by less than five-fold (Koster et al., 2020; Ma et al., 2023). A steric clash between F279 (F252 in CLC-2) and the benzyl substituent in AK-42 may also contribute to the lack of potency of AK-42 towards CLC-1 (**Figure 7 - figure supplement 9**). In CLC-2, this same residue (F252) is shifted away from the binding site, opening a sub-pocket that the benzyl group occupies. This difference is not simply induced by AK-42 binding, as F252 is also shifted away from the binding site in the CLC-2 apo structure. In the structure-activity relationship studies used to develop AK-42, the benzyl substituent increased selectivity approximately 5-fold (Koster et al., 2020), thus supporting the significance of this interaction to selectivity. Unfortunately, this hypothesis cannot be tested through mutagenesis experiments due to the extremely low expression of F252 mutants (Ma et al., 2023).

The pathway from the extracellular solution appears sufficiently wide for AK-42 to worm its way into the binding site (**Figure 7C**). It is not yet known whether this pathway becomes wider in the CLC-2 open state. Intriguingly, the lack of density for the hairpin peptide in the AK-42-bound structure suggests that hairpin and AK-42 binding may be mutually exclusive. Studies to evaluate state-dependence of AK-42 inhibition and of hairpin block will be valuable for understanding CLC-2 conformational change and gating dynamics.

E_{gate} conformation

CLC-2 is the first CLC channel homolog to be seen in a closed conformational state. While it was expected that E_{gate} would localize to the Cl^--permeation pathway in the closed conformational state, it was not certain whether the S_{ext} or S_{cen} site would be preferred. The structure of CLC-1 provides an argument that S_{ext} might be preferred. In CLC-1, anion density is observed at S_{ext} but not at S_{cen} (Park and MacKinnon, 2018). It was hypothesized that the lack of density at S_{cen} in CLC-1 may reflect a reduced anion-binding affinity that contributes to increased Cl^- conduction (higher Cl^- throughput) by the CLC channels compared to the transporters (Park and MacKinnon, 2018), as all structures of WT CLC transporters show anion density (either Cl^- or E_{gate}) at both S_{ext} and S_{cen} (Dutzler et al., 2003; Chavan et al., 2020; Schrecker et al., 2020). If true for all channels, one might expect E_{gate} in CLC-2 to occupy S_{ext} rather than S_{cen} in the closed state. However, we do not observe this occupancy, and therefore the decreased anion affinity at S_{cen} is not the universal reason for increased Cl^- conduction in CLC channels relative to the transporters. Instead, our CLC-2 structure is consistent with the predictions made by Arreola and colleagues, who used homology modeling in concert with detailed electrophysiological analyses to conclude that the CLC-2 gate is formed by the E_{gate}-Tyr_C pair at S_{cen} (De Jesus-Perez et al., 2021). Additional experiments, to directly measure anion affinity and to determine structures of CLC-2 and CLC-1 in both open and closed conformations are needed to better understand these channels' similarities and differences.

CTD conformation

CLC-2 is also the first CLC in which two conformations of the CTD are observed. While many previous studies indicate that conformational change of the CTDs plays a critical role in CLC gating (Jentsch and Pusch, 2018; Grieschat et al., 2020), the mechanistic details are currently fuzzy. Unlike other CLC variants, CLC-2 can still conduct Cl^- when its CTD is removed; however, the modified gating kinetics of this mutant do suggest a role of the CTD in regulating channel function (Garcia-Olivares et

al., 2008). The impact of mutations in various regions of the CLC-2 CTD further supports its role in gating (Yusef et al., 2006; Paul et al., 2007; Stolting et al., 2013; Giorgio et al., 2017), as do the effects of ATP binding on channel kinetics (Saint-Martin et al., 2009; Stolting et al., 2013). While we do not see ATP bound in our structure (none was added to the protein preparation), the binding-site region overlaps reasonably well with the structure of the ATP-bound CLC-5 CTD (**Figure 4 – figure supplement 5**). The physiological significance of an intact CTD is underscored by CTD mutations and truncations of CLC-2 that occur in human leukoencephalopathy and retinal degeneration (Giorgio et al., 2017; Guo et al., 2019; Xu et al., 2023). It is likely that the structural rearrangement we observe strongly influences channel gating: the CTD upward hinge rotation restricts access to the hairpin-blocking site and substantially changes CTD interactions with the transmembrane domain.

Ball and Chain Gating

Steric block of the Cl^- permeation pathway by the N-terminal hairpin peptide (**Figure 5**) rekindles the hypothesis of a “ball-and-chain”-type gating mechanism for CLC-2, first proposed over 30 years ago (Grunder et al., 1992). In those studies, residue Q19 in the N-terminal hairpin, which hydrogen bonds to Q153 in the TM domain (**Figure 5C**), was identified as a residue critical to the “ball” blocking mechanism (Grunder et al., 1992). In follow-up studies, it was concluded that the “receptor” site on the TM domain is formed by residues in a stretch from 342-351 (Jordt and Jentsch, 1997) on helix J, which also forms part of the hairpin-docking site (**Figure 5C, Figure 5 – figure supplement 6A**). The hairpin-TM interface identified in our structure also exquisitely harmonizes with results from studying human mutations associated with primary aldosteronism. These gain-of-function mutations, which map squarely onto the peptide hairpin and surrounding TM region (**Figure 5 – figure supplement 6B**), cause increases in CLC-2 currents that depolarize the glomerulosal membrane potential thus leading to disease (Fernandes-Rosa et al., 2018; Scholl et al., 2018).

Our electrophysiology results also support a ball-and-chain gating mechanism. First, we demonstrate that the increase in current in hairpin-deleted channels reflects an increase in channel

activity rather than an increase in surface expression (**Figure 6D,E**), consistent with loss of a channel-closing mechanism. Second, we show that WT but not delta-N CLC-2 currents increase over time (**Figure 6F,G)**, consistent with relief of the hairpin block. Importantly, our use of the selective inhibitor AK-42 (Koster et al., 2020) provides confidence that the current increase is specific to CLC-2 and not a result of leak or a run-up of other Cl^- currents, which notoriously lurk in all mammalian cells and can confound interpretation of experimental results. In the context of our structure and the mutagenesis studies discussed above, our electrophysiological results fortify a ball-and-chain model for CLC-2 gating.

Ball-and-chain gating as a potential mechanism for CLC-2 current variability

How do we explain the ostensible discrepancy between our results, which support a ball-and-chain model, and the previously published results that were used to argue against a ball-and-chain type gating mechanism? We think the discrepancy is not as dire as it originally seemed. The previous discrepancy is as follows. In studies of an N-terminal CLC-2 deletion mutant in HEK 293 cells, Varela et al. observed currents that differed depending on whether whole-cell or nystatin-perforated patch clamp recording was used: with whole-cell recording, deletion-mutant currents displayed rectification similar to WT CLC-2 but with much faster kinetics; with perforated-patch recording, currents were voltage independent and non-rectifying (Varela et al., 2002). At the time, this difference was interpreted to mean that the open-channel phenotype (and therefore ball-and-chain gating) was artifactual, due to a diffusible intracellular factor binding to the N-terminal deletion channel, but not the WT channel, locking it open in the perforated-patch recording configuration (but diffusing away in whole-cell recording experiments). However, Varela et al. also aptly pointed out that mutagenesis experiments did support a role for the CLC-2 N-terminus in channel gating. Further, they noted that the different results between their two recording configurations could be due to differences of physiological relevance, such as osmotic forces and/or channel-cytoskeleton interactions (Grunder et al., 1992; Ahmed et al., 2000). Such factors could also explain the differences between our whole-cell recordings and those of Varela

et al. We note that our Delta-N currents observed with whole-cell recording (**Figure 6 – figure supplement 1**) are similar to currents displayed by the aldosteronism peptide-hairpin mutant G24D in perforated-patch clamp recordings (Goppner et al., 2019), supporting that our use of whole-cell recording is not introducing an artifact.

We hypothesize that sensitivity of ball-and-chain gating to physiological variables may underlie the tremendous variation in kinetics and voltage-dependence observed amongst recordings of natively expressed CLC-2 (Bosl et al., 2001; Jentsch and Pusch, 2018). Such variation could arise from differences in one or more of the factors known to modulate CLC-2 gating – osmotic forces, transmembrane voltage, ATP, phosphorylation, or interactions with the cytoskeleton or other cellular proteins (Nighot et al., 2017; Jentsch and Pusch, 2018; Okamoto et al., 2019) – and could be further modulated by the expression of N-terminal splice variants (Furukawa et al., 1995; Cid et al., 2000). We propose that mechanistic studies of the CLC-2 gating run-up we report here (**Figure 6F**) will be valuable to guide studies on the variability of CLC-2 currents in native systems and how it relates to ball-and-chain gating.

Revised framework for CLC-2 gating

The established framework for CLC channel gating (Jentsch and Pusch, 2018) is based on pioneering investigations on the *Torpedo* homolog CLC-0. These investigations identified two separate mechanisms responsible for channel gating (Miller, 1982). The first gating mechanism, referred to as “fast” or “protopore” gating, opens and closes each pore of the homodimer independently on a millisecond timescale. E_{gate} (**Figure 1**) plays a central role in this protopore gating (Dutzler et al., 2003), with voltage-dependence arising from interactions between E_{gate} and ions in the pore (Pusch et al., 1995). The second gating mechanism, referred to as “slow” or “common” gating, is orders of magnitude slower (seconds to tens-of-seconds timescale) than “fast” gating and operates in a highly cooperative manner to open and close both CLC-0 pores simultaneously. The simultaneous opening/closing of pores that are separated by >30 Angstrom, together with the exceptionally high temperature

dependence of slow gating (Pusch et al., 1997), suggests that large structural rearrangements are involved. Indeed, large movements of the CTDs were observed in a fluorescence resonance energy transfer study of CLC-0 slow gating (Bykova et al., 2006).

In CLC-2, electrophysiological studies of WT and mutant channels were used to illustrate that CLC-2 has two gating mechanisms (Zuniga et al., 2004; de Santiago et al., 2005; Yusef et al., 2006). However, it remains uncertain as to whether these two mechanisms are analogous to the fast protopore and slow common gating mechanisms observed in CLC-0. On one hand, studies demonstrating that interactions between E_{gate} and ions in the pore play a critical role in gating support that CLC-2 has a "fast" protopore gating mechanism (Niemeyer et al., 2003; Niemeyer et al., 2009; Sanchez-Rodriguez et al., 2010; Sanchez-Rodriguez et al., 2012; De Jesus-Perez et al., 2016). On the other hand, there are substantial differences between CLC-2's "slow" gating mode and CLC-0's common gating in terms of kinetics and temperature dependence. Moreover, unlike CLC-0 (Lin et al., 1999), CLC-2 slow and fast gating cannot be separately affected by mutation (Zuniga et al., 2004; de Santiago et al., 2005; Yusef et al., 2006; De Jesus-Perez et al., 2021). Finally, in contrast to CLC-0, it has not been demonstrated that the "slow" gate in CLC-2 corresponds to a common gating process operating on both pores simultaneously.

Our results strongly motivate a revised framework for understanding CLC-2 protopore gating. At least two events are needed to open each protopore - relief of block by the N-terminal hairpin (ball and chain gating) and E_{gate} movement (**Figure 8**). A key aspect of our revised framework is that ball and chain gating is coupled to CTD conformational change: close examination of the state with the CTD rotated (**Figure 4A**) reveals that the hairpin can't access its pore-blocking site in this state. Thus, CTD rotation facilitates hairpin release and channel opening. This structural model is consistent with electrophysiological studies showing that removal of the CTD speeds CLC-2 activation and deactivation kinetics (Garcia-Olivares et al., 2008). In contrast to CLC-0, where movements in the CTD have been linked to the highly cooperative conformational change involved in common gating (Estevez et al.,

2004; Bykova et al., 2006), our structures illustrate that in CLC-2 the CTDs can move independently of one another.

CLC-2 gating is more complex than depicted in our simple cartoon, and many questions remain. First, prior results suggest that CLC-2 “slow” gating involves conformational change beyond the E_{gate} and hairpin/CTD motions depicted in our model. Even when E_{gate} is neutralized, CLC-2 retains some voltage-dependent gating (Niemeyer et al., 2003), indicating a conformational change beyond E_{gate}. This additional voltage-dependent gating cannot be solely due to N-terminal ball and chain gating, since channels with N-terminal deletions retain biexponential voltage dependence as is seen in the wild type channels (Varela et al., 2002). Second, electrophysiological studies indicate that CLC-2 has at least two open states (de Santiago et al., 2005), but the physical basis for these different open states is unknown. These points strongly motivate studies to elucidate additional conformational changes in CLC-2. Whether such changes include a highly cooperative common gating mechanism will require functional studies to complement structures, ideally with visualization of gating in single-channel recordings. Augmenting complexity in understanding CLC-2 is our observation that channel rectification changes upon N-terminal deletion or ball and chain gating (**Figure 6F; Figure 6 – Figure supplement 2**): the molecular underpinnings of this change in rectification are wholly unknown. Addressing all these questions will be important for understanding CLC-2’s diverse functional characteristics and physiological roles in various tissues and cells (Bosl et al., 2001; Jentsch and Pusch, 2018).

Summary

The structures and electrophysiological data presented here reveal a ball-and-chain mechanism involved in CLC-2 gating and offer a framework for understanding CLC-2’s multiple gating mechanisms. In addition, the structures illuminate details for molecular recognition by the selective inhibitor AK-42, the first and currently only known small-molecule modulator that is both potent and selective for a CLC family member.

METHODS

Molecular biology and AK-42 synthesis

Full-length human CLC-2 (Uniprot ID: P51788) was fused to a C-terminal twin-strep tag with a linker of 5'- TCGAATTCTTTGGAAGTTTTGTTTCAAGGTCCAACTGCTGCCGCCGCT-3' containing a HRV 3C protease cleavage sequence (underlined). This human C-terminal twin-strep-tagged CLC-2 fusion construct was cloned into a modified pFastBac vector that contains a CMV promoter for protein expression in mammalian cells (Goehring et al., 2014; Park et al., 2017). For electrophysiology and cell surface protein biotinylation/isolation experiments, the twin-strep tag was replaced by a EGFP tag. A C-terminal GFP tag was previously shown to have no significant effect on CLC-2 channel kinetics or voltage dependence (Park, Arreola 1998). In the N-terminal deletion CLC-2 (delta-N), residues 14-27 (ALQYEQTLMYGRYT) were removed from full-length (WT) CLC-2.

AK-42 was synthesized and quantified as previously described (Koster et al., 2020)

Protein expression/ purification

The full-length CLC-2 construct was transformed to DH10Bac competent cells (Invitrogen) to isolate baculovirus bacmid. The bacmid was transfected to sf9 cells using Cellfectin-II (Invitrogen) to produce baculovirus. The baculovirus were then further amplified twice in sf9 cells. The protein was expressed with HEK293 GnTI$^-$ cells with the amplified baculovirus. HEK293 GnTI$^-$ cells were cultured in Freestyle 293 medium (Invitrogen) supplemented with 2% FBS on a shaker at 37 °C in the presence of 8% CO_2 to a density of 3×10^6 cells per ml, then infected with 5% v/v baculovirus. After culturing for another 8-16 hours, sodium butyrate was added at final concentration of 10 mM, then further expressed for 48 hours at 37 °C before harvest. Cells were pelleted and stored at -80 °C.

Frozen cell pellets were resuspended in resuspension buffer containing 50 mM Hepes, pH 7.5, 300 mM NaCl, 1 mM dithiothreitol (DTT), 1 mM ethylenediaminetetraacetic acid (EDTA), and 1 protease inhibitor cocktail tablet (MedChem Express), then briefly lysis cells with dounce homogenizer for 10-15 times. Cellular debris were collected by centrifugation at 18k rpm for 30 minutes at 4 °C, and

then resuspended with resuspension buffer supplemented with 1% lauryl maltose neopentyl glycol (LMNG) and 0.1% cholesteryl semisuccinate (CHS). After extraction for 2 hours, the lysate was centrifuged at 18k rpm for 40 minutes at 4 °C. The clarified lysate was incubated with 1 mL of strep-Tacin XT high-capacity resin (IBA) for 2 hours at 4 °C. Resin was washed with wash buffer containing 50 mM Hepes, pH 7.5, 300 mM NaCl, 1 mM DTT, 1 mM EDTA, 0.02% LMNG, and 0.002% CHS. Purified protein was released from resin with 50 µg HRV 3C protease and incubated at 4 °C for overnight. The retrieved protein was concentrated to 0.5 ml with Amicon Ultra (50 kDa cutoff, EMD Millipore) and followed by size-exclusion chromatography (SEC) using a superdex 200 Increased 10/300 chromatography column on an AKTA Purifier 10 FPLC system (GE Healthcare) with buffer containing 20 mM Hepes, 150 mM NaCl, 1 mM DTT, 0.5 mM EDTA, 0.002% LMNG, and 0.0002% CHS. Protein fractions were pooled, concentrated with Amicon Ultra (50 kDa cutoff, EMD Millipore) to ~5 mg/ml, and immediately used for cryoEM grid preparation.

For CLC-2 and AK-42 complex, AK-42 was first dissolved in DMSO to 45 mM, then further diluted with CLC-2 SEC buffer to 2 mM and mixed with purified and concentrated CLC-2 protein (2.9 mg/mL) to make final solution with CLC-2/AK-42 at a molar ratio of 1:10 (20 µM CLC-2 with 200 µM AK-42). The mixture was incubated at 4 °C for 3 hours and then used for cryoEM grid preparation.

CryoEM data collection and processing

Three microliters of the purified CLC-2 or CLC-2/AK-42 mixture was applied to glow-discharged copper Quantifoil R1.2/1.3 or R2/1 holey carbon grids (Quantifoil). Grids were incubated for 15 s, then blotted for 4s or 6s at 100% humidity, then plunge-frozen in liquid-nitrogen-cooled liquid ethane using a Vitrobot Mark IV (Thermo Fisher Scientific) at 4 °C.

The grids were imaged on a Titan Krios electron microscope (Thermo Fisher) operated at 300 kV with a Falcon 4 direct electron detector (Thermo Fisher Scientific) and SelectrisX energy filter (Thermo Fisher Scientific). Micrographs were recorded at a magnification of 130,000 × (pixel size of 0.946 Å per pixel) with EPU software (Thermo Fisher Scientific) Each image was composed of 40

individual frames with total cumulative dose of 50 e^- per $Å^2$. For CLC-2 dataset, images were collected with an exposure time of 7.5 seconds and a dose rate of 6.7 e^- per second per $Å^2$ (OR 6.0 e^- per second per pixel). For CLC-2/AK-42 dataset, images were collected with an exposure time of 5.6 seconds and a dose rate of 8.9 e^- per second per $Å^2$ (OR 8.0 e^- per second per pixel). Defocus values were set from -1.0 μm to -2.0 μm.

CryoEM data processing was performed mainly using CryoSPARC 3.2 (Structura Biotechnology Inc), except those mentioned specifically. For CLC-2 sample, a total of 14,198 movie stacks were subjected to motion correction. The contrast-transfer function (CTF) parameters were estimated using patch CTF. Initially, a total of 56,091 particles were auto-picked and subjected to reference-free 2D classification. A total of 7 class averages were selected as templated for automated particle picking. A total of 4,999,780 particles were auto-picked and extracted with a box size of 256 pixels. The extracted particles were then subjected to 2D classification to remove ice, contaminants, and aggregates. The following ab initio reconstruction and 3D refinement (for all structures presented in this paper) are all performed with C1 symmetry (no symmetry imposed). The cleared-up classes were used for ab initio reconstruction with two classes. These models were used as reference for a heterogenous refinement with no symmetry imposed. The best class from heterogenous refinement which contained 2,415,222 particles were subjected to non-uniform 3D refinements, followed by local 3D refinements, yielding final CLC2-TM map at 2.46 Å, as determined by the gold-standard measure of Fourier shell correlation (FSC) using a cut-off of 0.143. Local resolution was estimated with relion 3.1. To further improve density map of CTD, the selected 2,415,222 particles were divided into 10 subsets for 3D classification in relion 3.1. A reference map for 3D classification was generated by the 3D ab initio model in CryoSparc. Two of the classes, containing 56,580 and 39,272 particles respectively, showed distinct CTD features and were used for further non-uniform 3D refinement and local 3D refinements, separately. The resolution was determined by Fourier shell correlation (FSC) using a cut-off of 0.143 at 2.75 Å and 2.76 Å, respectively.

Processing for CLC2-AK42 sample was executed similarly as described above. In brief, a total of 14,300 movie stacks were motion corrected by CryoSPARC. After auto-picking, 5,214,695 particles were extracted and subjected to 2D classification. After 2D classification, 2,391,813 particles were used for non-uniform 3D and local refinement to generate the final 2.74 Å map. To further improve the CTD density map, 3D classification was performed. The best of the 10 classes, containing 66,251 particles, was used for further refinement. Local refinement with masking of the CTD allowed a resolution 4.03 Å to be reached.

Model building and refinement

The initial model of CLC-2 was generated by SWISS-MODEL using human CLC-1 (PDB:6qvc) as a homology model. It was fit to each map and manually rebuilt using Coot (Emsley and Cowtan, 2004) (v0.91). The models were further refined with ISOLDE (Croll, 2018) in ChimeraX (Pettersen et al., 2004) (v.1.6) and Phenix (Liebschner et al., 2019) (v1.20) real space refinement. The two potential conformations for the AK-42 ligand were tested using the Quantum Mechanical Restraints (QMR) method (Liebschner et al., 2023). Q-scores were performed with the MapQ Chimera plugin v1.9.12.

Cell surface protein biotinylation and isolation

CHO K1 cells (ATCC CCL–61) were cultured at 37°C [95/5% O_2/CO_2 ratio] in F12K media (ATCC, Catalog no. 30-2004) supplemented with 10% fetal bovine serum (Gibco) and 1% penicillin/streptomycin (Gibco). Cells were seeded at 5×10^6 in 15-cm dishes. After 48 hours, the confluency reached around 60%, and cells were transfected with 6 µg of CLC-2 plasmid, either WT or Delta-N, using Lipofectamine LTX, opti-MEM, and PLUS reagent (Invitrogen). For the control sample, CHO cells were seeded at the same time as the transfected groups and kept culturing in parallel. 48-72 hours after transient transfection, two 15-cm dishes cells for each sample (WT, delta-N, or control) were combined to create one sample for use in the biotinylation of surface proteins assay, which was performed using a Pierce cell surface protein biotinylation and isolation kit (Thermo Scientific, A44390).

Briefly, cells were washed twice in PBS (0.1 M sodium phosphate, 0.15 M NaCl, pH 7.2) and then incubated with PBS containing 0.25 mg/ml of sulfosuccinimidyl 2-(biotin-amido)-ethyl-1,3-dithiopropionate (EZ-link Sulfo-NHS-SS-biotin, Pierce) at room temperature for 10 minutes. Cells were incubated in ice-cold TBS (25 mM Tris, 0.15 M NaCl, pH 7.2) twice to quench the labeling. Cells were then scraped and lysed in lysis buffer from the Kit. Samples were incubated at 4°C for 30 minutes and then centrifugated at 15,000 × g for 5 minutes. Following centrifugation, the extracted membrane samples from the supernatant were incubated with 50 µl NeutrAvidin™ Agarose (Pierce) at 4°C for 2 hours, then washed with wash buffer from the kit four times. Finally, the isolated proteins were eluted with 60 µl elution buffer (from the kit) containing 100 mM DTT. 40 µl of each sample was used for Western blotting detection with 1:2,500 anti-GFP antibody (Invitrogen A11122) and 1:10,000 anti-rabbit secondary antibody (Licor 926-68073). The relative expression level was calculated by quantifying the intensities of the 100-kD bands on the Western blot, using a Li-Cor Odyssey 9120 Infrared Imaging System. The samples from three independent experiments (independent transfections on different days) were run on a single Western blot, shown in Figure 6D and in Figure 6 – source data 2.

Cell Culture and patch-clamp recording

CHO K1 cells (ATCC CCL–61) were cultured at 37°C [95/5% O2/CO2 ratio] in F12K media (ATCC, Catalog no. 30-2004) supplemented with 10% fetal bovine serum (Gibco) and 1% penicillin/streptomycin (Gibco). At 60% confluency, cells were transfected with 120 ng CLC-2, either WT or delta-N, using Lipofectamine LTX, opti-MEM, and PLUS reagent (Invitrogen). 105 ng of a soluble GFP construct was co-transfected with the CLC-2 construct to improve visualization of transfected cells.

Whole-cell patch-clamp experiments were performed using an Axopatch 200B amplifier attached to a Digidata 1440A. Data were acquired at 10 kHz with filtering at 5 kHz. Traces shown in figures were filtered offline in Clampfit at 1 kHz (8-pole Bessel). Borosilicate glass micropipettes (Sutter Instruments BF150-86-10) were pulled and fire-polished to a tip diameter with a resistance of 1.8 to 3.4 MΩ. For

whole-cell patch-clamp recordings, the external solution was composed of 148 mM CsCl, 2 mM $CaCl_2$ (from a 1 M aqueous stock), 100 mM D-mannitol, and 10 mM HEPES, adjusted to pH 7.4 with 2 M CsOH. The internal solution was composed of 146 mM CsCl, 5 mM EGTA, 5 mM NaF, 60 mM D-mannitol, and 10 mM HEPES, adjusted to pH 7.4 with 2 M CsOH. Bath perfusion of external solution (2 mL/min) was initiated after whole cell and series resistance compensation (70% or more) was established. For leak subtraction, 300 nM AK-42 was perfused at 2 mL/min. AK-42 was diluted from a 1 mM stock solution in DMSO (0.03% final [DMSO]).

MD simulations

System setup for MD simulations. The apo dimer structure was used for simulations. For all simulations, hydrogen atoms were added, and protein chain termini were capped with neutral acetyl and methylamide groups. Titratable residues were kept in their dominant protonation state at pH 7. Histidine residues were modeled as neutral, with a hydrogen atom bound to epsilon nitrogen. The Dowser program was used to hydrate pockets within and around each structure (Morozenko and Stuchebrukhov, 2016). Then the receptor was inserted into a pre-equilibrated palmitoyl-oleoyl-phosphatidylcholine (POPC) bilayer using Dabble (Betz, 2017). Sodium and chloride ions were added to neutralize each system at a concentration of 150 mM. Approximate system dimensions were 131 Å x 95 Å x 125 Å.

Simulation protocols. All simulations were run on a single Graphical Processing Unit (GPU) using the Amber18 Compute Unified Device Architecture (CUDA) version of particle-mesh Ewald molecular dynamics (PMEMD) (Salomon-Ferrer et al., 2013). We used the CHARMM36m parameter set for protein molecules, lipids, and ions, and the CHARMM TIP3P water model for waters (Huang and MacKerell, 2013). Heating (to 310 K over 137.5 ps) and equilibration (28 ns with restraints on protein and ligand) steps were performed before production simulations as described previously (Suomivuori et al., 2020). Trajectory snapshots were saved every 200 ps. All simulations were at least 2 microseconds in length.

Simulation analysis protocols. The AmberTools18 CPPTRAJ package (Roe and Cheatham, 2013) was used to reimage trajectories, while Visual Molecular Dynamics (VMD) (Humphrey et al., 1996), PyMol (Schrodinger), and Matplotlib Python package were used for visualization and analysis. For analysis, the N-terminus peptide backbone was defined as segment name P5, excluding residues 14 15 27 28. For the CTD analysis, we used segment names P9 P3 P4 P8 excluding residue 419 to 578. For bar plots, individual dots show the average value in each independent simulation. Bar values show the average value across the independent simulations. The error bars for simulation results show the 68% confidence intervals of the mean (appropriate for non-parametric distributions) calculated using bootstrapping with the Seaborn Python library.

ACKNOWLEDGMENTS

We thank Huawei Zhang for sharing pdb coordinates and cryo-EM density for CLC-2/AK-42 in advance of release. We thank Anna Koster, Bill Kobertz, Dan Collins, Jürgen Kreiter, Martin Prieto, Shwetha Srinivasan, and Chris Miller for comments on the manuscript. We also thank Nigel Moriarty (Phenix) for performing Quantum Mechanical Restraints (QMR) analysis of the AK-42 ligand.

FUNDING

This research was funded by NIH R21NS125767 (M.M. and W.C.) and NIH R01NS113611 (M.M., J.D.B., and R.O.D.). CryoEM was performed at the Stanford-SLAC Cryo-EM Center (S^2C^2), which is supported by the National Institutes of Health Common Fund Transformative High-Resolution Cryo-Electron Microscopy program (U24 GM129541). M.X. was supported by a Wu Tsai Neurosciences Institute Interdisciplinary Scholar Award. S.D.M. is supported by a Stanford Bio-X Bowes fellowship.

AUTHOR CONTRIBUTIONS

MX: Conceived and carried out experiments, performed molecular biology to generate constructs, purified protein, collected and analyzed cryoEM data, built and refined experimental model, performed

surface biotinylation experiments, generated figures, drafted, reviewed, and edited manuscript. **TN:** Conceived, carried out, and analyzed electrophysiology experiments, reviewed manuscript. **ASP:** Conceived, carried out, and analyzed MD simulations, reviewed and edited manuscript. **YL:** cryoEM data collection and analysis. **SDM:** Synthesized AK-42, performed transfections and cell culture for electrophysiology experiments, analyzed electrophysiology data, reviewed and edited manuscript. **GP:** Model refinement, analysis, validation and deposition, writing related to ligand modeling and validation. **JDB:** Supervision, manuscript review and editing, funding. **ROD:** Supervision, manuscript review and editing, funding. **WC:** Supervision, manuscript review and editing, funding. **MM:** Conceived experiments, supervised, drafted, reviewed, and edited manuscript, funding.

DATA AVAILABILITY

Cryo-EM Density maps and structure coordinates have been deposited in the Electron Microscopy Data Bank (EMDB) and the Protein Data Bank (PDB), with accession codes EMD-41127 and PDB 8TA3 for the CLC2-TM, EMD-41128 and PDB 8TA4 for the CLC2-CTDsym, EMD-41129 and PDB 8TA5 for CLC2-CTDasym, EMD-41126 and PDB 8TA2 for CLC2-TM-AK42, and EMD-41130 and PDB 8TA6 for CLC2-AK42-CTD-only.

FIGURE LEGENDS

Figure 1. Gating conformations in CLC transporters and channels. (**A**) Cartoon depictions of the CLC anion-permeation pathway. The “gating glutamate” (E_{gate}) can occupy anion binding sites within the permeation pathway (“down” and “middle” conformations, occupying the central (S_{cen}) and external (S_{ext}) anion-binding sites respectively) or away from these sites (“up” and “out” conformations). Coupling of E_{gate} movement to Cl^-/H^+ binding/unbinding and global conformational change generates 2:1 Cl^-/H^+ exchange. (**B**) E_{gate} is required for voltage-dependent gating in CLC channels but cryoEM density for this residue has been observed only in CLC-1 (PDB ID: 6coy), in the “out” position. In contrast to CLC-1, which is predominantly open at zero mV, CLC-2 is predominantly

closed. The open probability (P_o) versus voltage (V) traces were drawn based on published data reported for CLC-1 (Lisal and Maduke, 2008) and CLC-2 (Stolting et al., 2013).

Figure 2. CryoEM structure of the human CLC-2 channel. Overall structure of the transmembrane domain ("CLC2-TM") at 2.46 Å. The identical subunits of the homodimer are shown in purple and gray, Cl^- ions are shown as green balls. (**A**) cryoEM density map with model overlay (contour level: 0.71, 5.5 σ) and (**B**) model only with dashed arrows indicating the locations of pathways detected by Caver: orange, primary Cl^- pathway common to all CLCs; yellow, secondary Cl^- pathway detected in CLC-2 and CLC-1. Details of the pathways are presented in Figure 3. The secondary pathway, whose function is not yet known, was so named when first observed in the CLC-1 structure (Park and MacKinnon, 2018). (**C**) Zoomed-in views showing cryoEM density overlay of bound Cl^- and key residues – E_{gate} (E205) and inner-gate residues Ser_C (S162) and Tyr_C (Y553). S_{cen} is indicated with a green dashed circle. Contour level: 1.1, 7.2 σ (middle panel); 0.97, 6.3 σ (right panel).

Figure 2 - figure supplement 1. Micrograph, 2D classes, and structure validation of CLC2-TM. (**A**) Representative motion-corrected cryoEM micrograph. (**B**) 2D class averages. (**C**) Gold standard FSC plots calculated in cryoSPARC. (**D**) Local resolution of the cryoEM map of the CLC2-TM. (**E**) Model validation using Q-scores (Pintilie et al., 2020) of subunit A (left) and subunit B (right). The black line represents the expected Q-score at respective resolution based on the correlation between Q-scores and map resolution.

Figure 2 - figure supplement 2. CryoEM workflow of the CLC2 single-particle cryoEM data processing. A total of 14,198 movie stacks were collected on a 300 kV Titan Krios cryo-electron microscope. cryoSPRAC was used for 2D classification, and the CLC2-TM density map was obtained after 2D classification. Relion was used for 3D classification and yielded two conformations differing

in the CTD: CLC2-CTDsym and CLC2-CTDasym. Resolutions shown refer to the whole protein molecule.

Figure 2 - figure supplement 3. Helix map of CLC2-TM. cryoEM densities and model of CLC-2 transmembrane helices (contour level: 0.73, 2.7 σ)

Figure 2 - figure supplement 4. E_{gate} position and Cl^- binding sites (S_{ext} and S_{cen}). (**A**) Comparison between CLC-2 (purple), CLC-1 (light blue), and cmCLC (salmon pink). E_{gate} (E205 in CLC-2, E232 in CLC-1, and E210 in cmCLC), Ser_C (S162 in CLC2, S189 in CLC-1, and S165 in cmCLC) and Tyr_C (Y553 in CLC-2, Y578 in CLC-1, and Y515 in cmCLC) are shown as sticks. In CLC-2 and cmCLC, S_{ext} is occupied by Cl^-, and S_{cen} is occupied by E_{gate}. E_{gate} is in the "down" position. In CLC-1, S_{ext} is occupied by Cl^-, and S_{cen} lacks anion density. E_{gate} is in the "out" position, away from the Cl^--permeation pathway. (**B**) Overlay view (stereo) of panel **A**. (**C**) Overlay with the CLC-2 E_{gate} conformations modeled in PDB ID: 7XJA (Ma et al., 2023).

Figure 3 Pore profile detected in CLC-2. (**A**). Left: The primary (orange) and secondary (yellow) pore detected in CLC-2 using Caver. Middle: The detected pore radii are displayed in dots as a color map. Right: Zoomed-in view of the restricted (narrowest) site of the pore profile, using the same coloring as in the middle panel. E_{gate}, Ser_C and Tyr_C are shown as sticks. (**B**). Pore profile for CLC-1 (PDB ID:6coy), with display as in panel **A**.

Figure 3 - figure supplement 1. Cl^- pathway in CLC-2 and CLC-1. (**A**) CLC-2 Cl^- pathway as shown in Figure 3 but omitting sections with pore radius less than 1Å. E_{gate}, occupying the S_{cen} site, blocks the canonical Cl^- pathway. (**B**) same as panel A, for CLC-1 (PDB ID:6coy).

Figure 3 - figure supplement 2. Comparison of primary and secondary Cl^- pathways with transporter Cl^- and H^+ pathways. (**A**) The top two panels are repeated from Figure 3A, indicating the primary (orange) and secondary (yellow) caver-detected pores in CLC-1 and CLC-2. The lower panel shows CLC-ec1 (PDB ID: 1OTS), a representative for the CLC transporters, where caver detects only the primary pore (orange dots as for CLC-1 and CLC-2). (**B**) Detected pore radii show a longer constriction in the CLC-ec1 transporter compared to the CLC-1 and CLC-2 channels. (**C**) Zoomed-in view of the secondary-pore region for CLC-2 (top), CLC-1 (middle) and CLC-ec1 (bottom). The CLC-ec1 panel shows water wires (space-filled) detected in simulations of the QQQ mutant structure (PDB ID: 6V2J) (Chavan et al., 2020).

Figure 4. Different conformations of the CTD. (**A**). Overall structure of the two CLC-2 conformations. Left: CLC2-CTDsym at 2.75 Å. Right: CLC2-CTDasym at 2.76 Å. The subunits of the homodimer are shown in orange (CLC2-CTDsym) or yellow (CLC2-CTDasym) and gray (for both). The subunits adopting different CTD conformations are shown in orange and yellow, while the subunits sharing the same CTD conformation are shown in gray. The dashed line demarcates the transmembrane (TM) and cytoplasmic (CTD) domains. A hairpin structure detected at the intracellular pore is shown in blue. (**B**) Overlay of two conformations. (**C**) Hinge movement of the CTD between two conformations. The middle panel shows an overlay of CLC2-CTDsym (orange and gray) and CLC1-CTDasym (yellow and gray), with the CTDs highlighted in boxes. For the subunits that adopt different conformations (orange and yellow), the double-headed arrow indicates the change between the two conformations. The RMSD between the subunits shown in orange/yellow is 6.9 Å, while the RMSD for the subunits shown in gray is only 1.3 Å. Alignments of only the CTDs are shown at left and right; in these alignments, the low RSMD values (0.9 Å and 1.0 Å, respectively) indicate that the CTDs undergo a hinge movement.

Figure 4 - figure supplement 1. Structure validation of CLC2-CTDsym and CLC2-CTDasym. (**A**) Gold standard FSC plots calculated in cryoSPARC for CLC2-CTDsym. (**B**) Local resolution of the cryo-EM map of the CLC2-CTDsym. (**C**) Model validation using Q-scores of subunit A (left) and subunit B (right) of CLC2-CTDsym. The black line represents the expected Q-score at respective resolution based on the correlation between Q-scores and map resolution. (**D-F**) the same as (**A-C**) for CLC2-CTDasym**.**

Figure 4 – figure supplement 2. CryoEM density maps for the two CTD-containing CLC-2 conformations, overlaid with structural models. (**A**) CLC2-CTDsym (contour level: 0.68, 4.9 σ). (**B**) CLC2-CTDasym (contour level: 0.75, 6.8 σ). Side view (left) and top view (right) are shown. (**C**) CTD of CLC2-CTDsym shows two CBS domains on each subunit (orange and light orange for subunit A; gray and light gray for subunit B).

Figure 4 - figure supplement 3. MD analysis indicates conformational flexibility of the CTD. (**A**) The CTD is highly mobile relative to the transmembrane domain, and often tilts upward or downward relative to its initial location. In the inset images, two representative frames from simulation are shown (orange) overlaid on the starting structure (black outline). (**B**) The RMSD (root mean square deviation) and RMSF (root mean square fluctuation) of the cytoplasmic domain backbone were calculated after aligning frames on the transmembrane domains. Bars show the mean of five independent simulations, each 2.0 μs in length. Error bars are 68% confidence intervals of the mean.

Figure 4 - figure supplement 4. Comparison of CTD orientation with respect to the TM domain. (**A**) The CLC-1 structure is shown in light blue. The angle of orientation for the CTDs was calculated using the far end residue of helix T (the second helix of first CBS domain) as the endpoint of rays and the center of the TM-CTD connecting plane as the vertex of the angle. On the right the CTD is shown in surface representation following rotation as indicated. Panels (**B**) – (**F**) show the CLC homolog

indicated, with angles calculated as for CLC-1, and the rotated view of the CTD shown to compare the positioning of the CTDs relative to the membrane domains. The dashed lines indicate the long axes of the CTDs. In each panel, CLC-1 is shown in light blue as a reference for comparison. (**G**) and (**H**) overlays compare the CTD orientations in the CLC-2 structures to that in CLC-7. PDB IDs are shown in the parentheses. PDB IDs for CLC2-CTDsym and CLC2-CTD asym are 8TA4 and 8TA5.

Figure 4 – figure supplement 5. ATP binding site comparison between CLC-2 and CLC-5. Top: Structural overlay of CLC2-CTDsym (in orange) and CLC5-CTD (in dark purple) with ATP (pink carbon atoms; CPK coloring on non-carbon atoms. PDB ID: 2J9L). Bottom: Zoomed in stereo view of ATP binding site in CLC5-CTD (dark purple) overlaid with the same region in CLC2-CTDsym (orange). Residue numbers are labeled in dark purple for CLC-5 and orange for CLC-2.

Figure 5. The blocking hairpin structure corresponds to an N-terminal sequence of CLC-2. (**A**). *Left:* The hairpin structure seen in the cryoEM density (blue mesh) fits N-terminal residues 14-28 (blue). *Right:* The subunit in CLC2-CTDasym structure that contains a CTD with rotated orientation lacks density for the hairpin structure. In this structure, the residues linking TM helices J and K are not resolved. The dark blue circles indicate this unresolved region (right panel) and the corresponding resolved J-K helix that occurs in the other subunits. (Contour level: 0.76, 5.5 σ.) (**B**) Model validation using Q-scores for the N-terminal hairpin: orange and light orange for subunits A & B of CLC2-CTDsymsubunit; yellow for subunit A (the hairpin-containing subunit) of CLC2-CTDasym. The black line represents the expected Q-score at 2.75 Å based on the correlation between Q-scores and map resolution. (**C**) Residues on the transmembrane domain interact with the N-terminal hairpin. The J-K helical linker and TM Helices C, D, R, and J are labeled with arrows. Inset: Zoomed-in view of two hydrogen bonds formed between the hairpin structure and the TM domain: Q19-Q153 and T20-R363. Mutation of these two residues (Q25 and T26 in rat CLC-2) generated an open-channel phenotype for CLC-2 expressed in *Xenopus* oocytes (Grunder et al., 1992).

Figure 5 – figure supplement 1. Comparison of peptide candidates fitting into the hairpin density. (**A**) Best-fitting peptide candidate from the N-terminus (left shown in blue) and from the C-terminus (right shown in purple) fitted into cryoEM hairpin density (blue mesh). (**B**) Q-score plot of the two peptide candidates (residues 1-15 of the respective sequences). The Q-scores for the C-terminal peptide are generally lower than the Q-score expected for the corresponding resolution (0.65).

Figure 5 supplement 2. N-terminal hairpin sequence is conserved in CLC-2, but not other CLCs. (**A**) Alignment of the N-terminal hairpin sequence (blue boxed) amongst different species. (**B**) Alignment of N-terminal hairpin sequence (blue boxed) amongst other human CLCs.

Figure 5 – figure supplement 3. Electrostatic map of the N-terminal hairpin blocking site. Left: view from the cytoplasm showing the electrostatic surface potential of the TM region (blue, positive; red, negative), with the hairpin shown in cartoon. Right: side view showing the electrostatic surface potential of the hairpin (blue, positive; red, negative) and the TM blocking site shown in transparent cartoon model.

Figure 5 – figure supplement 4. MD simulations confirm the N-terminal hairpin structure is stable (**A**) In simulations, the N-terminus (blue) remains stably bound to the intracellular side of the transmembrane domain (orange). In the inset image, frames of the N-terminus taken every 200 ns from a representative simulation are overlaid. (**B**) The root-mean-square deviation (RMSD) and root-mean-square fluctuation (RMSF) of the N-terminus backbone were calculated after aligning frames on the transmembrane domains. Bars show the mean of five independent simulations, each 2.0 μs in length. Error bars are 68% CI (confidence interval of the mean).

Figure 5 - figure supplement 5. The N-terminal hairpin blocks the primary Cl^- pore in CLC-2. (**A**) *Left:* Side view of CLC2-TM showing the caver-detected pore (primary in orange and secondary in yellow). *Right:* View of the primary pore from the intracellular side. (**B**) The N-terminal hairpin (blue) overlaid with CLC2-TM as shown in panel **A**.

Figure 5 – figure supplement 6. Mapping mutant data onto the cryoEM structure. (A) Left: same as Figure 5C, showing hairpin interactions. Right: Rotated view highlighting ball "receptor" residues identified by Jordt and Jentsch, 1997. (**B**) Residues mutated in human Aldosteronism (Fernandes-Rosa et al., 2018; Scholl et al., 2018) and Leukoencephalopathy (Gaitan-Penas et al., 2017) are shown on CLC2-CTDsym in magenta and green, respectively).

Figure 6 Patch-clamp experiments support CLC-2 channel block by the N-terminal hairpin structure. (**A**) Representative currents from WT and delta-N CLC-2, recorded using the whole-cell patch clamp configuration in response to the voltage protocol shown. (**B**) WT CLC-2 recording from panel A, shown on an expanded scale. (**C**) Summary of current levels measured for WT and delta-N CLC-2 at the end of the 1-s voltage pulse to -100 mV. Data are from six independent transfection samples, in each case with WT and delta-N recorded on the same day following transfection. WT: -600 ± 102 pA (SEM, n=8);Delta-N: -3300 ± 630 pA (SEM, n=8). (**D**) Western blot detection of biotinylated surface-expressed CLC-2 from three independent experiments. (**E**) Summary data for electrophysiology and surface-biotinylation experiments. Points representing individual experiments for Delta-N surface biotinylation (each normalized to WT) are shown. Individual data points for the electrophysiology experiments are shown in panel C. (**F**) Representative examples of experiments to evaluate current run-up in WT and Delta-N CLC-2. *Left panels:* Time course data. Following an initial voltage-family measurement (I-V protocol as in panel A, taken at point "1"), currents were monitored by 1-s pulses to -100 mV every 5 s for five minutes, after which a second voltage-family measurement was made (point 2), followed by application of AK-42 to facilitate leak subtraction, and

a final voltage-family measurement at point 3. I-V traces are shown at right. (**G**) Summary data for "run-up" experiments. *Left panel:* Normalized time-dependent currents for WT and delta-N. Currents were first leak-subtracted (using the steady-state current after AK-42 application) and then normalized to the amplitude of the current measured in the first step of the 5-minute sequence. *Right panels:* Leak-subtracted current levels at -100 mV from "initial" and "final" IV traces measured at points "1" and "2' in the time course (panel F). Average initial and final currents (pA ± SEM, n=8) are WT: -600 ± 102 and -1400 ± 260; Delta-N: -3300 ± 630 and -2900 ± 420).

Figure 6 – figure supplement 1. Data traces from the CLC-2 run-up experiments summarized in Figure 6G. For Delta-N, separate scale bars indicate the currents for the top six and bottom 10 traces. AK-42 leak currents, not subtracted in these raw data traces, are summarized in Figure 6 – source data 1.

Figure 6 – figure supplement 2. CLC-2 current rectification. (**A**) Example traces from two experiments on WT CLC-2. Current values at end of the -100-mV test pulses and in the steady-state portion of the +80-mV tail pulse (following the +20-mV test pulse) are indicated. Robust AK-42 inhibition of the current at +80 mV indicates that CLC-2 is passing current at positive voltages. (**B**) Rectification ratios. Rectification was quantified by taking the ratio (absolute value) of the leak-subtracted currents at -100 mV and +80 mV. For WT initial currents, the low currents at +80 mV make this quantification challenging: for 5 out of 8 experiments on WT CLC-2, the AK-42 current at +80 mV was greater than the initial WT current at +80 mV, likely due to an increase in leak over the course of the experiment (~15 minutes of voltage pulsing). Therefore, the rectification calculated for the WT initial currents (99 ± 34, SEM n=3) has substantial uncertainty. That said, such high rectification is consistent with reports of CLC-2 rectification throughout the literature (Park et al., 1998; Arreola et al., 2002; Jentsch and Pusch, 2018). On the other hand, Delta-N currents display only mild rectification, which is straightforward to quantify given the high signal:noise (high AK-42-

sensitive current relative to background), and which does not change in response to voltage pulsing. For “WT-final”, the rectification ratio similarly can be accurately quantified. Thus, while the high uncertainty and variance in estimating WT initial rectification precludes quantitative statistical comparisons, these data strongly suggest that WT CLC-2 current rectification decreases in parallel to current run-up. (**C**) WT initial rectification ratio from panel B replotted to show the individual data points from the 3 experiments in which AK-42 current at +80 mV was less than the initial WT current at +80 mV. Data for all experiments are summarized in Figure 6 – source data 1.

Figure 7 Bound AK-42 blocks the Cl^- pathway in CLC-2. (**A**) TM-domain structure of the CLC-2 structure in complex with AK-42 (CLC2-TM-AK42) at 2.74 Å. The identical subunits of the homodimer are shown in hot pink and gray; Cl^- ions are shown as green balls. Bound AK-42 is highlighted with a yellow circle on the pink subunit. The cyan arrow indicates the Cl^- pathway. (**B**) Zoomed-in view of the AK-42 binding site (contour level: 0.91, 6.0 σ). (**C**) A sliced view of CLC-2 showing AK-42 (yellow carbon atoms; CPK coloring on non-carbon atoms) and E_{gate} (CPK sticks). Both AK-42 and E_{gate} obstruct the Cl^- pathway, displayed as a color map.

Figure 7 - figure supplement 1. CryoEM workflow of the CLC2-TM-AK42 single-particle cryo-EM data processing. A total of 14,300 movie stacks were collected on a 300 kV Titan Krios cryo-electron microscope. cryoSPRAC was used for 2D classification and CLC2-TM-AK42 density map was obtained after 2D classification. Relion was used for 3D classification.

Figure 7 - figure supplement 2. Micrograph and 2D classes and structure validation of CLC2-AK42. (A) Representative motion-corrected cryo-EM micrograph. (B) 2D class averages. (C) Gold standard FSC plots calculated in cryoSPARC for CLC2-TM-AK42 (left) and CLC2-AK42-CTD-only (right). (D) Local resolution of the cryo-EM map for CLC2-TM-AK42 (left) and CLC2-AK42-CTD-only (right)

Figure 7 - figure supplement 3. Model validation using Q-scores. (**A**) Q-scores of CLC2-TM-AK42 for subunit A (left) and subunit B (right). (**B**) Q-scores of CLC2-AK42-CTD-only for subunit A (left) and subunit B (right). The black line represents the expected Q-score at respective resolution based on the correlation between Q-scores and map resolution.

Figure 7 - figure supplement 4. cryoEM map and structure of CLC2-AK42. (**A**) cryoEM model of CLC2-TM-AK42 with docked CTD. The transmembrane region is shown in hot pink and gray. The CTD is shown in green and gray. AK-42 is shown in yellow and highlighted by yellow circles. Chloride ions are shown in green. (**B**) cryoEM model overlay with density map of CLC2-AK42. Contour level: 0.83, 6.8 σ (TM region); 0.35, 14 σ (CTD).

Figure 7 - figure supplement 5. Helix map of CLC2-TM-AK42. cryo-EM densities and model of CLC2-AK42 transmembrane helices (contour level: 0.52, 3.4 σ)

Figure 7 – figure supplement 6. Density overlay at key Cl^--pathway residues. Zoomed-in view highlighting residues S162, E205, Y553, and the bound chloride ion, with cryoEM density overlay (contour level: 1.4, 9.0 σ).

Figure 7 - figure supplement 7. AK-42 binding site comparison between CLC2-TM and CLC2-TM-AK42. Top: Stereo view of structural overlay at the AK-42 binding site. Hydrogen bonds between AK-42 and residues K204,S392,K394 are indicated by blue dashed lines. Bottom: A view highlighting the movement of residue M460 to make space for AK-42.

Figure 7 - figure supplement 8. Structural comparison of CLC2-TM and CLC2-TM-AK42. Difference distance matrices comparing Cα residues on TM helices between CLC2-TM and CLC2-TM-AK42 in subunits A (**A**) or B (**B**). Residues in loops connecting helices, where there is low

confidence in the model building (Q score lower than the expected Q score of 0.65), were omitted from the matrices.

Figure 7 - figure supplement 9 AK-42 binding site comparison between CLC-2 and CLC-1. (**A**) Top: Stereo view of the AK-42 binding site in CLC2-TM-AK42 (hot pink) overlaid with the same region in CLC-1 (blue, PDB:6coy). Residue numbers correspond to those of CLC-2. The five residues that differ between CLC-2 and CLC-1 are: I112 (S139), S392 (M419), Q393 (P420), K394 (R421), and L397 (I424). Bottom: Rotated (stereo) view of AK-42 binding site to compare residues S392, Q393 and K394 in CLC-2 versus M419, P420 and R421 in CLC-1. These three were calculated to contribute most significantly to the AK-42 binding energy (Ma, 2023). (**B**) Residues in CLC-1 predicted to clash with AK-42. AK-42 is shown in yellow sticks and white surface. F252 and M460 in CLC-2 correspond to F279 and M485 in CLC-1.

FIGURE 8: CLC-2's gating is illustrated based on our new structural data. Opening of each protopore requires at least two events – unblock by the N-terminal hairpin ("N-ter") and rotation of E_{gate} away from the permeation pathway. The dashed green arrow represents the Cl^- conduction pathway. Hairpin unblock (ball and chain gating) is coupled to conformational change of the CTD: rotation of the CTD towards the membrane precludes hairpin binding, thus facilitating channel opening. Opening of the channel pore following these two events is depicted for one subunit of the homodimer (filled green arrow).

Video 1. CLC-2 pore detected using Caver.

Video 2. CLC-1 pore detected using Caver.

Video 3. CLC-ec1 Caver detected pathway.

Video 4. Rigid body movement from CLC2-CTDsym to CLC2-CTDasym.

Video 5. Hairpin surface potential.

Video 6. AK-42 density.

REFERENCES

Accardi, A., and C. Miller. 2004. Secondary active transport mediated by a prokaryotic homologue of ClC Cl- channels. *Nature*. 427:803-807.

Ahmed, N., M. Ramjeesingh, S. Wong, A. Varga, E. Garami, and C.E. Bear. 2000. Chloride channel activity of ClC-2 is modified by the actin cytoskeleton. *Biochem. J.* 352 Pt 3:789-794.

Alioth, S., S. Meyer, R. Dutzler, and K. Pervushin. 2007. The cytoplasmic domain of the chloride channel ClC-0: structural and dynamic characterization of flexible regions. *J. Mol. Biol.* 369:1163-1169.

Altamura, C., J.F. Desaphy, D. Conte, A. De Luca, and P. Imbrici. 2020. Skeletal muscle ClC-1 chloride channels in health and diseases. *Pflugers Arch.* 472:961-975.

Anashkin, V.A., A.A. Baykov, and R. Lahti. 2017. Enzymes Regulated via Cystathionine beta-Synthase Domains. *Biochemistry (Mosc.)*. 82:1079-1087.

Arreola, J., T. Begenisich, and J.E. Melvin. 2002. Conformation-dependent regulation of inward rectifier chloride channel gating by extracellular protons. *J. Physiol.* 541:103-112.

Betz, R.M. 2017. v2.6.3. *Zenodo*.

Bosl, M.R., V. Stein, C. Hubner, A.A. Zdebik, S.E. Jordt, A.K. Mukhopadhyay, M.S. Davidoff, A.F. Holstein, and T.J. Jentsch. 2001. Male germ cells and photoreceptors, both dependent on close cell-cell interactions, degenerate upon ClC-2 Cl(-) channel disruption. *EMBO J.* 20:1289-1299.

Brenes, O., M. Pusch, and F. Morales. 2023. ClC-1 Chloride Channel: Inputs on the Structure-Function Relationship of Myotonia Congenita-Causing Mutations. *Biomedicines*. 11.

Bykova, E.A., X.D. Zhang, T.Y. Chen, and J. Zheng. 2006. Large movement in the C terminus of CLC-0 chloride channel during slow gating. *Nat. Struct. Mol. Biol.* 13:1115-1119.

Cederholm, J.M., G.Y. Rychkov, C.J. Bagley, and A.H. Bretag. 2010. Inter-subunit communication and fast gate integrity are important for common gating in hClC-1. *Int. J. Biochem. Cell Biol.* 42:1182-1188.

Chavan, T.S., R.C. Cheng, T. Jiang, Mathews, II, R.A. Stein, A. Koehl, H.S. McHaourab, E. Tajkhorshid, and M. Maduke. 2020. A CLC-ec1 mutant reveals global conformational change and suggests a unifying mechanism for the CLC Cl(-)/H(+) transport cycle. *Elife*. 9.

Chovancova, E., A. Pavelka, P. Benes, O. Strnad, J. Brezovsky, B. Kozlikova, A. Gora, V. Sustr, M. Klvana, P. Medek, L. Biedermannova, J. Sochor, and J. Damborsky. 2012. CAVER 3.0: a tool for the analysis of transport pathways in dynamic protein structures. *PLoS Comput. Biol.* 8:e1002708.

Cid, L.P., M.I. Niemeyer, A. Ramirez, and F.V. Sepulveda. 2000. Splice variants of a ClC-2 chloride channel with differing functional characteristics. *Am. J. Physiol. Cell Physiol.* 279:C1198-1210.

Croll, T.I. 2018. ISOLDE: a physically realistic environment for model building into low-resolution electron-density maps. *Acta Crystallogr D Struct Biol*. 74:519-530.

De Jesus-Perez, J.J., A. Castro-Chong, R.C. Shieh, C.Y. Hernandez-Carballo, J.A. De Santiago-Castillo, and J. Arreola. 2016. Gating the glutamate gate of CLC-2 chloride channel by pore occupancy. *J. Gen. Physiol.* 147:25-37.

De Jesus-Perez, J.J., G.A. Mendez-Maldonado, A.E. Lopez-Romero, D. Esparza-Jasso, I.L. Gonzalez-Hernandez, V. De la Rosa, R. Gastelum-Garibaldi, J.E. Sanchez-Rodriguez, and J. Arreola. 2021. Electro-steric opening of the CLC-2 chloride channel gate. *Sci Rep*. 11:13127.

de Santiago, J.A., K. Nehrke, and J. Arreola. 2005. Quantitative analysis of the voltage-dependent gating of mouse parotid ClC-2 chloride channel. *J. Gen. Physiol.* 126:591-603.

Duan, D.D. 2013. Phenomics of cardiac chloride channels. *Compr Physiol*. 3:667-692.

1028 Duncan, A.R., M.M. Polovitskaya, H. Gaitan-Penas, S. Bertelli, G.E. VanNoy, P.E. Grant, A. O'Donnell-
1029 Luria, Z. Valivullah, A.K. Lovgren, E.M. England, E. Agolini, J.A. Madden, K. Schmitz-Abe, A.
1030 Kritzer, P. Hawley, A. Novelli, P. Alfieri, G.S. Colafati, D. Wieczorek, K. Platzer, J. Luppe, M. Koch-
1031 Hogrebe, R. Abou Jamra, J. Neira-Fresneda, A. Lehman, C.F. Boerkoel, K. Seath, L. Clarke, C.
1032 Study, Y. van Ierland, E. Argilli, E.H. Sherr, A. Maiorana, T. Diel, M. Hempel, T. Bierhals, R.
1033 Estevez, T.J. Jentsch, M. Pusch, and P.B. Agrawal. 2021. Unique variants in CLCN3, encoding an
1034 endosomal anion/proton exchanger, underlie a spectrum of neurodevelopmental disorders.
1035 *Am. J. Hum. Genet.* 108:1450-1465.
1036 Dutzler, R., E.B. Campbell, M. Cadene, B.T. Chait, and R. MacKinnon. 2002. X-ray structure of a ClC
1037 chloride channel at 3.0 A reveals the molecular basis of anion selectivity. *Nature*. 415:287-294.
1038 Dutzler, R., E.B. Campbell, and R. MacKinnon. 2003. Gating the selectivity filter in ClC chloride channels.
1039 *Science*. 300:108-112.
1040 Emsley, P., and K. Cowtan. 2004. Coot: model-building tools for molecular graphics. *Acta Crystallogr. D*
1041 *Biol. Crystallogr.* 60:2126-2132.
1042 Ereno-Orbea, J., I. Oyenarte, and L.A. Martinez-Cruz. 2013. CBS domains: Ligand binding sites and
1043 conformational variability. *Arch. Biochem. Biophys.* 540:70-81.
1044 Estevez, R., M. Pusch, C. Ferrer-Costa, M. Orozco, and T.J. Jentsch. 2004. Functional and structural
1045 conservation of CBS domains from CLC chloride channels. *J. Physiol.* 557:363-378.
1046 Feng, L., E.B. Campbell, Y. Hsiung, and R. MacKinnon. 2010. Structure of a eukaryotic CLC transporter
1047 defines an intermediate state in the transport cycle. *Science*. 330:635-641.
1048 Feng, L., E.B. Campbell, and R. MacKinnon. 2012. Molecular mechanism of proton transport in CLC Cl-
1049 /H+ exchange transporters. *Proc. Natl. Acad. Sci. U. S. A.* 109:11699-11704.
1050 Fernandes-Rosa, F.L., G. Daniil, I.J. Orozco, C. Goppner, R. El Zein, V. Jain, S. Boulkroun, X. Jeunemaitre,
1051 L. Amar, H. Lefebvre, T. Schwarzmayr, T.M. Strom, T.J. Jentsch, and M.C. Zennaro. 2018. A gain-
1052 of-function mutation in the CLCN2 chloride channel gene causes primary aldosteronism. *Nat.*
1053 *Genet.* 50:355-361.
1054 Furukawa, T., S. Horikawa, T. Terai, T. Ogura, Y. Katayama, and M. Hiraoka. 1995. Molecular cloning
1055 and characterization of a novel truncated from (ClC-2 beta) of ClC-2 alpha (ClC-2G) in rabbit
1056 heart. *FEBS. Lett.* 375:56-62.
1057 Gaitan-Penas, H., P.M. Apaja, T. Arnedo, A. Castellanos, X. Elorza-Vidal, D. Soto, X. Gasull, G.L. Lukacs,
1058 and R. Estevez. 2017. Leukoencephalopathy-causing CLCN2 mutations are associated with
1059 impaired Cl(-) channel function and trafficking. *J. Physiol.* 595:6993-7008.
1060 Garcia-Olivares, J., A. Alekov, M.R. Boroumand, B. Begemann, P. Hidalgo, and C. Fahlke. 2008. Gating of
1061 human ClC-2 chloride channels and regulation by carboxy-terminal domains. *J. Physiol.*
1062 586:5325-5336.
1063 Gianesello, L., D. Del Prete, M. Ceol, G. Priante, L.A. Calo, and F. Anglani. 2020. From protein uptake to
1064 Dent disease: An overview of the CLCN5 gene. *Gene*. 747:144662.
1065 Giorgio, E., G. Vaula, P. Benna, N. Lo Buono, C.M. Eandi, D. Dino, C. Mancini, S. Cavalieri, E. Di Gregorio,
1066 E. Pozzi, M. Ferrero, M.T. Giordana, C. Depienne, and A. Brusco. 2017. A novel homozygous
1067 change of CLCN2 (p.His590Pro) is associated with a subclinical form of leukoencephalopathy
1068 with ataxia (LKPAT). *J. Neurol. Neurosurg. Psychiatry*. 88:894-896.
1069 Goehring, A., C.H. Lee, K.H. Wang, J.C. Michel, D.P. Claxton, I. Baconguis, T. Althoff, S. Fischer, K.C.
1070 Garcia, and E. Gouaux. 2014. Screening and large-scale expression of membrane proteins in
1071 mammalian cells for structural studies. *Nat. Protoc.* 9:2574-2585.

1072 Goppner, C., I.J. Orozco, M.B. Hoegg-Beiler, A.H. Soria, C.A. Hubner, F.L. Fernandes-Rosa, S. Boulkroun,
1073 M.C. Zennaro, and T.J. Jentsch. 2019. Pathogenesis of hypertension in a mouse model for
1074 human CLCN2 related hyperaldosteronism. *Nat. Commun.* 10:4678.
1075 Grieschat, M., R.E. Guzman, K. Langschwager, C. Fahlke, and A.K. Alekov. 2020. Metabolic energy
1076 sensing by mammalian CLC anion/proton exchangers. *EMBO Rep.* 21:e47872.
1077 Grunder, S., A. Thiemann, M. Pusch, and T.J. Jentsch. 1992. Regions involved in the opening of CIC-2
1078 chloride channel by voltage and cell volume. *Nature*. 360:759-762.
1079 Guo, Z., T. Lu, L. Peng, H. Cheng, F. Peng, J. Li, Z. Lu, S. Chen, and W. Qiu. 2019. CLCN2-related
1080 leukoencephalopathy: a case report and review of the literature. *BMC Neurol.* 19:156.
1081 Hansen, T.H., Y. Yan, G. Ahlberg, O.B. Vad, L. Refsgaard, J.L. Dos Santos, N. Mutsaers, J.H. Svendsen,
1082 M.S. Olesen, B.H. Bentzen, and N. Schmitt. 2020. A Novel Loss-of-Function Variant in the
1083 Chloride Ion Channel Gene Clcn2 Associates with Atrial Fibrillation. *Sci Rep*. 10:1453.
1084 Huang, J., and A.D. MacKerell, Jr. 2013. CHARMM36 all-atom additive protein force field: validation
1085 based on comparison to NMR data. *J Comput Chem*. 34:2135-2145.
1086 Humphrey, W., A. Dalke, and K. Schulten. 1996. VMD: visual molecular dynamics. *J. Mol. Graph.* 14:33-
1087 38, 27-38.
1088 Jardetzky, O. 1966. Simple allosteric model for membrane pumps. *Nature*. 211:969-970.
1089 Jentsch, T.J., and M. Pusch. 2018. CLC Chloride Channels and Transporters: Structure, Function,
1090 Physiology, and Disease. *Physiol. Rev.* 98:1493-1590.
1091 Jeworutzki, E., T. Lopez-Hernandez, X. Capdevila-Nortes, S. Sirisi, L. Bengtsson, M. Montolio, G. Zifarelli,
1092 T. Arnedo, C.S. Muller, U. Schulte, V. Nunes, A. Martinez, T.J. Jentsch, X. Gasull, M. Pusch, and R.
1093 Estevez. 2012. GlialCAM, a Protein Defective in a Leukodystrophy, Serves as a ClC-2 Cl(-)
1094 Channel Auxiliary Subunit. *Neuron*. 73:951-961.
1095 Jordt, S.E., and T.J. Jentsch. 1997. Molecular dissection of gating in the ClC-2 chloride channel. *EMBO J.*
1096 16:1582-1592.
1097 Kieferle, S., P. Fong, M. Bens, A. Vandewalle, and T.J. Jentsch. 1994. Two highly homologous members
1098 of the ClC chloride channel family in both rat and human kidney. *Proc. Natl. Acad. Sci. U.S.A.*
1099 91:6943-6947.
1100 Koster, A.K., A.L. Reese, Y. Kuryshev, X. Wen, K.A. McKiernan, E.E. Gray, C. Wu, J.R. Huguenard, M.
1101 Maduke, and J. Du Bois. 2020. Development and validation of a potent and specific inhibitor for
1102 the CLC-2 chloride channel. *Proc. Natl. Acad. Sci. U. S. A.*
1103 Lein, E.S., M.J. Hawrylycz, N. Ao, M. Ayres, A. Bensinger, A. Bernard, A.F. Boe, M.S. Boguski, K.S.
1104 Brockway, E.J. Byrnes, L. Chen, L. Chen, T.M. Chen, M.C. Chin, J. Chong, B.E. Crook, A.
1105 Czaplinska, C.N. Dang, S. Datta, N.R. Dee, A.L. Desaki, T. Desta, E. Diep, T.A. Dolbeare, M.J.
1106 Donelan, H.W. Dong, J.G. Dougherty, B.J. Duncan, A.J. Ebbert, G. Eichele, L.K. Estin, C. Faber,
1107 B.A. Facer, R. Fields, S.R. Fischer, T.P. Fliss, C. Frensley, S.N. Gates, K.J. Glattfelder, K.R.
1108 Halverson, M.R. Hart, J.G. Hohmann, M.P. Howell, D.P. Jeung, R.A. Johnson, P.T. Karr, R. Kawal,
1109 J.M. Kidney, R.H. Knapik, C.L. Kuan, J.H. Lake, A.R. Laramee, K.D. Larsen, C. Lau, T.A. Lemon, A.J.
1110 Liang, Y. Liu, L.T. Luong, J. Michaels, J.J. Morgan, R.J. Morgan, M.T. Mortrud, N.F. Mosqueda,
1111 L.L. Ng, R. Ng, G.J. Orta, C.C. Overly, T.H. Pak, S.E. Parry, S.D. Pathak, O.C. Pearson, R.B.
1112 Puchalski, Z.L. Riley, H.R. Rockett, S.A. Rowland, J.J. Royall, M.J. Ruiz, N.R. Sarno, K. Schaffnit,
1113 N.V. Shapovalova, T. Sivisay, C.R. Slaughterbeck, S.C. Smith, K.A. Smith, B.I. Smith, A.J. Sodt,
1114 N.N. Stewart, K.R. Stumpf, S.M. Sunkin, M. Sutram, A. Tam, C.D. Teemer, C. Thaller, C.L.
1115 Thompson, L.R. Varnam, A. Visel, R.M. Whitlock, P.E. Wohnoutka, C.K. Wolkey, V.Y. Wong, M.
1116 Wood, M.B. Yaylaoglu, R.C. Young, B.L. Youngstrom, X.F. Yuan, B. Zhang, T.A. Zwingman, and

1117 A.R. Jones. 2007. Genome-wide atlas of gene expression in the adult mouse brain. *Nature*.
1118 445:168-176.
1119 Leisle, L., Y. Xu, E. Fortea, S. Lee, J.D. Galpin, M. Vien, C.A. Ahern, A. Accardi, and S. Berneche. 2020.
1120 Divergent Cl(-) and H(+) pathways underlie transport coupling and gating in CLC exchangers and
1121 channels. *Elife*. 9.
1122 Liebschner, D., P.V. Afonine, M.L. Baker, G. Bunkoczi, V.B. Chen, T.I. Croll, B. Hintze, L.W. Hung, S. Jain,
1123 A.J. McCoy, N.W. Moriarty, R.D. Oeffner, B.K. Poon, M.G. Prisant, R.J. Read, J.S. Richardson, D.C.
1124 Richardson, M.D. Sammito, O.V. Sobolev, D.H. Stockwell, T.C. Terwilliger, A.G. Urzhumtsev, L.L.
1125 Videau, C.J. Williams, and P.D. Adams. 2019. Macromolecular structure determination using X-
1126 rays, neutrons and electrons: recent developments in Phenix. *Acta Crystallogr D Struct Biol*.
1127 75:861-877.
1128 Liebschner, D., N.W. Moriarty, B.K. Poon, and P.D. Adams. 2023. In situ ligand restraints from quantum-
1129 mechanical methods. *Acta Crystallogr D Struct Biol*. 79:100-110.
1130 Lin, Y.W., C.W. Lin, and T.Y. Chen. 1999. Elimination of the slow gating of ClC-0 chloride channel by a
1131 point mutation. *J. Gen. Physiol.* 114:1-12.
1132 Lisal, J., and M. Maduke. 2008. The ClC-0 chloride channel is a 'broken' Cl-/H+ antiporter. *Nat. Struct.*
1133 *Mol. Biol.* 15:805-810.
1134 Ma, L., G.Y. Rychkov, E.A. Bykova, J. Zheng, and A.H. Bretag. 2011. Movement of hClC-1 C-termini
1135 during common gating and limits on their cytoplasmic location. *Biochem. J.* 436:415-428.
1136 Ma, T., L. Wang, A. Chai, C. Liu, W. Cui, S. Yuan, S. Wing Ngor Au, L. Sun, X. Zhang, Z. Zhang, J. Lu, Y.
1137 Gao, P. Wang, Z. Li, Y. Liang, H. Vogel, Y.T. Wang, D. Wang, K. Yan, and H. Zhang. 2023. Cryo-EM
1138 structures of ClC-2 chloride channel reveal the blocking mechanism of its specific inhibitor AK-
1139 42. *Nat. Commun.* 14:3424.
1140 Maduke, M.C., and R.J. Reimer. 2012. Biochemistry to the rescue: a ClC-2 auxiliary subunit provides a
1141 tangible link to leukodystrophy. *Neuron*. 73:855-857.
1142 Miller, C. 1982. Open-state substructure of single chloride channels from Torpedo electroplax. *Philos.*
1143 *Trans. R. Soc. Lond. B. Biol. Sci.* 299:401-411.
1144 Miller, C. 2006. ClC chloride channels viewed through a transporter lens. *Nature*. 440:484-489.
1145 Miller, C. 2021. Q-cubed mutant cues clues to CLC antiport mechanism. *J. Gen. Physiol.* 153.
1146 Morozenko, A., and A.A. Stuchebrukhov. 2016. Dowser++, a new method of hydrating protein
1147 structures. *Proteins*. 84:1347-1357.
1148 Nicoli, E.R., M.R. Weston, M. Hackbarth, A. Becerril, A. Larson, W.M. Zein, P.R. Baker, 2nd, J.D. Burke,
1149 H. Dorward, M. Davids, Y. Huang, D.R. Adams, P.M. Zerfas, D. Chen, T.C. Markello, C. Toro, T.
1150 Wood, G. Elliott, M. Vu, N. Undiagnosed Diseases, W. Zheng, L.J. Garrett, C.J. Tifft, W.A. Gahl,
1151 D.L. Day-Salvatore, J.A. Mindell, and M.C.V. Malicdan. 2019. Lysosomal Storage and Albinism
1152 Due to Effects of a De Novo CLCN7 Variant on Lysosomal Acidification. *Am. J. Hum. Genet.*
1153 104:1127-1138.
1154 Niemeyer, M.I., L.P. Cid, Y.R. Yusef, R. Briones, and F.V. Sepulveda. 2009. Voltage-dependent and -
1155 independent titration of specific residues accounts for complex gating of a ClC chloride channel
1156 by extracellular protons. *J. Physiol.* 587:1387-1400.
1157 Niemeyer, M.I., L.P. Cid, L. Zuniga, M. Catalan, and F.V. Sepulveda. 2003. A conserved pore-lining
1158 glutamate as a voltage- and chloride-dependent gate in the ClC-2 chloride channel. *J. Physiol.*
1159 553:873-879.

1160 Nighot, P.K., L. Leung, and T.Y. Ma. 2017. Chloride channel ClC- 2 enhances intestinal epithelial tight
1161 junction barrier function via regulation of caveolin-1 and caveolar trafficking of occludin. *Exp.*
1162 *Cell Res.* 352:113-122.
1163 Nishikawa, K.O., T.; Isogai, Y.; Saitô, N. 1972. Tertiary Structure of Proteins. I. Representation and
1164 Computation of the Conformations. *Journal of the physical society of Japan*. 32.
1165 Okamoto, Y., Y. Nagasawa, Y. Obara, K. Ishii, D. Takagi, and K. Ono. 2019. Molecular identification of
1166 HSPA8 as an accessory protein of a hyperpolarization-activated chloride channel from rat
1167 pulmonary vein cardiomyocytes. *J. Biol. Chem.* 294:16049-16061.
1168 Palmer, E.E., M. Pusch, A. Picollo, C. Forwood, M.H. Nguyen, V. Suckow, J. Gibbons, A. Hoff, L. Sigfrid, A.
1169 Megarbane, M. Nizon, B. Cogne, C. Beneteau, F.S. Alkuraya, A. Chedrawi, M.O. Hashem, H.
1170 Stamberger, S. Weckhuysen, A. Vanlander, B. Ceulemans, S. Rajagopalan, K. Nunn, S. Arpin, M.
1171 Raynaud, C.S. Motter, C. Ward-Melver, K. Janssens, M. Meuwissen, D. Beysen, N. Dikow, M.
1172 Grimmel, T.B. Haack, E. Clement, A. McTague, D. Hunt, S. Townshend, M. Ward, L.J. Richards, C.
1173 Simons, G. Costain, L. Dupuis, R. Mendoza-Londono, T. Dudding-Byth, J. Boyle, C. Saunders, E.
1174 Fleming, S. El Chehadeh, M.A. Spitz, A. Piton, B. Gerard, M.T. Abi Warde, G. Rea, C. McKenna, S.
1175 Douzgou, S. Banka, C. Akman, J.M. Bain, T.T. Sands, G.N. Wilson, E.J. Silvertooth, L. Miller, D.
1176 Lederer, R. Sachdev, R. Macintosh, O. Monestier, D. Karadurmus, F. Collins, M. Carter, L.
1177 Rohena, M.H. Willemsen, C.W. Ockeloen, R. Pfundt, S.D. Kroft, M. Field, F.E.R. Laranjeira, A.M.
1178 Fortuna, A.R. Soares, V. Michaud, S. Naudion, S. Golla, D.D. Weaver, L.M. Bird, J. Friedman, V.
1179 Clowes, S. Joss, L. Polsler, P.M. Campeau, M. Blazo, E.K. Bijlsma, J.A. Rosenfeld, C. Beetz, Z.
1180 Powis, K. McWalter, T. Brandt, E. Torti, M. Mathot, S.S. Mohammad, R. Armstrong, and V.M.
1181 Kalscheuer. 2023. Functional and clinical studies reveal pathophysiological complexity of
1182 CLCN4-related neurodevelopmental condition. *Mol. Psychiatry*. 28:668-697.
1183 Park, E., E.B. Campbell, and R. MacKinnon. 2017. Structure of a CLC chloride ion channel by cryo-
1184 electron microscopy. *Nature*. 541:500-505.
1185 Park, E., and R. MacKinnon. 2018. Structure of the CLC-1 chloride channel from Homo sapiens. *Elife*. 7.
1186 Park, K., J. Arreola, T. Begenisich, and J.E. Melvin. 1998. Comparison of voltage-activated Cl- channels in
1187 rat parotid acinar cells with ClC-2 in a mammalian expression system. *J. Membr. Biol.* 163:87-95.
1188 Paul, J., S. Jeyaraj, S.M. Huber, G. Seebohm, C. Bohmer, F. Lang, P.G. Kremsner, and J.F. Kun. 2007.
1189 Alterations in the cytoplasmic domain of CLCN2 result in altered gating kinetics. *Cell. Physiol.*
1190 *Biochem.* 20:441-454.
1191 Pettersen, E.F., T.D. Goddard, C.C. Huang, G.S. Couch, D.M. Greenblatt, E.C. Meng, and T.E. Ferrin.
1192 2004. UCSF Chimera--a visualization system for exploratory research and analysis. *J Comput*
1193 *Chem*. 25:1605-1612.
1194 Picollo, A., M. Malvezzi, J.C. Houtman, and A. Accardi. 2009. Basis of substrate binding and
1195 conservation of selectivity in the CLC family of channels and transporters. *Nat. Struct. Mol. Biol.*
1196 16:1294-1301.
1197 Pintilie, G., K. Zhang, Z. Su, S. Li, M.F. Schmid, and W. Chiu. 2020. Measurement of atom resolvability in
1198 cryo-EM maps with Q-scores. *Nat. Methods*. 17:328-334.
1199 Pusch, M., S. Jordt, V. Stein, and T.J. Jentsch. 1999. Chloride dependence of hyperpolarization-activated
1200 chloride channel gates. *J. Physiol.* 515:341-353.
1201 Pusch, M., U. Ludewig, and T.J. Jentsch. 1997. Temperature dependence of fast and slow gating
1202 relaxations of ClC-0 chloride channels. *J. Gen. Physiol.* 109:105-116.
1203 Pusch, M., U. Ludewig, A. Rehfeldt, and T.J. Jentsch. 1995. Gating of the voltage-dependent chloride
1204 channel CIC-0 by the permeant anion. *Nature*. 373:527-531.

1205 Roe, D.R., and T.E. Cheatham, 3rd. 2013. PTRAJ and CPPTRAJ: Software for Processing and Analysis of
1206 Molecular Dynamics Trajectory Data. *Journal of chemical theory and computation*. 9:3084-3095.
1207 Saint-Martin, C., G. Gauvain, G. Teodorescu, I. Gourfinkel-An, E. Fedirko, Y.G. Weber, S. Maljevic, J.P.
1208 Ernst, J. Garcia-Olivares, C. Fahlke, R. Nabbout, E. LeGuern, H. Lerche, J.C. Poncer, and C.
1209 Depienne. 2009. Two novel CLCN2 mutations accelerating chloride channel deactivation are
1210 associated with idiopathic generalized epilepsy. *Hum. Mutat.* 30:397-405.
1211 Salomon-Ferrer, R., A.W. Gotz, D. Poole, S. Le Grand, and R.C. Walker. 2013. Routine Microsecond
1212 Molecular Dynamics Simulations with AMBER on GPUs. 2. Explicit Solvent Particle Mesh Ewald.
1213 *Journal of chemical theory and computation*. 9:3878-3888.
1214 Sanchez-Rodriguez, J.E., J.A. De Santiago-Castillo, and J. Arreola. 2010. Permeant anions contribute to
1215 voltage dependence of ClC-2 chloride channel by interacting with the protopore gate. *J. Physiol.*
1216 588:2545-2556.
1217 Sanchez-Rodriguez, J.E., J.A. De Santiago-Castillo, J.A. Contreras-Vite, P.G. Nieto-Delgado, A. Castro-
1218 Chong, and J. Arreola. 2012. Sequential interaction of chloride and proton ions with the fast
1219 gate steer the voltage-dependent gating in ClC-2 chloride channels. *J. Physiol.* 590:4239-4253.
1220 Scholl, U.I., G. Stolting, J. Schewe, A. Thiel, H. Tan, C. Nelson-Williams, A.A. Vichot, S.C. Jin, E. Loring, V.
1221 Untiet, T. Yoo, J. Choi, S. Xu, A. Wu, M. Kirchner, P. Mertins, L.C. Rump, A.M. Onder, C. Gamble,
1222 D. McKenney, R.W. Lash, D.P. Jones, G. Chune, P. Gagliardi, M. Choi, R. Gordon, M. Stowasser,
1223 C. Fahlke, and R.P. Lifton. 2018. CLCN2 chloride channel mutations in familial
1224 hyperaldosteronism type II. *Nat. Genet.* 50:349-354.
1225 Schrecker, M., J. Korobenko, and R.K. Hite. 2020. Cryo-EM structure of the lysosomal chloride-proton
1226 exchanger CLC-7 in complex with OSTM1. *Elife*. 9.
1227 Sepela, R.J., and J.T. Sack. 2018. Taming unruly chloride channel inhibitors with rational design. *Proc.*
1228 *Natl. Acad. Sci. U. S. A.* 115:5311-5313.
1229 Steinmeyer, K., C. Ortland, and T.J. Jentsch. 1991. Primary structure and functional expression of a
1230 developmentally regulated skeletal muscle chloride channel. *Nature*. 354:301-304.
1231 Stolting, G., M. Fischer, and C. Fahlke. 2014. CLC channel function and dysfunction in health and
1232 disease. *Front Physiol*. 5:378.
1233 Stolting, G., G. Teodorescu, B. Begemann, J. Schubert, R. Nabbout, M.R. Toliat, T. Sander, P. Nurnberg,
1234 H. Lerche, and C. Fahlke. 2013. Regulation of ClC-2 gating by intracellular ATP. *Pflugers Arch.*
1235 465:1423-1437.
1236 Suomivuori, C.M., N.R. Latorraca, L.M. Wingler, S. Eismann, M.C. King, A.L.W. Kleinhenz, M.A. Skiba,
1237 D.P. Staus, A.C. Kruse, R.J. Lefkowitz, and R.O. Dror. 2020. Molecular mechanism of biased
1238 signaling in a prototypical G protein-coupled receptor. *Science*. 367:881-887.
1239 Thiemann, A., S. Grunder, M. Pusch, and T.J. Jentsch. 1992. A chloride channel widely expressed in
1240 epithelial and non-epithelial cells. *Nature*. 356:57-60.
1241 Varela, D., M.I. Niemeyer, L.P. Cid, and F.V. Sepulveda. 2002. Effect of an N-terminus deletion on
1242 voltage-dependent gating of the ClC-2 chloride channel. *J. Physiol.* 544:363-372.
1243 Wang, H., M. Xu, Q. Kong, P. Sun, F. Yan, W. Tian, and X. Wang. 2017. Research and progress on ClC2
1244 (Review). *Mol Med Rep*. 16:11-22.
1245 Wang, K., S.S. Preisler, L. Zhang, Y. Cui, J.W. Missel, C. Gronberg, K. Gotfryd, E. Lindahl, M. Andersson,
1246 K. Calloe, P.F. Egea, D.A. Klaerke, M. Pusch, P.A. Pedersen, Z.H. Zhou, and P. Gourdon. 2019.
1247 Structure of the human ClC-1 chloride channel. *PLoS Biol.* 17:e3000218.
1248 Xu, P., Z. Chen, J. Ma, Y. Shan, Y. Wang, B. Xie, D. Zheng, F. Guo, X. Song, G. Gao, K. Ye, Y. Liu, G. Pan, B.
1249 Jiang, F. Peng, and X. Zhong. 2023. Biallelic CLCN2 mutations cause retinal degeneration by

1250 impairing retinal pigment epithelium phagocytosis and chloride channel function. *Hum. Genet.*
1251 142:577-593.
1252 Yamada, T., M. Krzeminski, Z. Bozoky, J.D. Forman-Kay, and K. Strange. 2016. Role of CBS and Bateman
1253 Domains in Phosphorylation-Dependent Regulation of a CLC Anion Channel. *Biophys. J.*
1254 111:1876-1886.
1255 Yusef, Y.R., L. Zuniga, M. Catalan, M.I. Niemeyer, L.P. Cid, and F.V. Sepulveda. 2006. Removal of gating
1256 in voltage-dependent ClC-2 chloride channel by point mutations affecting the pore and C-
1257 terminus CBS-2 domain. *J. Physiol.* 572:173-181.
1258 Zagotta, W.N., T. Hoshi, and R.W. Aldrich. 1990. Restoration of inactivation in mutants of Shaker
1259 potassium channels by a peptide derived from ShB [see comments]. *Science*. 250:568-571.
1260 Zifarelli, G. 2022. The Role of the Lysosomal Cl(-)/H(+) Antiporter ClC-7 in Osteopetrosis and
1261 Neurodegeneration. *Cells*. 11.
1262 Zuniga, L., M.I. Niemeyer, D. Varela, M. Catalan, L.P. Cid, and F.V. Sepulveda. 2004. The voltage-
1263 dependent ClC-2 chloride channel has a dual gating mechanism. *J. Physiol.* 555:671-682.
1264

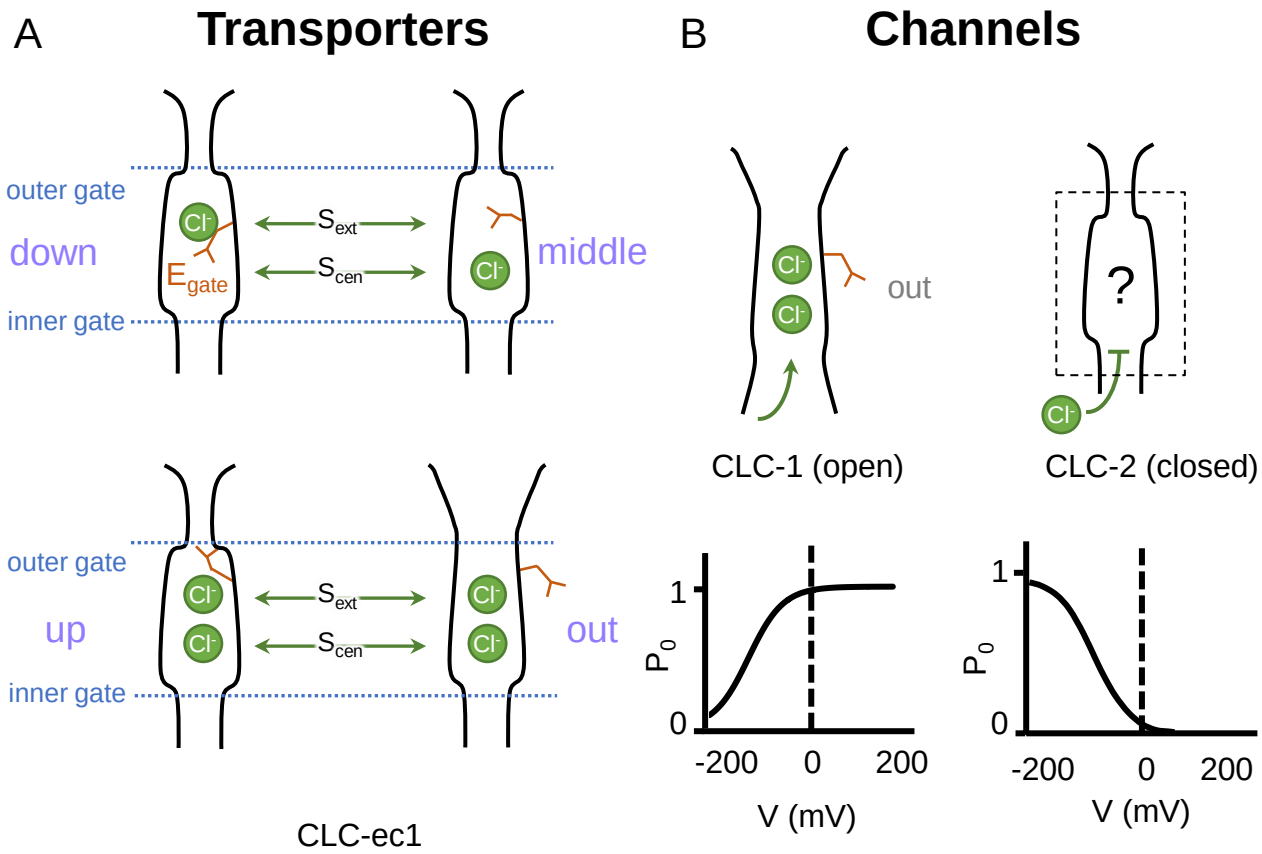

Figure 1. Gating conformations in CLC transporters and channels. (**A**) Cartoon depictions of the CLC anion-permeation pathway. The "gating glutamate" (E_{gate}) can occupy anion binding sites within the permeation pathway ("down" and "middle" conformations, occupying the central (S_{cen}) and external (S_{ext}) anion-binding sites respectively) or away from these sites ("up" and "out" conformations). Coupling of E_{gate} movement to Cl^-/H^+ binding/unbinding and global conformational change generates 2:1 Cl^-/H^+ exchange. (**B**) E_{gate} is required for voltage-dependent gating in CLC channels but has been observed structurally only in CLC-1 (PDB ID: 6coy), in the "out" position. In contrast to CLC-1, which is predominantly open at zero mV, CLC-2 is predominantly closed. The open probability (P_o) versus voltage (V) traces are based on published data reported for CLC-1 (Lisal and Maduke, 2008) and CLC-2 (Stolting et al., 2013).

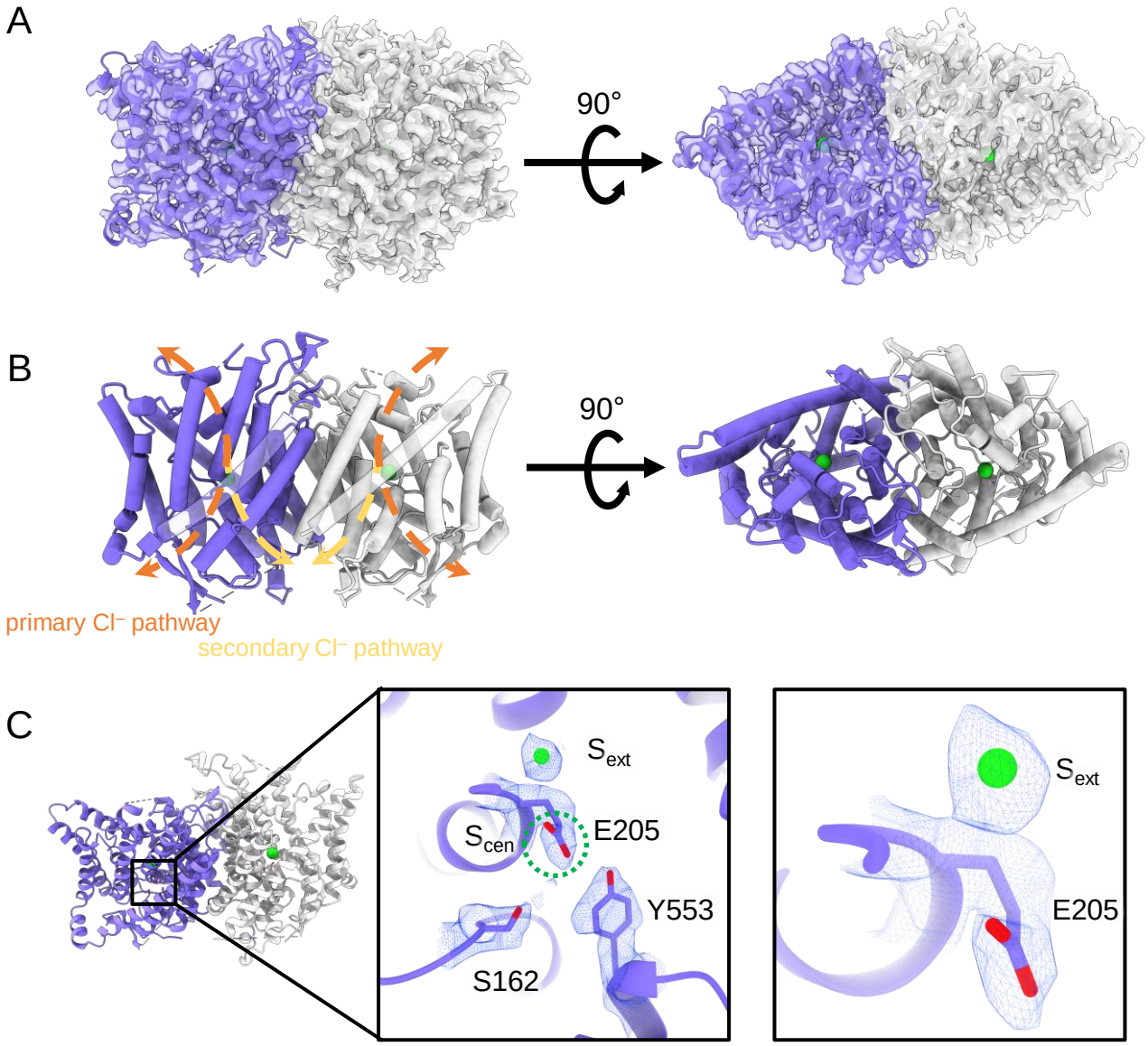

Figure 2. CryoEM structure of the human CLC-2 channel. Overall structure of the transmembrane domain ("CLC2-TM") at 2.46 Å. The identical subunits of the homodimer are shown in purple and gray, Cl^- ions are shown as green balls. (**A**) cryoEM density map with model overlay (contour level: 0.71, 5.5 σ) and (**B**) model only with dashed arrows indicating the locations of pathways detected by Caver: orange, primary Cl^- pathway common to all CLCs; yellow, secondary Cl^- pathway detected in CLC-2 and CLC-1. Details of the pathways are presented in Figure 3. The secondary pathway, whose function is not yet known, was so named when first observed in the CLC-1 structure (Park and MacKinnon, 2018). (**C**) Zoomed-in views showing cryoEM density overlay of bound Cl^- and key residues – E_{gate} (E205) and inner-gate residues Ser_C (S162) and Tyr_C (Y553). S_{cen} is indicated with a green dashed circle. Contour level: 1.1, 7.2 σ (middle panel); 0.97, 6.3 σ (right panel).

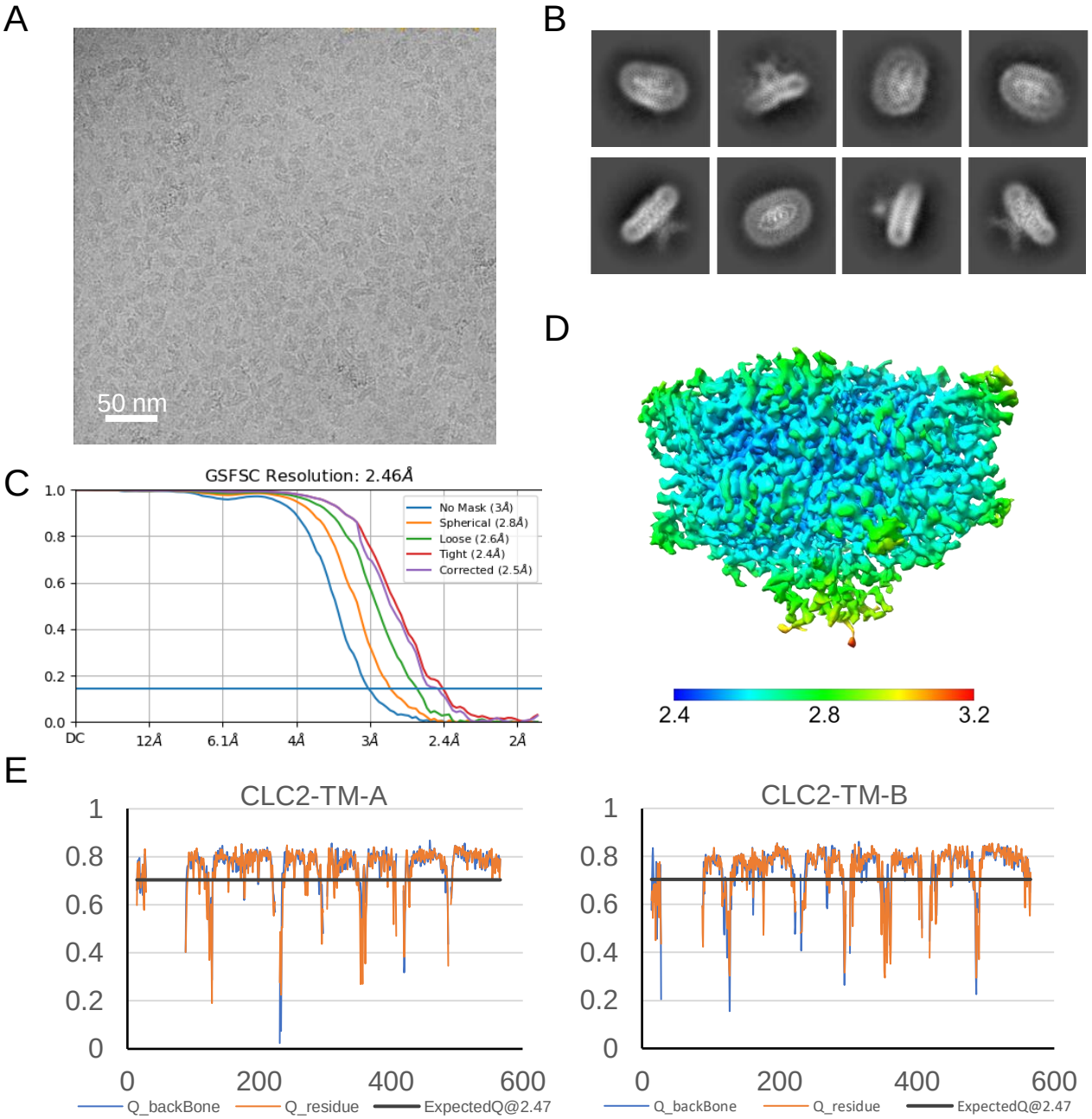

Figure 2 - figure supplement 1. Micrograph and 2D classes and structure validation of CLC2-TM. (**A**) Representative motion-corrected cryo-EM micrograph. (**B**) 2D class averages. (**C**) Gold standard FSC plots calculated in cryoSPARC. (**D**) Local resolution of the cryo-EM map of the CLC2-TM. (**E**) Model validation using Q-scores (Pintilie et al., 2020) of subunit A (left) and subunit B (right). The black line represents the expected Q-score at respective resolution based on the correlation between Q-scores and map resolution.

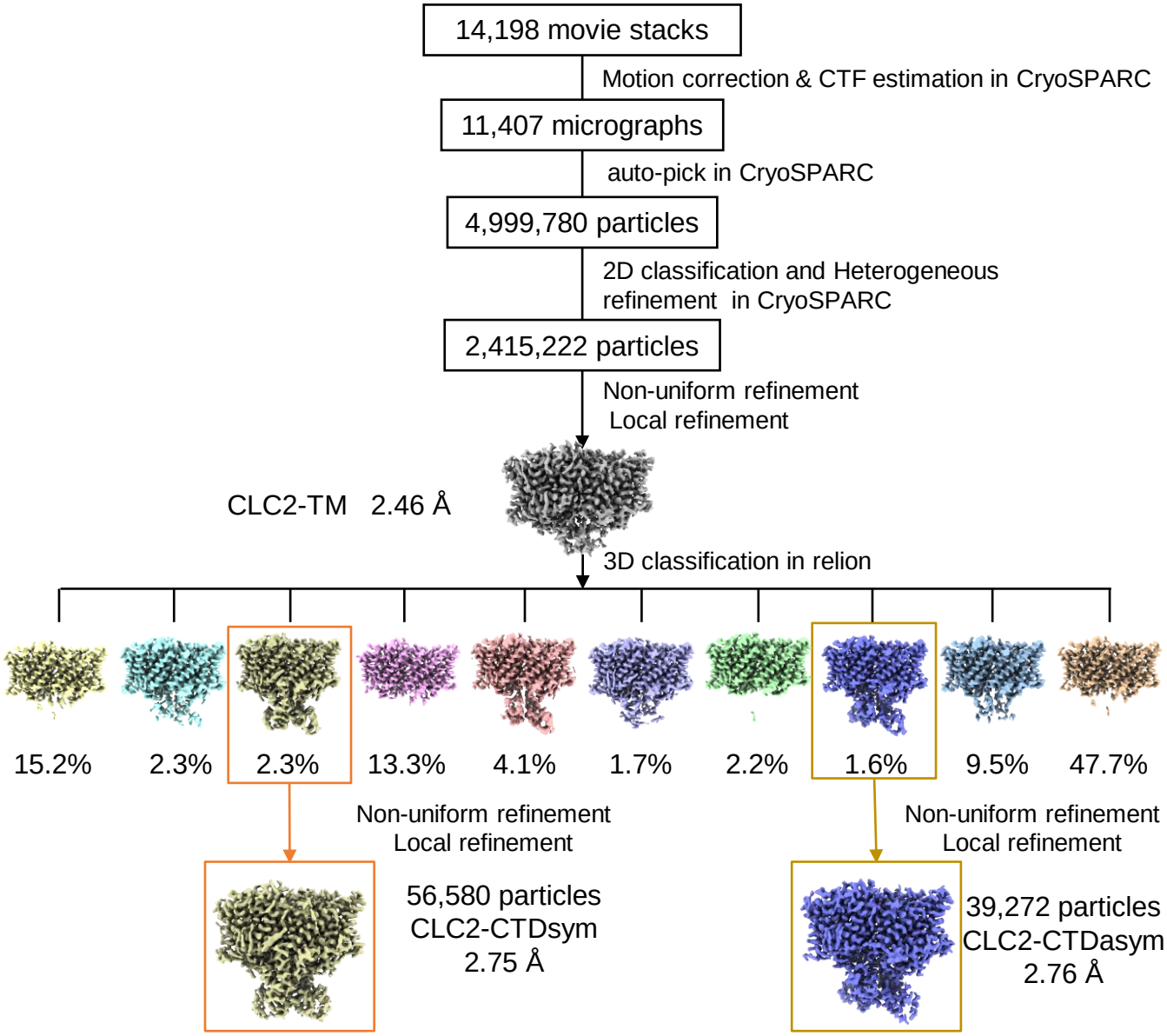

Figure 2 - figure supplement 2. CryoEM workflow of the CLC2 single-particle cryoEM data processing. A total of 14,198 movie stacks were collected on a 300 kV Titan Krios cryo-electron microscope. cryoSPRAC was used for 2D classification, and the CLC2-TM density map was obtained after 2D classification. Relion was used for 3D classification and yielded two conformations differing in the CTD: CLC2-CTDsym and CLC2-CTDasym. Resolutions shown refer to the whole protein molecule.

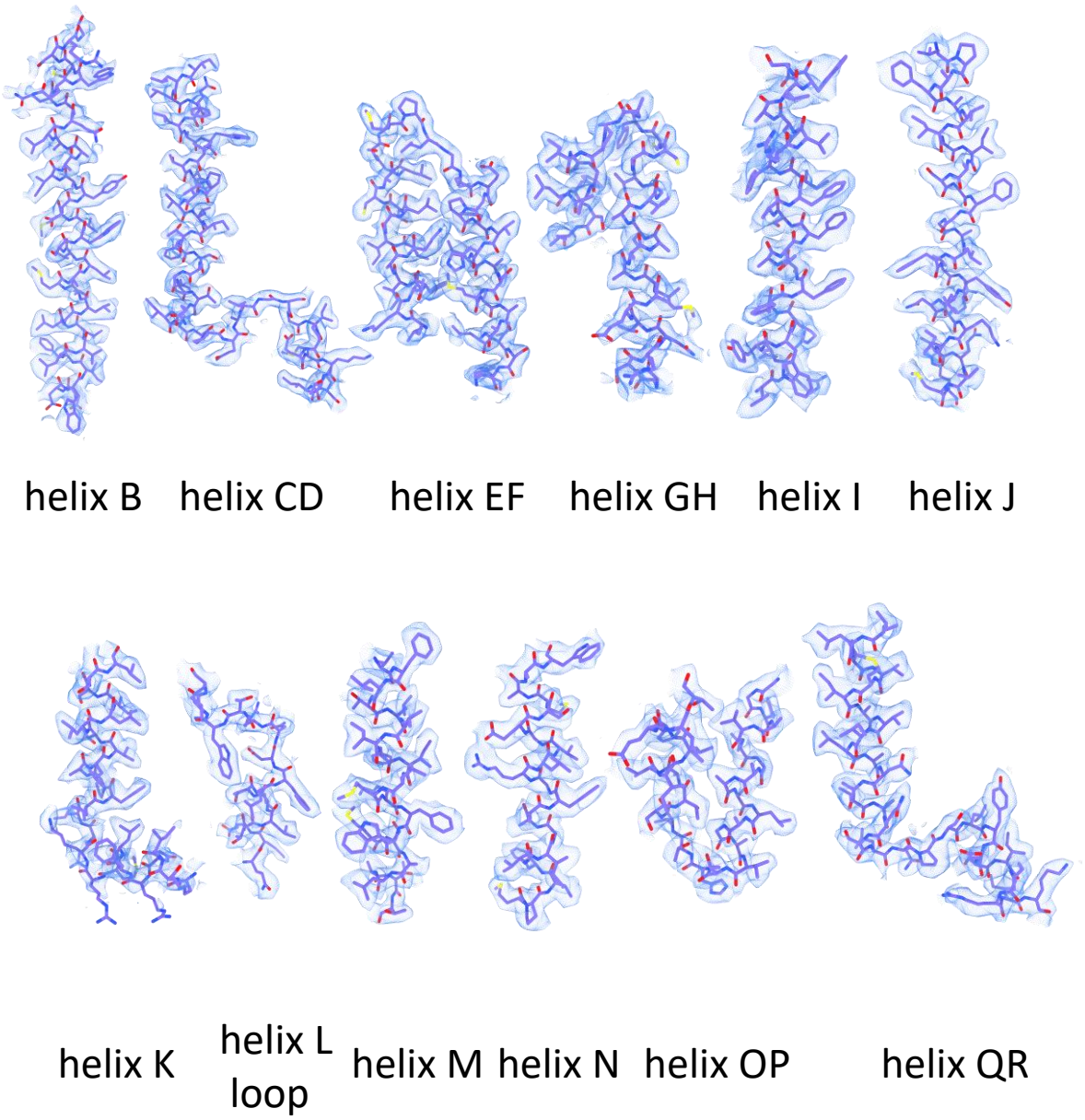

Figure 2 - figure supplement 3. Helix map of CLC2-TM. cryo-EM densities and model of CLC-2 transmembrane helices.

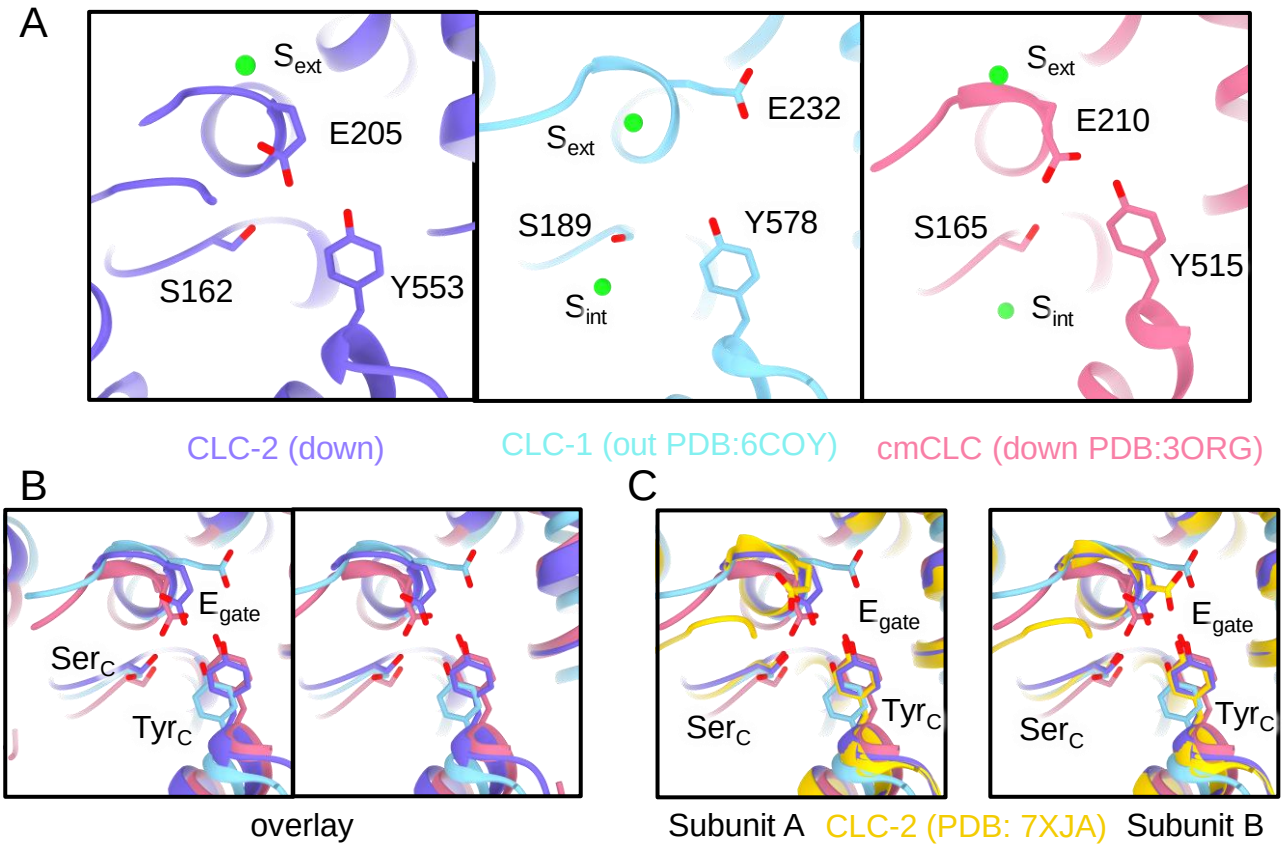

Figure 2 - figure supplement 4. E_{gate} position and Cl^- binding sites (S_{ext} and S_{cen}). (**A**) Comparison between CLC-2 (purple), CLC-1 (light blue), and cmCLC (salmon pink). E_{gate} (E205 in CLC-2, E232 in CLC-1, and E210 in cmCLC), Ser_C (S162 in CLC2, S189 in CLC-1, and S165 in cmCLC) and Tyr_C (Y553 in CLC-2, Y578 in CLC-1, and Y515 in cmCLC) are shown as sticks. In CLC-2 and cmCLC, S_{ext} is occupied by Cl^-, and S_{cen} is occupied by E_{gate}. E_{gate} is in the "down" position. In CLC-1, S_{ext} is occupied by Cl^-, and S_{cen} lacks anion density. E_{gate} is in the "out" position, away from the Cl^--permeation pathway. (**B**) Overlay view (stereo) of panel **A**. (**C**) Overlay with the CLC-2 E_{gate} conformations modeled in PDB ID: 7XJA (Ma et al., 2023).

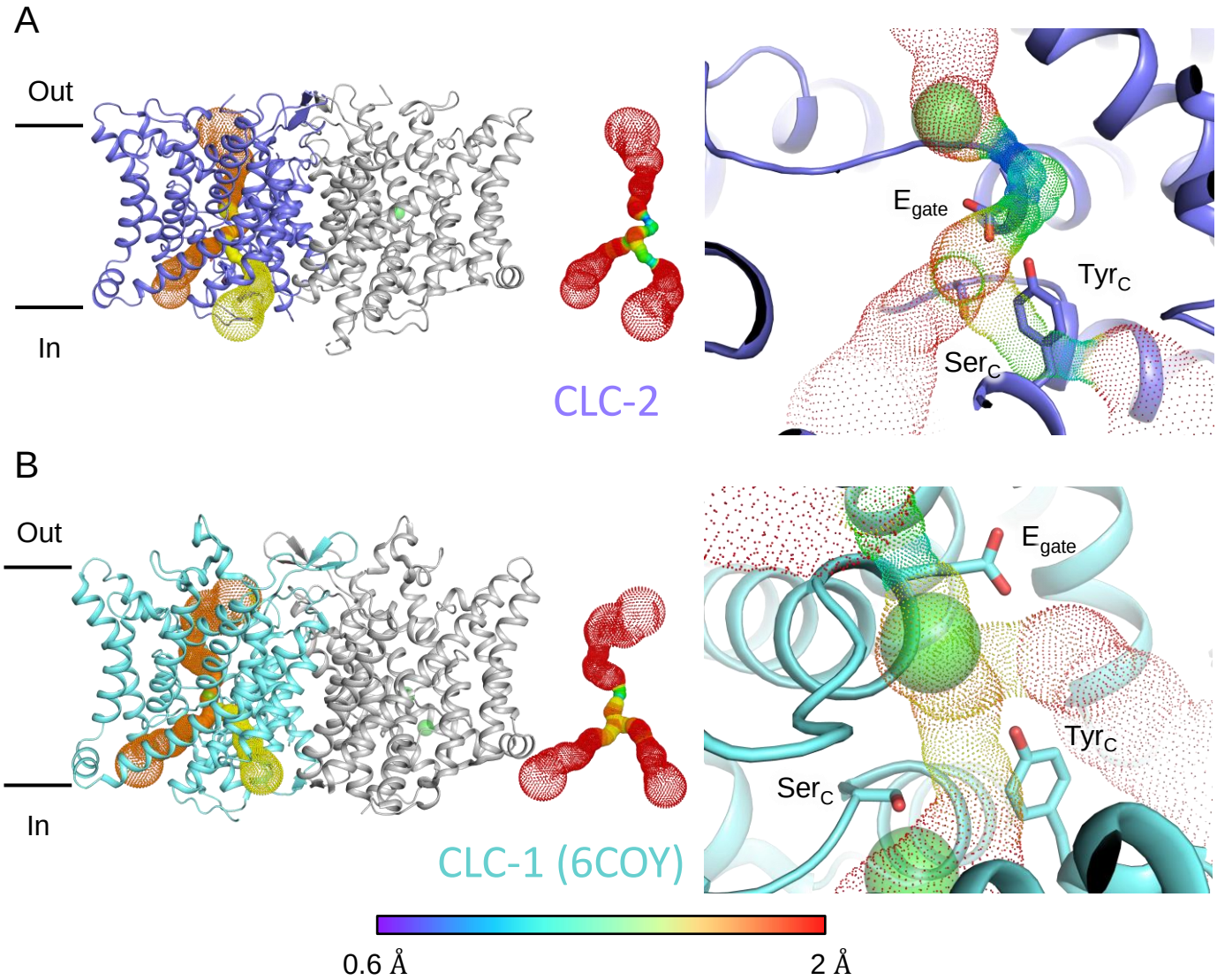

Figure 3 Pore profile detected in CLC-2. (**A**) Left: The primary (orange) and secondary (yellow) pore detected in CLC-2 using Caver. Middle: The detected pore radii are displayed in dots as a color map. Right: Zoomed-in view of the restricted (narrowest) site of the pore profile, using the same coloring as in the middle panel. E_{gate}, Ser_C and Tyr_C are shown as sticks. (**B**) Pore profile for CLC-1 (PDB ID:6coy), with display as in panel **A**.

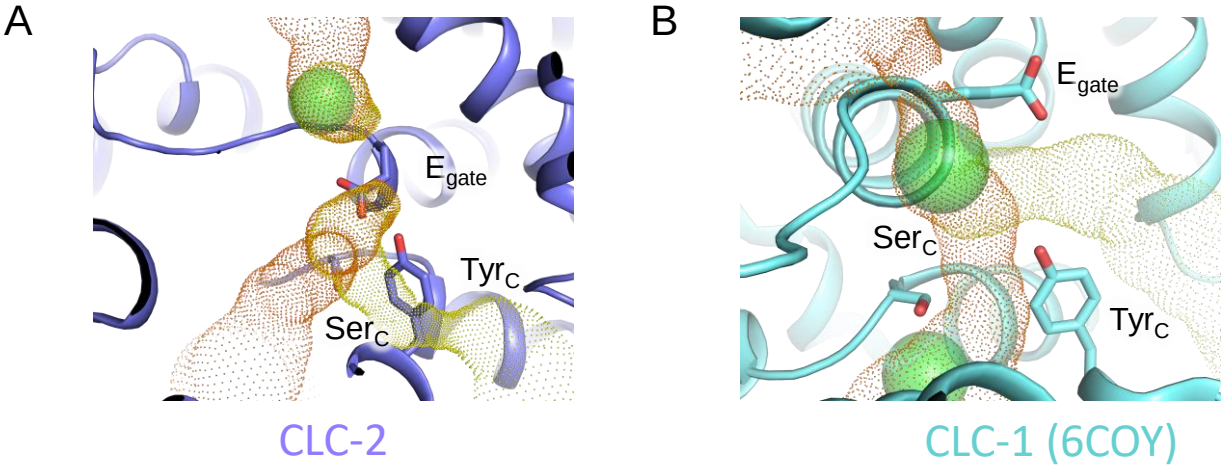

Figure 3 - figure supplement 1. Cl^- pathway in CLC-2 and CLC-1. (**A**) CLC-2 Cl^- pathway as shown in Figure 3 but omitting sections with pore radius less than 1Å. E_{gate}, occupying the S_{cen} site, blocks the canonical Cl^- pathway. (**B**) same as panel A, for CLC-1 (PDB ID:6coy).

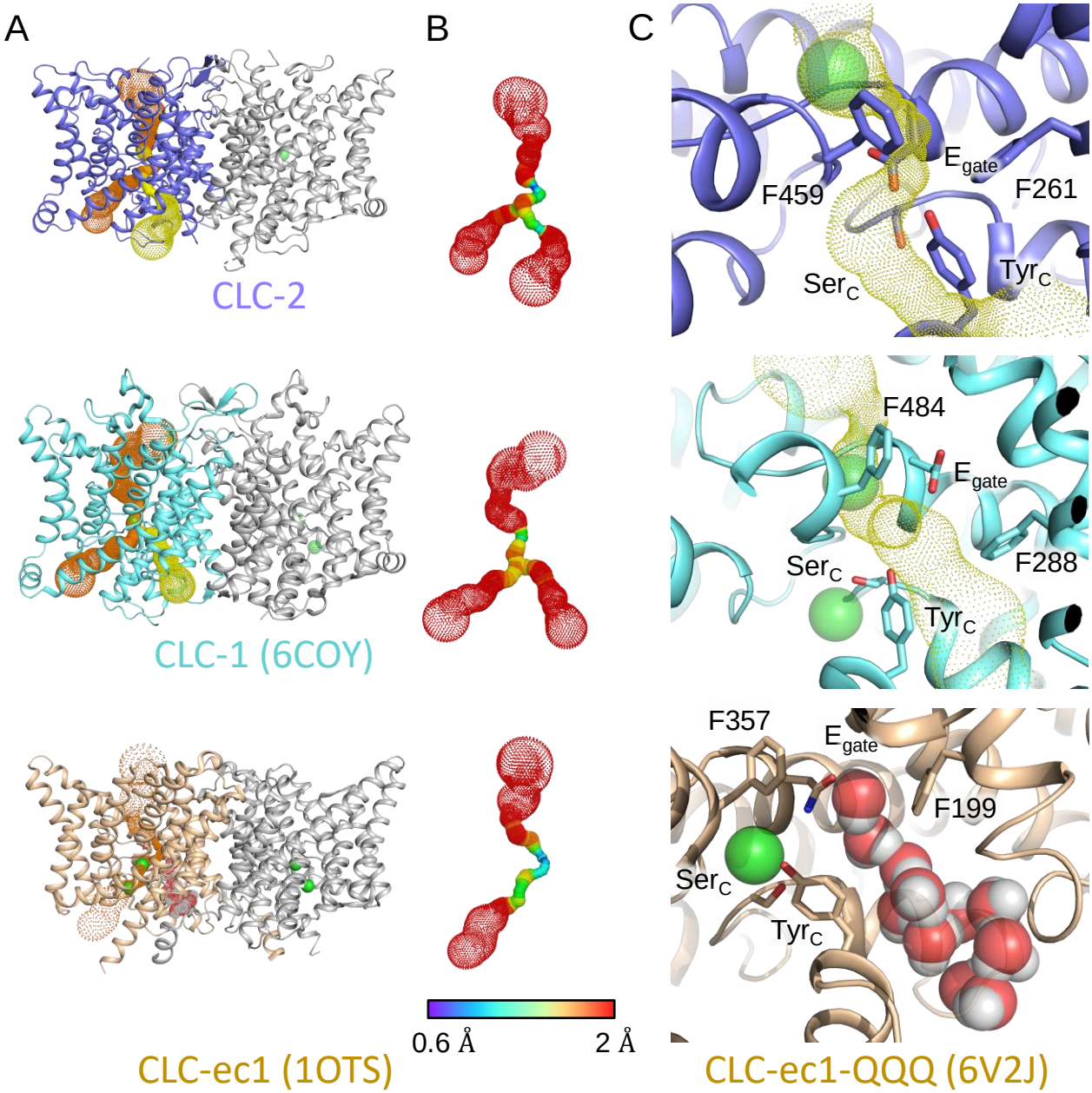

Figure 3 - figure supplement 2. Comparison of primary and secondary Cl^- pathways with transporter Cl^- and H^+ pathways. (**A**) The top two panels are repeated from Figure 3A, indicating the primary (orange) and secondary (yellow) caver-detected pores in CLC-1 and CLC-2. The lower panel shows CLC-ec1 (PDB ID: 1OTS), a representative for the CLC transporters, where caver detects only the primary pore (orange dots as for CLC-1 and CLC-2). (**B**) Detected pore radii show a longer constriction in the CLC-ec1 transporter compared to the CLC-1 and CLC-2 channels. (**C**) Zoomed-in view of the secondary-pore region for CLC-2 (top), CLC-1 (middle) and CLC-ec1 (bottom). The CLC-ec1 panel shows water wires (space-filled) detected in simulations of the QQQ mutant structure (PDB ID: 6V2J) (Chavan et al., 2020).

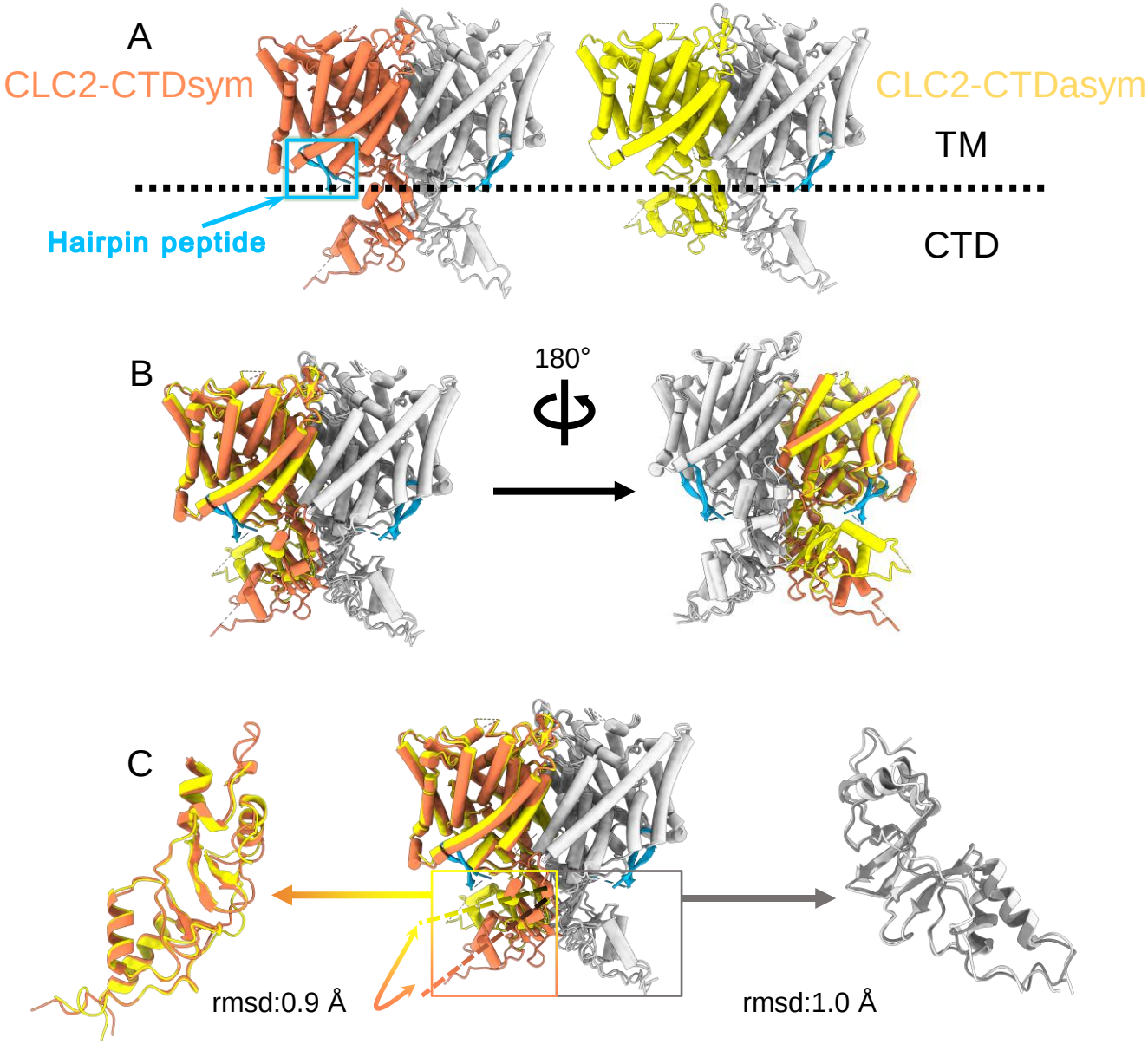

Figure 4. Different conformations of the CTD. (**A**). Overall structure of the two CLC-2 conformations. Left: CLC2-CTDsym at 2.75 Å. Right: CLC2-CTDasym at 2.76 Å. The subunits of the homodimer are shown in orange (CLC2-CTDsym) or yellow (CLC2-CTDasym) and gray (for both). The subunits adopting different CTD conformations are shown in orange and yellow, while the subunits sharing the same CTD conformation are shown in gray. The dashed line demarcates the transmembrane (TM) and cytoplasmic (CTD) domains. A hairpin structure detected at the intracellular pore is shown in blue. (**B**) Overlay of two conformations. (**C**) Hinge movement of the CTD between two conformations. The middle panel shows an overlay of CLC2-CTDsym (orange and gray) and CLC1-CTDasym (yellow and gray), with the CTDs highlighted in boxes. For the subunits that adopt different conformations (orange and yellow), the double-headed arrow indicates the change between the two conformations. The RMSD between the subunits shown in orange/yellow is 6.9 Å, while the RMSD for the subunits shown in gray is only 1.3 Å. Alignments of only the CTDs are shown at left and right; in these alignments, the low RSMD values (0.9 Å and 1.0 Å, respectively) indicate that the CTDs undergo a hinge movement.

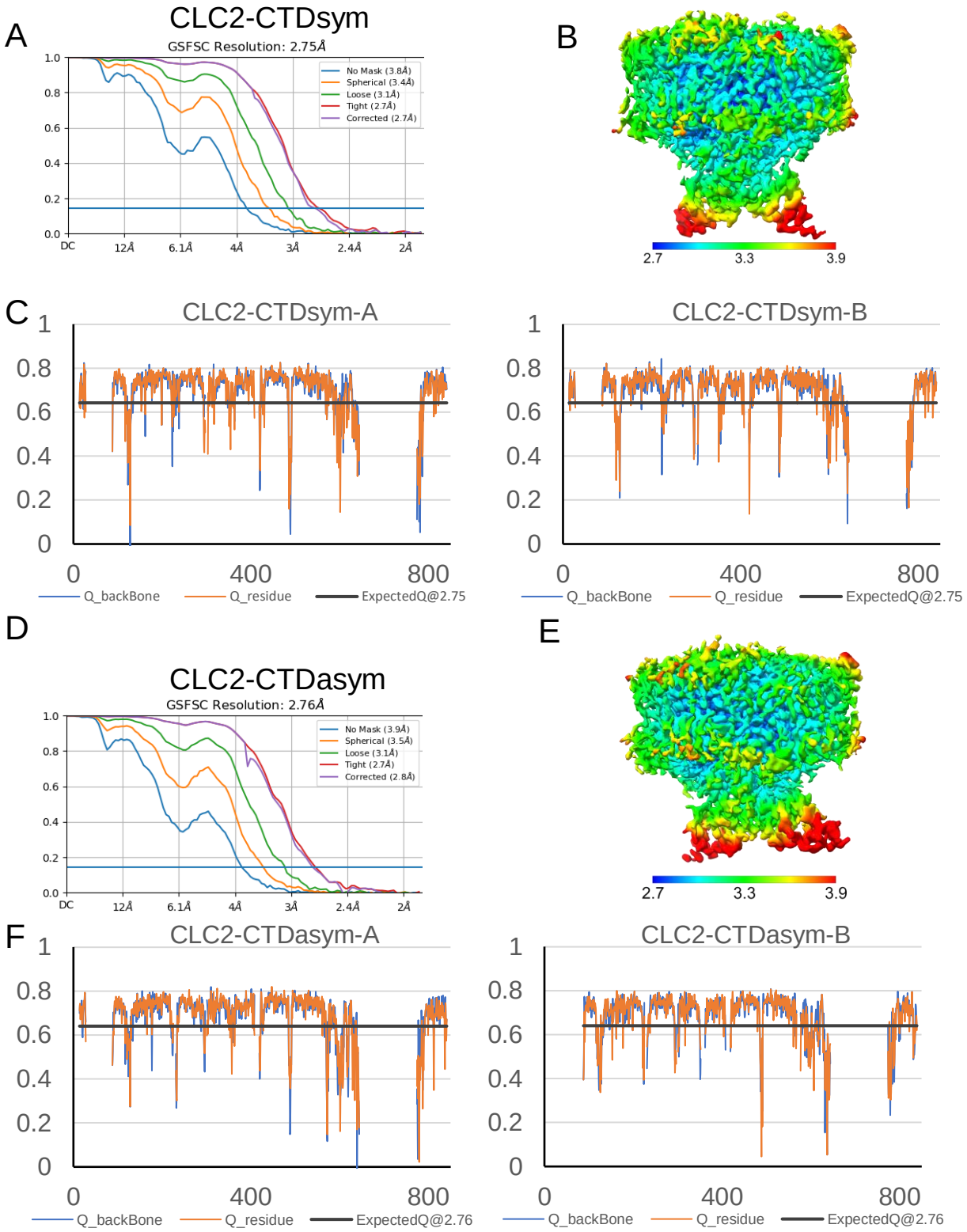

Figure 4 - figure supplement 1. Structure validation of CLC2-CTDsym and CLC2-CTDasym. (**A**) Gold standard FSC plots calculated in cryoSPARC for CLC2-CTDsym. (**B**) Local resolution of the cryo-EM map of the CLC2-CTDsym. (**C**) Model validation using Q-scores of subunit A (left) and subunit B (right) of CLC2-CTDsym. The black line represents the expected Q-score at respective resolution based on the correlation between Q-scores and map resolution. (**D-F**) the same as (**A-C**) for CLC2-CTDasym**.**

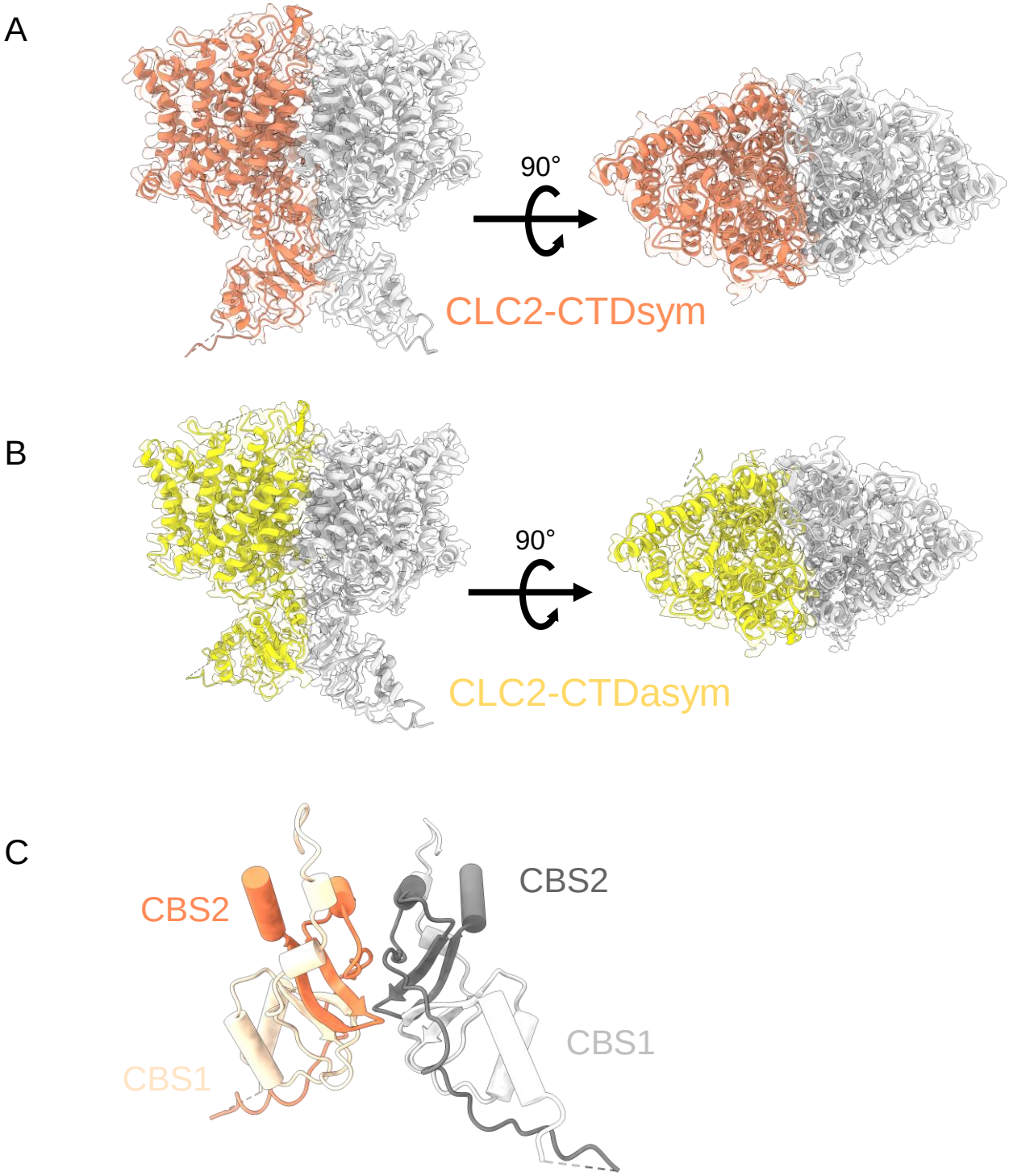

Figure 4 – figure supplement 2. CryoEM density maps for the two CTD-containing CLC-2 conformations, overlaid with structural models. (**A**) CLC2-CTDsym. (**B**) CLC2-CTDasym. Side view (left) and top view (right) are shown. (**C**) CTD of CLC2-CTDsym shows two CBS domains on each subunit (orange and light orange for subunit A; gray and light gray for subunit B).

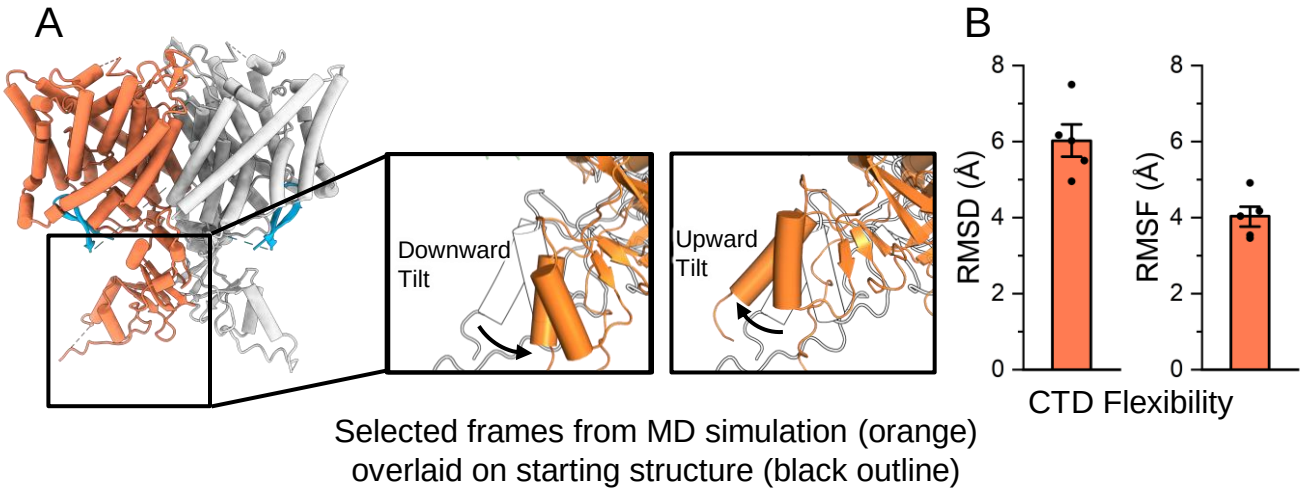

Figure 4 - figure supplement 3. MD analysis indicates conformational flexibility of the CTD. (**A**) The CTD is highly mobile relative to the transmembrane domain, and often tilts upward or downward relative to its initial location. In the inset images, two representative frames from simulation are shown (orange) overlaid on the starting structure (black outline). (**B**) The RMSD (root mean square deviation) and RMSF (root mean square fluctuation) of the cytoplasmic domain backbone were calculated after aligning frames on the transmembrane domains. Bars show the mean of five independent simulations, each 2.0 μs in length. Error bars are 68% confidence intervals of the mean.

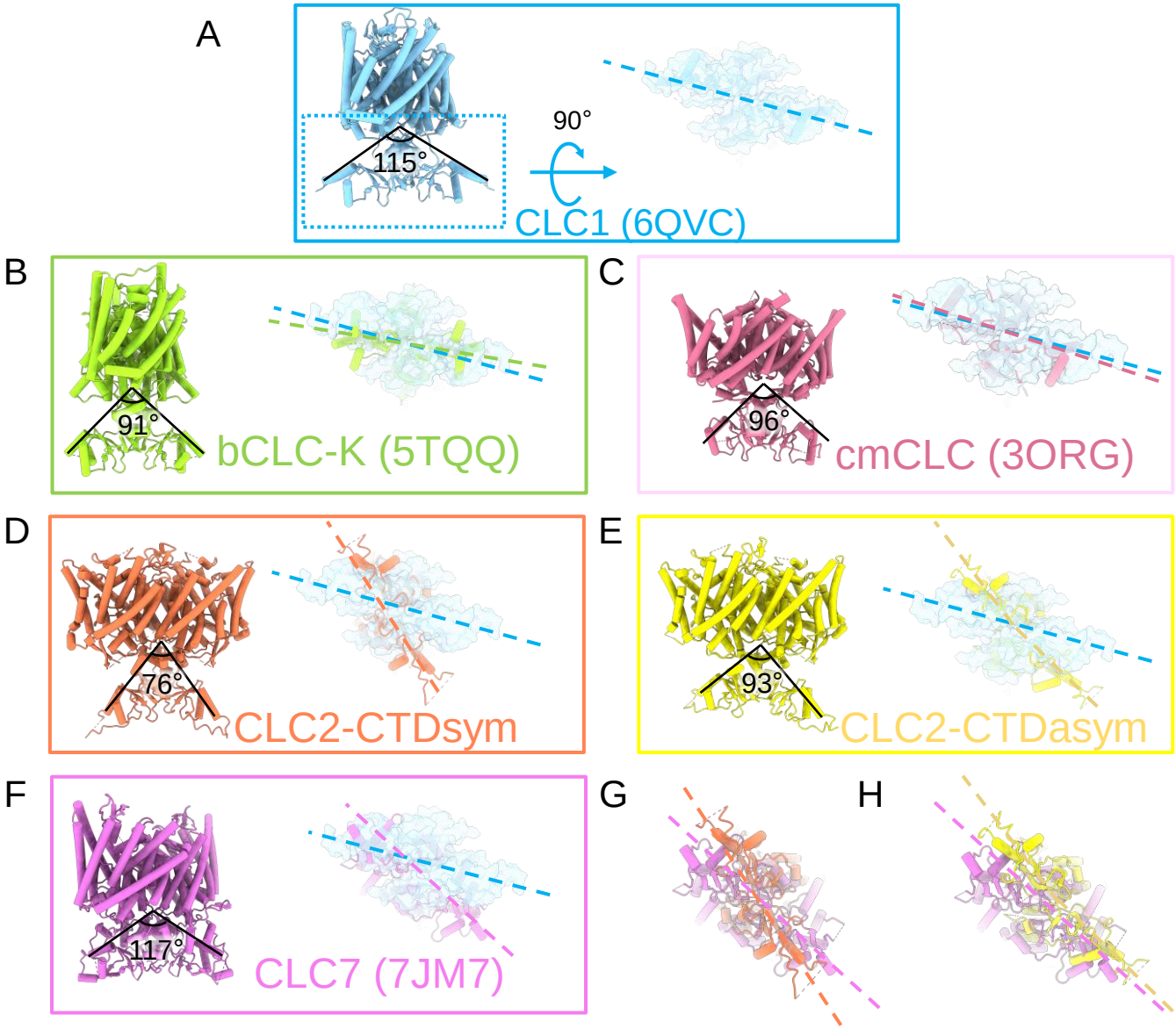

Figure 4 - figure supplement 4. Comparison of CTD orientation with respect to the TM domain. (**A**) The CLC-1 structure is shown in light blue. The angle of orientation for the CTDs was calculated using the far end residue of helix T (the second helix of first CBS domain) as the end point of rays and the center of the TM-CTD connecting plane as the vertex of the angle. On the right the CTD is shown in surface representation following rotation as indicated. Panels (**B**) – (**F**) show the CLC homolog indicated, with angles calculated as for CLC-1, and the rotated view of the CTD shown to compare the positioning of the CTDs relative to the membrane domains. The dashed lines indicate the long axes of the CTDs. In each panel, CLC-1 is shown in light blue as a reference for comparison. (**G**) and (**H**) overlays compare the CTD orientations in the CLC-2 structures to that in CLC-7. PDB IDs are shown in the parentheses. PDB IDs for CLC2-CTDsym and CLC2-CTD asym are 8TA4 and 8TA5.

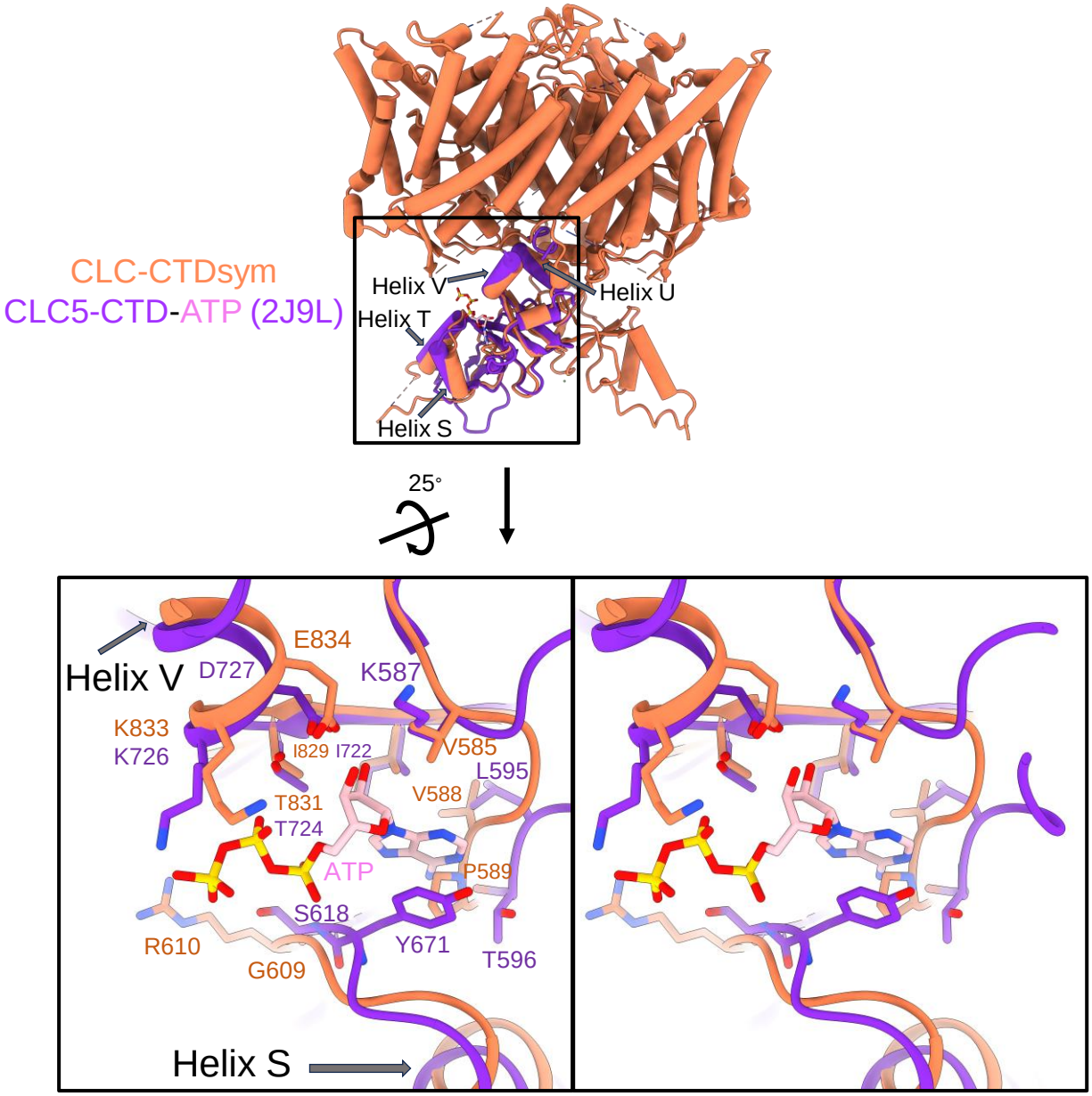

Figure 4 – figure supplement 5. ATP binding site comparison between CLC-2 and CLC-5. Top: Structural overlay of CLC2-CTDsym (in orange) and CLC5-CTD (in dark purple) with ATP (pink carbon atoms; CPK coloring on non-carbon atoms. PDB ID: 2J9L). Bottom: Zoomed in stereo view of ATP binding site in CLC5-CTD (dark purple) overlaid with the same region in CLC2-CTDsym (orange). Residue numbers are labeled in dark purple for CLC-5 and orange for CLC-2.

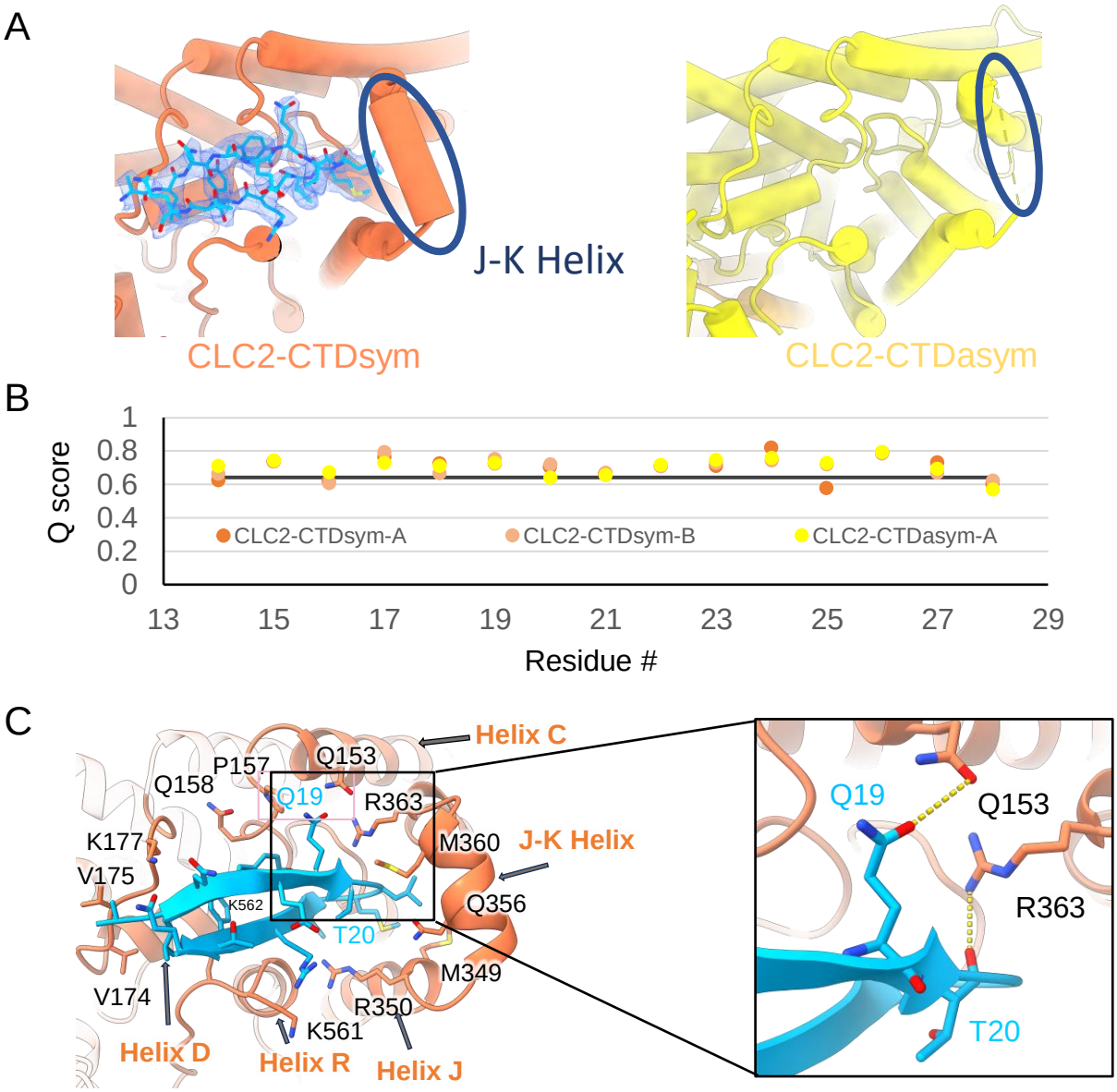

Figure 5. The blocking hairpin structure corresponds to an N-terminal sequence of CLC-2. (**A**). *Left:* The hairpin structure seen in the cryoEM density (blue mesh) fits N-terminal residues 14-28 (blue). *Right:* The subunit in CLC2-CTDasym structure that contains a CTD with rotated orientation lacks density for the hairpin structure. In this structure, the residues linking TM helices J and K are not resolved. The dark blue circles indicate this unresolved region (right panel) and the corresponding resolved J-K helix that occurs in the other subunits. (**B**) Model validation using Q-scores for the N-terminal hairpin: orange and light orange for subunits A & B of CLC2-CTDsymsubunit; yellow for subunit A (the hairpin-containing subunit) of CLC2-CTDasym. The black line represents the expected Q-score at 2.75 Å based on the correlation between Q-scores and map resolution. (**C**) Residues on the transmembrane domain interact with the N-terminal hairpin. The J-K helical linker and TM Helices C, D, R, and J are labeled with arrows. Inset: Zoomed-in view of two hydrogen bonds formed between the hairpin structure and the TM domain: Q19-Q153 and T20-R363. Mutation of these two residues (Q25 and T26 in rat CLC-2) generated an open-channel phenotype for CLC-2 expressed in *Xenopus* oocytes (Grunder et al., 1992).

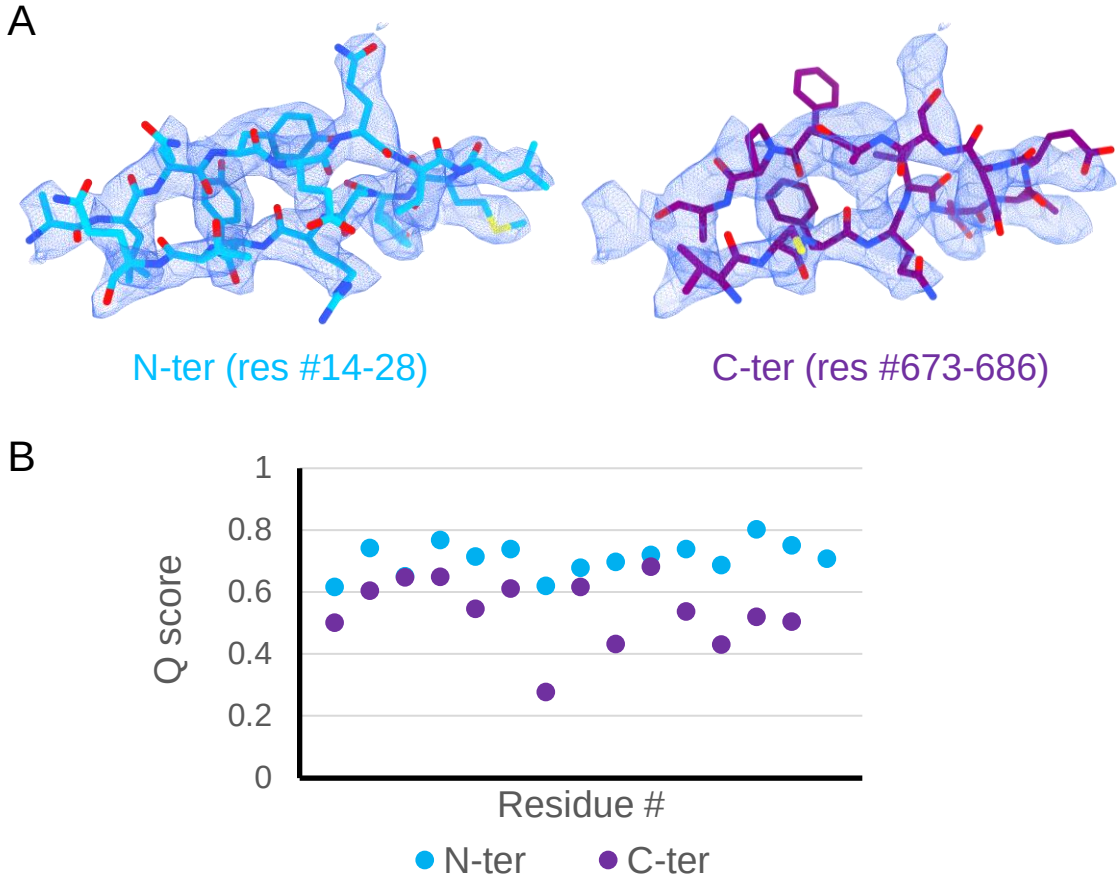

Figure 5 – figure supplement 1. Comparison of peptide candidates fitting into the hairpin density. (**A**) Best-fitting peptide candidate from the N-terminus (left shown in blue) and from the C-terminus (right shown in purple) fitted into cryoEM hairpin density (blue mesh). (**B**) Q-score plot of the two peptide candidates (residues 1-15 of the respective sequences). The Q-scores for the C-terminal peptide are generally lower than the Q-score expected for the corresponding resolution (0.65).

A

```
                    20        30        40        50
CLC2_HUMAN   EPRALQYEQTLMYGRYTQDLGAFAKEEAARIRLGGPEPWKGPPSSRAA
CLC2_RAT     EPRALQYEQTLMYGRYTQELGAFAKEEAARIRLGGPEPWKGSPSARAT
CLC2_MOUSE   EPRALQYEQTLMYGRYTQELGAFAKEEAARIRLGGPEPWKGSPSARAT
CLC2_RABBIT  EPRALQYEQTLMYGRYTQDLGAFAKEEAARIRLGGPEPWRSPPSPRTP
CLC2_CAVPO   EPRALQYEQTLMYGRYTQELGAFAKEEAARIRLGGPEPWKGPPSPRVP
CLC2_BOVIN   EPRALQYEQTLMYGRYTQDLGAFAKEEAARIRLGGPEPWRGPPSPRAP
CLC2_DROME   DDDPIGYIDTLMYGRYTKDLGEFAKDEARKLKILEKRRK..QEDKQRN
```

B

```
                 10        20        30
CLC2_HUMAN   AAEEGMEPRA.......LQYEQTLMYGRYTQD.....L......GAFAKE
CLC1_HUMAN   SENGGLQHRLRKDAGPRHNVHPTQIYGHHKEQ...............FSDR
CLCKA_HUMAN  ..................................................ME
CLCKB_HUMAN  ..................................................ME
CLC0_TORPEDO ...........................MSHEKNE...................
CLC3_HUMAN   FQTSEDDNLLDGDTAVGTHY..TMTNGGSINS...................
CLC4_HUMAN   .......................MVNAGAMSG...................
CLC5_HUMAN   FSMRDDVPPLDREVGEDK.....SYNGGGIGS...................
CLC6_HUMAN   ........................MAGC.........RGSLCCCCRWCCC
CLC7_HUMAN   RDDEEAAPLLRRTARPGGGT..PLLNGAGPGAARQSPRSALFRVGHMSSV

                 40        50        60        70
CLC2_HUMAN   EAARIRLGGP..EPW..KGPPSSRAAPELLEYGRSRCARCRVC.......
CLC1_HUMAN   E...QDIGMPKKTGS.....SST....V.DSKDEDHYSKCQDC.......
CLCKA_HUMAN  E....LVGLR..EGF..SGDPVT......L...QELWGPCPHIRR.....
CLCKB_HUMAN  E....FVGLR..EGS..SGNPVT......L...QELWGPCPRIRR.....
CLC0_TORPEDO .....ASGNPEAQSW..KAQEAM....LGVKTEVSRWRAVKNC.......
CLC3_HUMAN   ..STHLLDL.LDEPIPGVG........TYDDFHTIDWVREKCKDR.ERHR
CLC4_HUMAN   ..SGNLMDF.LDEPFPDVG........TYEDFHTIDWLREKSRDT.DRHR
CLC5_HUMAN   ..SNRIMDF.LEEPIPGVG........TYDDFNTIDWVREKSRDR.DRHR
CLC6_HUMAN   CGERETRTPEEL.TILGETQEEEDEILPRKDYESLDYDRCINDPYLEVLE
CLC7_HUMAN   ELDDELLDPDMDPPHPFPKEIPHNEKLLSLKYESLDYDNSENQLFLEEER
```

Figure 5 – figure supplement 2. N-terminal hairpin sequence is conserved in CLC-2, but not other CLCs. (**A**) Alignment of the N-terminal hairpin sequence (blue boxed) amongst different species. (**B**) Alignment of N-terminal hairpin sequence (blue boxed) amongst other human CLCs.

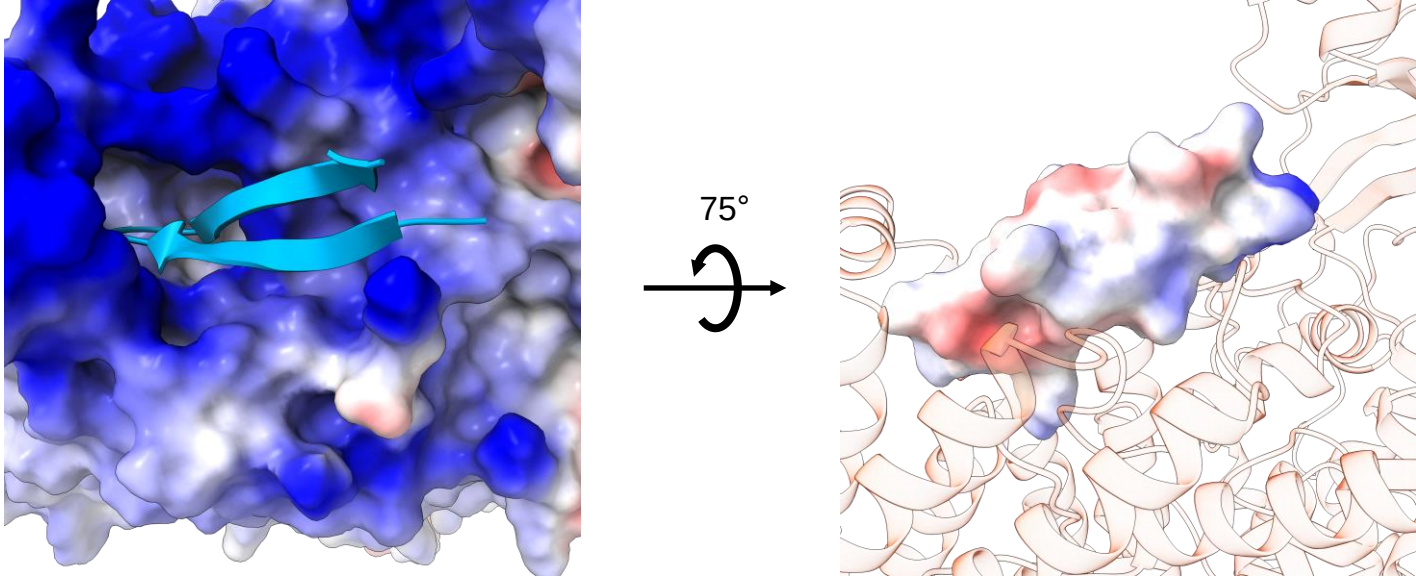

Figure 5 – figure supplement 3. Electrostatic map of the N-terminal hairpin blocking site. Left: view from the cytoplasm showing the electrostatic surface potential of the TM region (blue, positive; red, negative), with the hairpin shown in cartoon. Right: side view showing the electrostatic surface potential of the hairpin (blue, positive; red, negative) and the TM blocking site shown in transparent cartoon model.

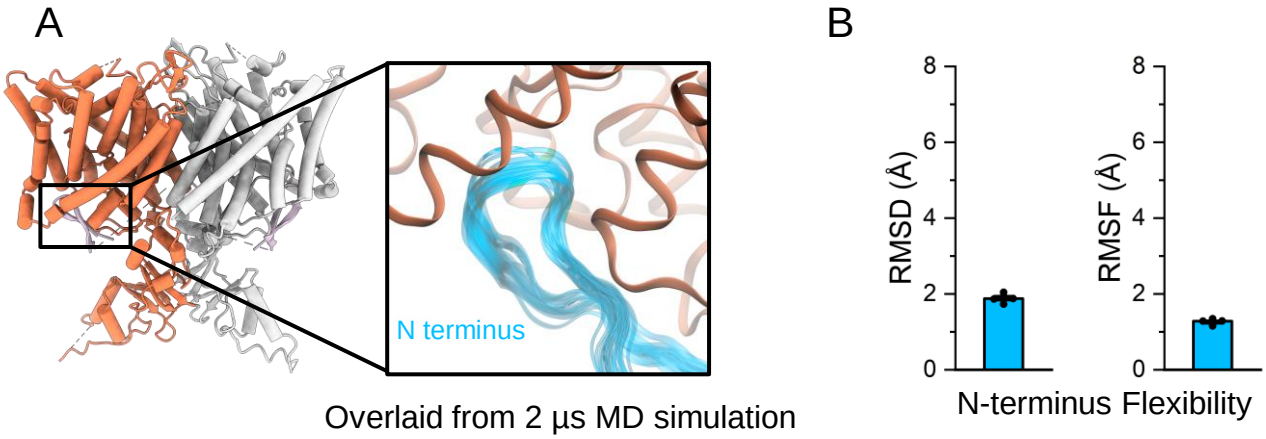

Figure 5 - figure supplement 4. MD simulations confirm the N-terminal hairpin structure is stable (**A**) In simulations, the N-terminus (blue) remains stably bound to the intracellular side of the transmembrane domain (orange). In the inset image, frames of the N-terminus taken every 200 ns from a representative simulation are overlaid. (**B**) The root-mean-square deviation (RMSD) and root-mean-square fluctuation (RMSF) of the N-terminus backbone were calculated after aligning frames on the transmembrane domains. Bars show the mean of five independent simulations, each 2.0 µs in length. Error bars are 68% CI (confidence interval of the mean).

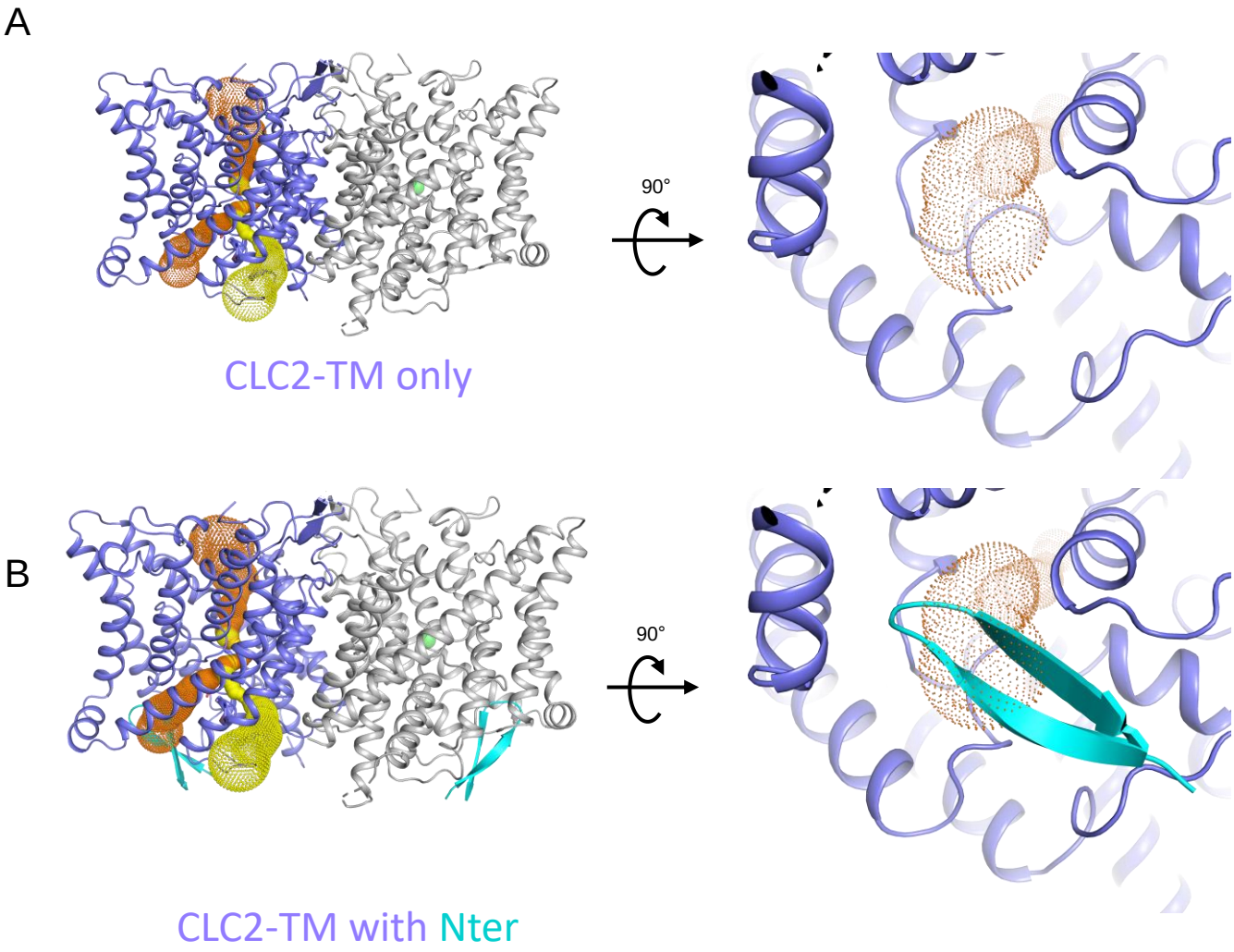

Figure 5 - figure supplement 5. The N-terminal hairpin blocks the primary Cl^- pore in CLC-2. (**A**) *Left:* Side view of CLC2-TM showing the caver-detected pore (primary in orange and secondary in yellow). *Right:* View of the primary pore from the intracellular side. (**B**) The N-terminal hairpin (blue) overlaid with CLC2-TM as shown in panel **A**.

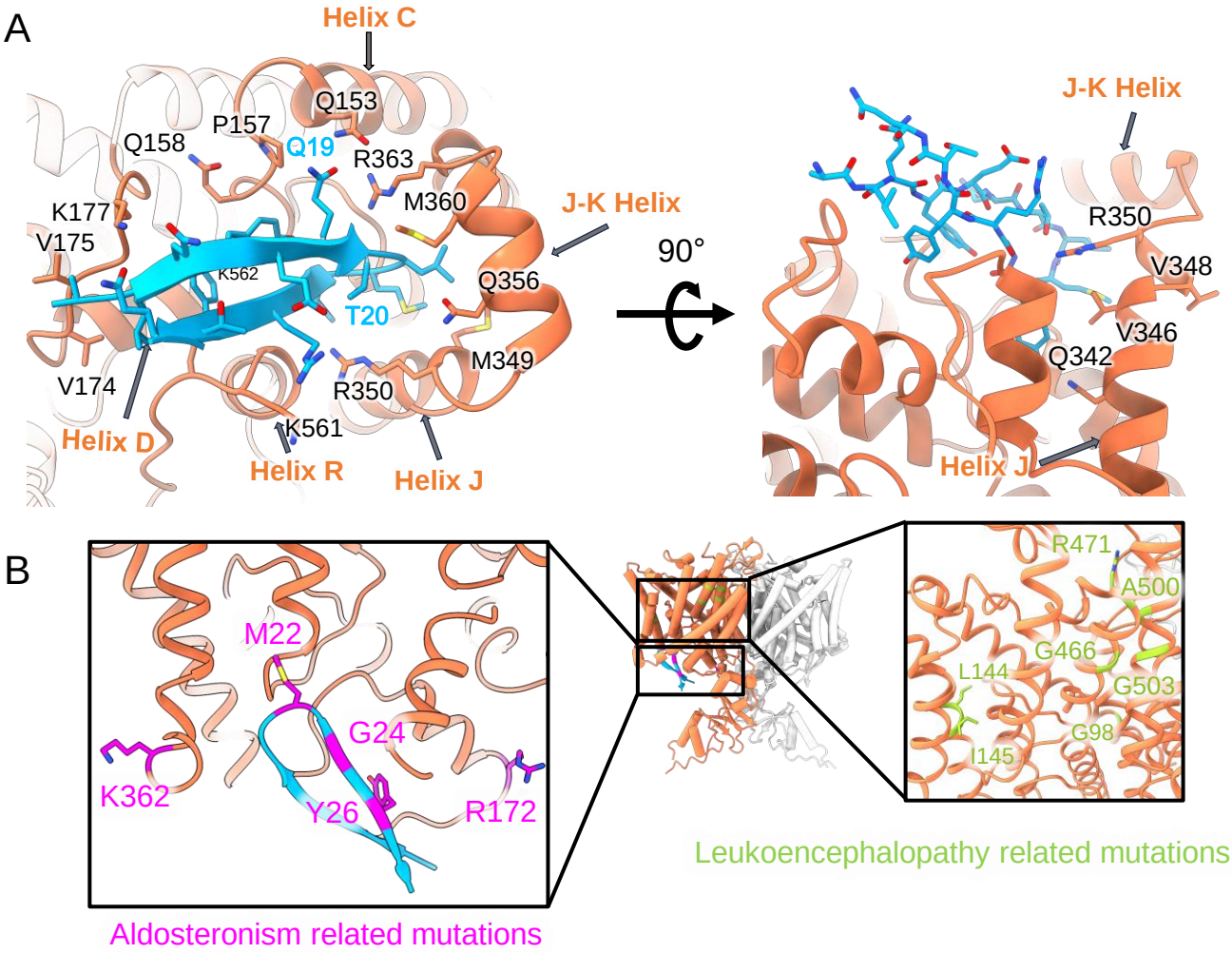

Figure 5 – figure supplement 6. Mapping mutant data onto the cryoEM structure. (A) Left: same as Figure 5C, showing hairpin interactions. Right: Rotated view highlighting ball "receptor" residues identified by Jordt and Jentsch, 1997. (**B**) Residues mutated in human Aldosteronism (Fernandes-Rosa et al., 2018, Scholl et al., 2018) and Leukoencephalopathy (Hector Gaitan-Penas., 2017) are shown on CLC2-CTDsym in magenta and green, respectively.

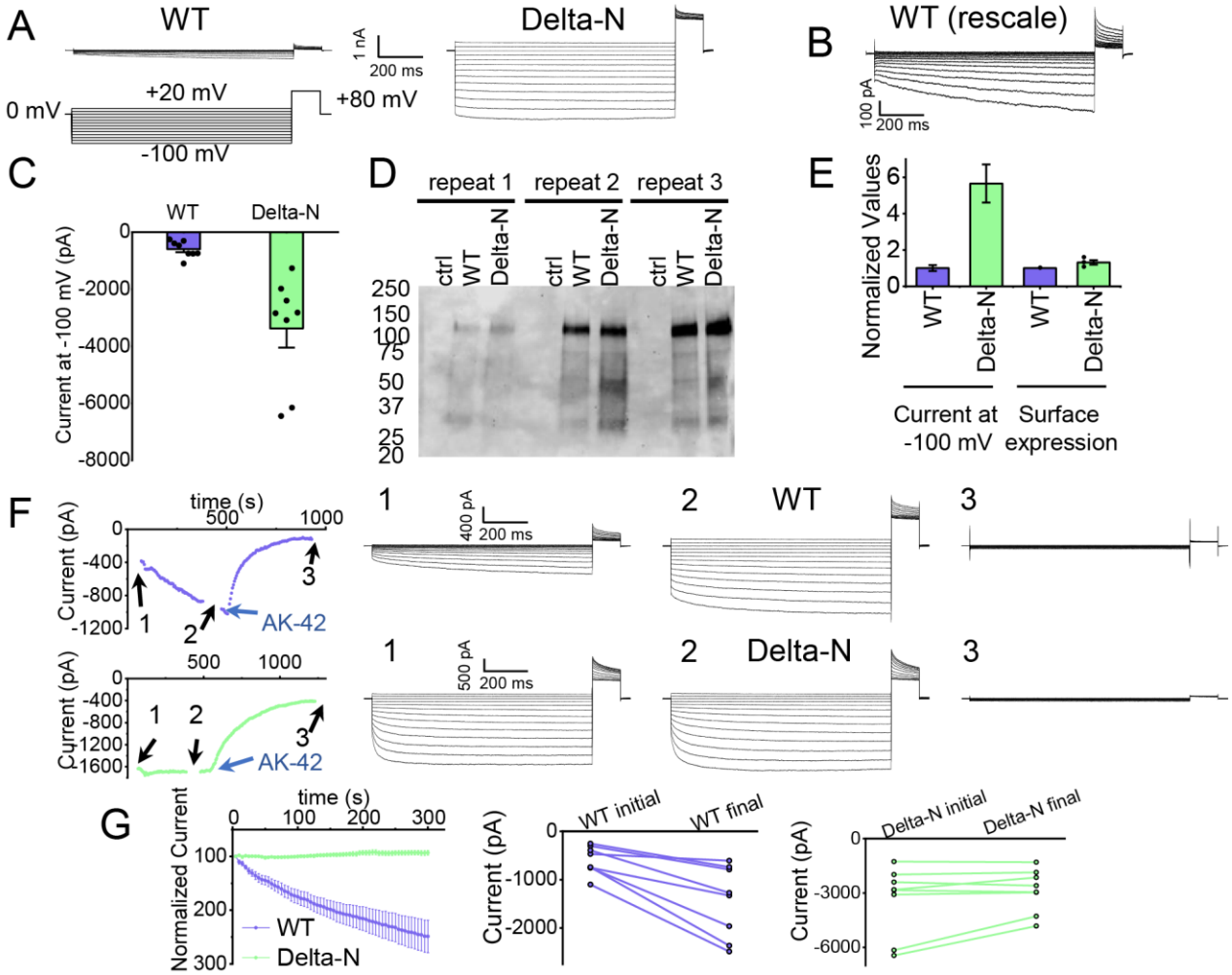

Figure 6 Patch-clamp experiments support CLC-2 channel block by the N-terminal hairpin structure. (**A**) Representative currents from WT and Delta-N CLC-2, recorded using the whole-cell patch clamp configuration in response to the voltage protocol shown. (**B**) WT CLC-2 recording from panel A, shown on an expanded scale. (**C**) Summary of current levels measured for WT and Delta-N CLC-2 at the end of the 1-s voltage pulse to -100 mV. Data are from six independent transfection samples, in each case with WT and Delta-N recorded on the same day following transfection. WT: -600 ± 102 pA (SEM, n=8);Delta-N: -3300 ± 630 pA (SEM, n=8). (**D**) Western blot detection of biotinylated surface-expressed CLC-2 from three independent experiments. (**E**) Summary data for electrophysiology and surface-biotinylation experiments. Points representing individual experiments for Delta-N surface biotinylation (each normalized to WT) are shown. Individual data points for the electrophysiology experiments are shown in panel C. (**F**) Representative examples of experiments to evaluate current run-up in WT and Delta-N CLC-2. *Left panels:* Time course data. Following an initial voltage-family measurement (I-V protocol as in panel A, taken at point "1"), currents were monitored by 1-s pulses to -100 mV every 5 s for five minutes, after which a second voltage-family measurement was made (point 2), followed by application of AK-42 to facilitate leak subtraction, and a final voltage-family measurement at point 3. I-V traces are shown at right. (**G**) Summary data for "run-up" experiments. *Left panel:* Normalized time-dependent currents for WT and Delta-N. Currents were first leak-subtracted (using the steady-state current after AK-42 application) and then normalized to the amplitude of the current measured in the first step of the 5-minute sequence. *Right panels:* Leak-subtracted current levels at -100 mV from "initial" and "final" IV traces measured at points "1" and "2' in the time course (panel F). Average initial and final currents (pA ± SEM, n=8) are WT: -600 ± 102 and -1400 ± 260; Delta-N: -3300 ± 630 and -2900 ± 420).

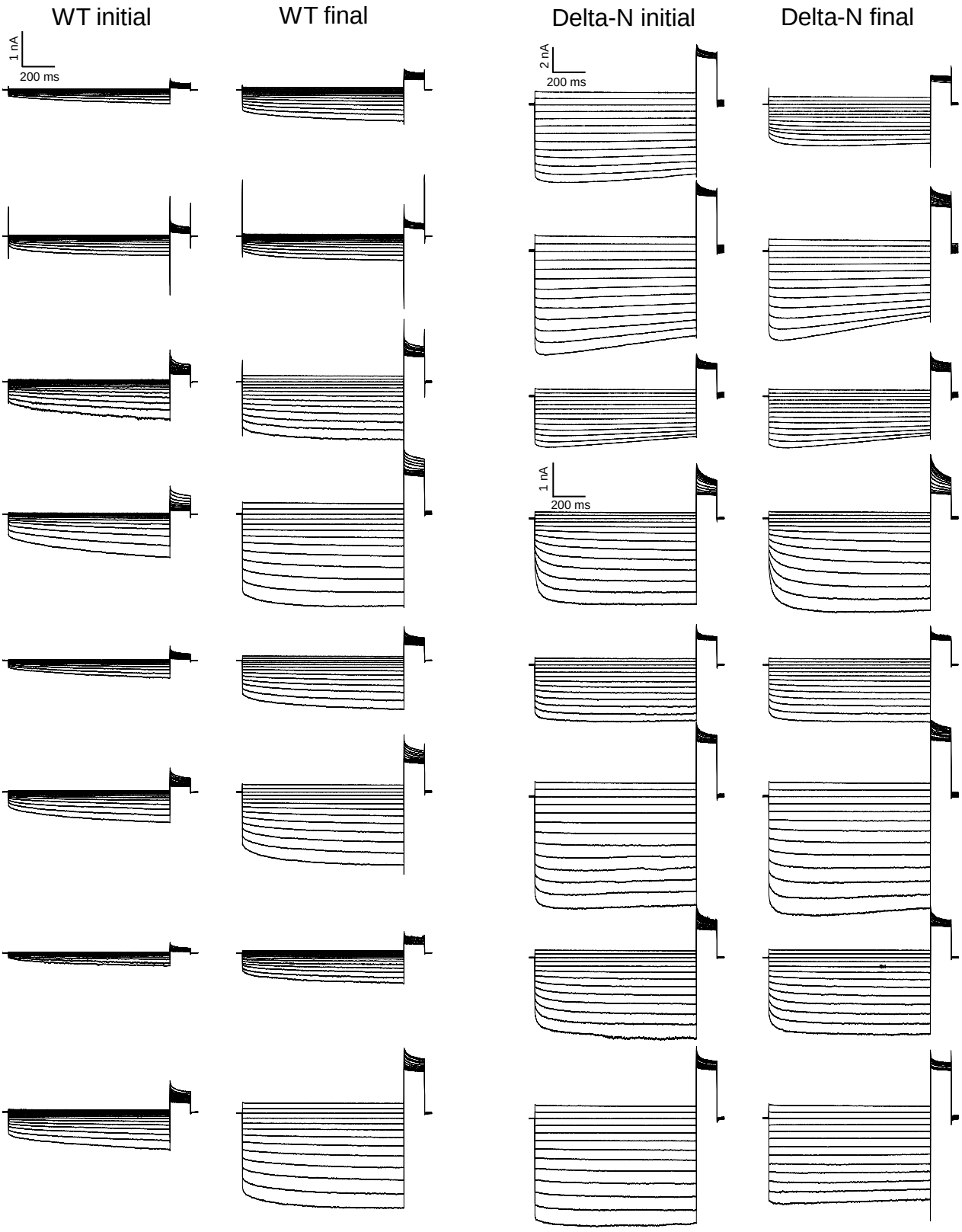

Figure 6 – figure supplement 1. Data traces from the CLC-2 run-up experiments summarized in Figure 6G. For Delta-N, separate scale bars indicate the currents for the top six and bottom 10 traces. AK-42 leak currents, not subtracted in these raw data traces, are summarized in Figure 6 – source data 1.

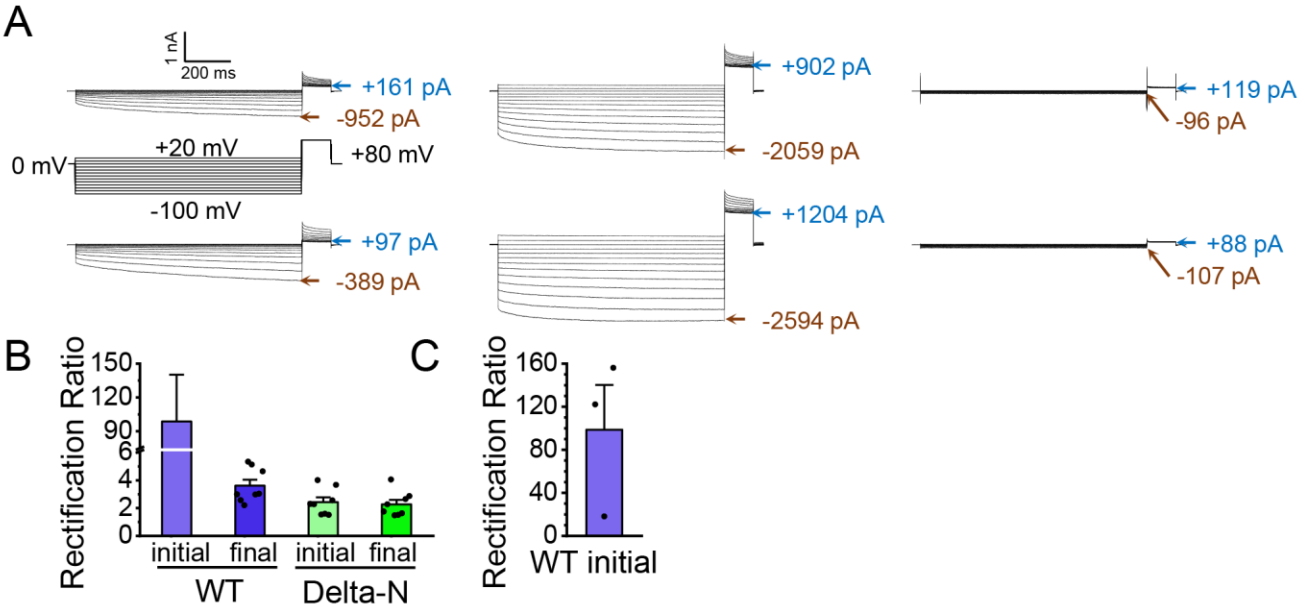

Figure 6 – figure supplement 2. CLC-2 current rectification. (**A**) Example traces from two experiments on WT CLC-2. Current values at end of the -100-mV test pulses and in the steady-state portion of the +80-mV tail pulse (following the +20-mV test pulse) are indicated. Robust AK-42 inhibition of the current at +80 mV indicates that CLC-2 is passing current at positive voltages. (**B**) Rectification ratios. Rectification was quantified by taking the ratio (absolute value) of the leak-subtracted currents at -100 mV and +80 mV. For WT initial currents, the low currents at +80 mV make this quantification challenging: for 5 out of 8 experiments on WT CLC-2, the AK-42 current at +80 mV was greater than the initial WT current at +80 mV, likely due to an increase in leak over the course of the experiment (~15 minutes of voltage pulsing). Therefore, the rectification calculated for the WT initial currents (99 ± 34, SEM n=3) has substantial uncertainty. That said, such high rectification is consistent with reports of CLC-2 rectification throughout the literature (Park et al., 1998; Arreola et al., 2002; Jentsch and Pusch, 2018). On the other hand, Delta-N currents display only mild rectification, which is straightforward to quantify given the high signal:noise (high AK-42-sensitive current relative to background), and which does not change in response to voltage pulsing. For “WT-final”, the rectification ratio similarly can be accurately quantified. Thus, while the high uncertainty and variance in estimating WT initial rectification precludes quantitative statistical comparisons, these data strongly suggest that WT CLC-2 current rectification decreases in parallel to current run-up. (**C**) WT initial rectification ratio from panel B replotted to show the individual data points from the 3 experiments in which AK-42 current at +80 mV was less than the initial WT current at +80 mV. Data for all experiments are summarized in Figure 6 – source data 1.

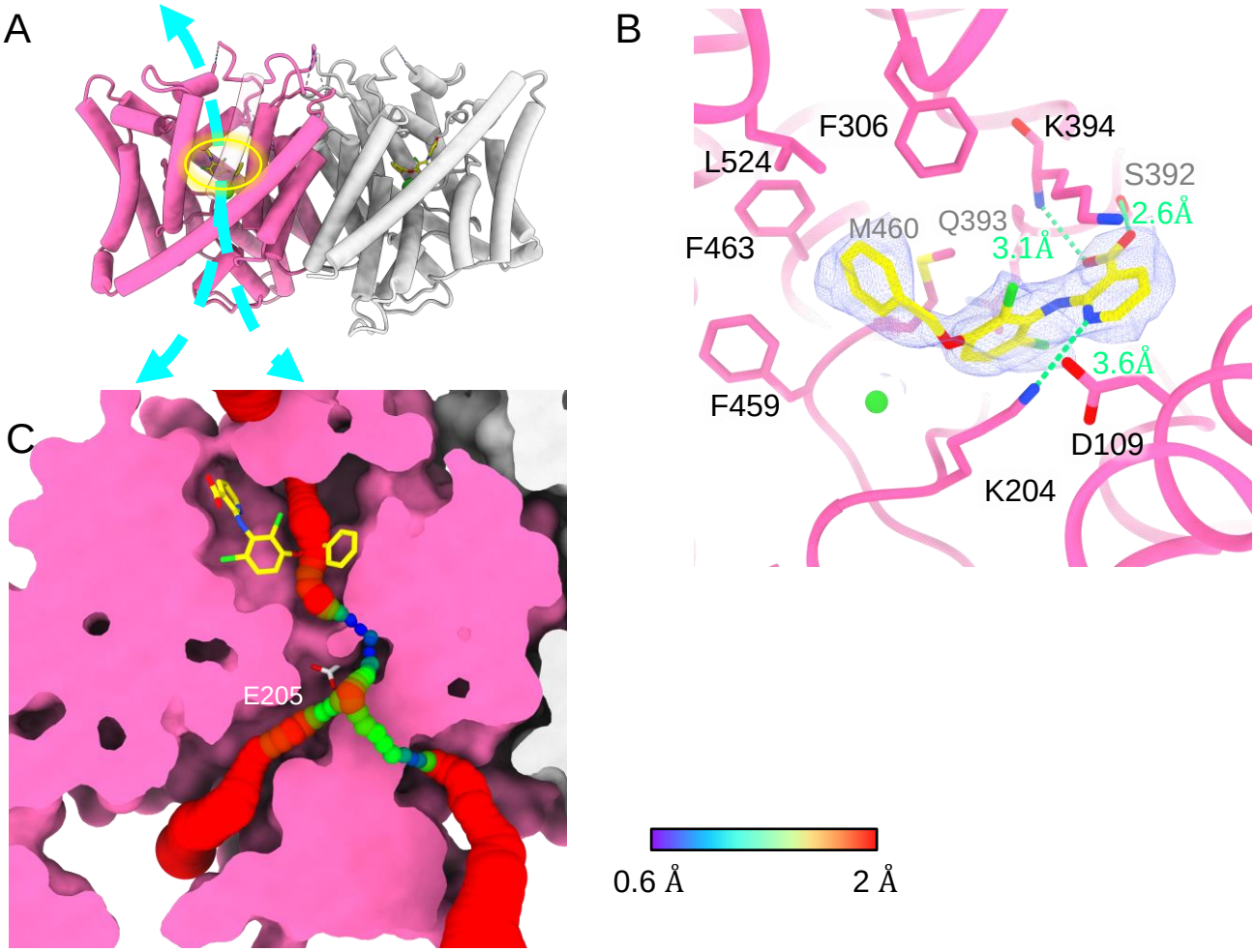

Figure 7 Bound AK-42 blocks the Cl^- pathway in CLC-2. (**A**) TM-domain structure of the CLC-2 structure in complex with AK-42 (CLC2-TM-AK42) at 2.74 Å. The identical subunits of the homodimer are shown in hot pink and gray; Cl^- ions are shown as green balls. Bound AK-42 is highlighted with a yellow circle on the pink subunit. The cyan arrow indicates the Cl^- pathway. (**B**) Zoomed-in view of the AK-42 binding site(contour level: 0.91, 6.0 σ). (**C**) A sliced view of CLC-2 showing AK-42 (yellow carbon atoms; CPK coloring on non-carbon atoms) and E_{gate} (CPK sticks). Both AK-42 and E_{gate} obstruct the Cl^- pathway, displayed as a color map.

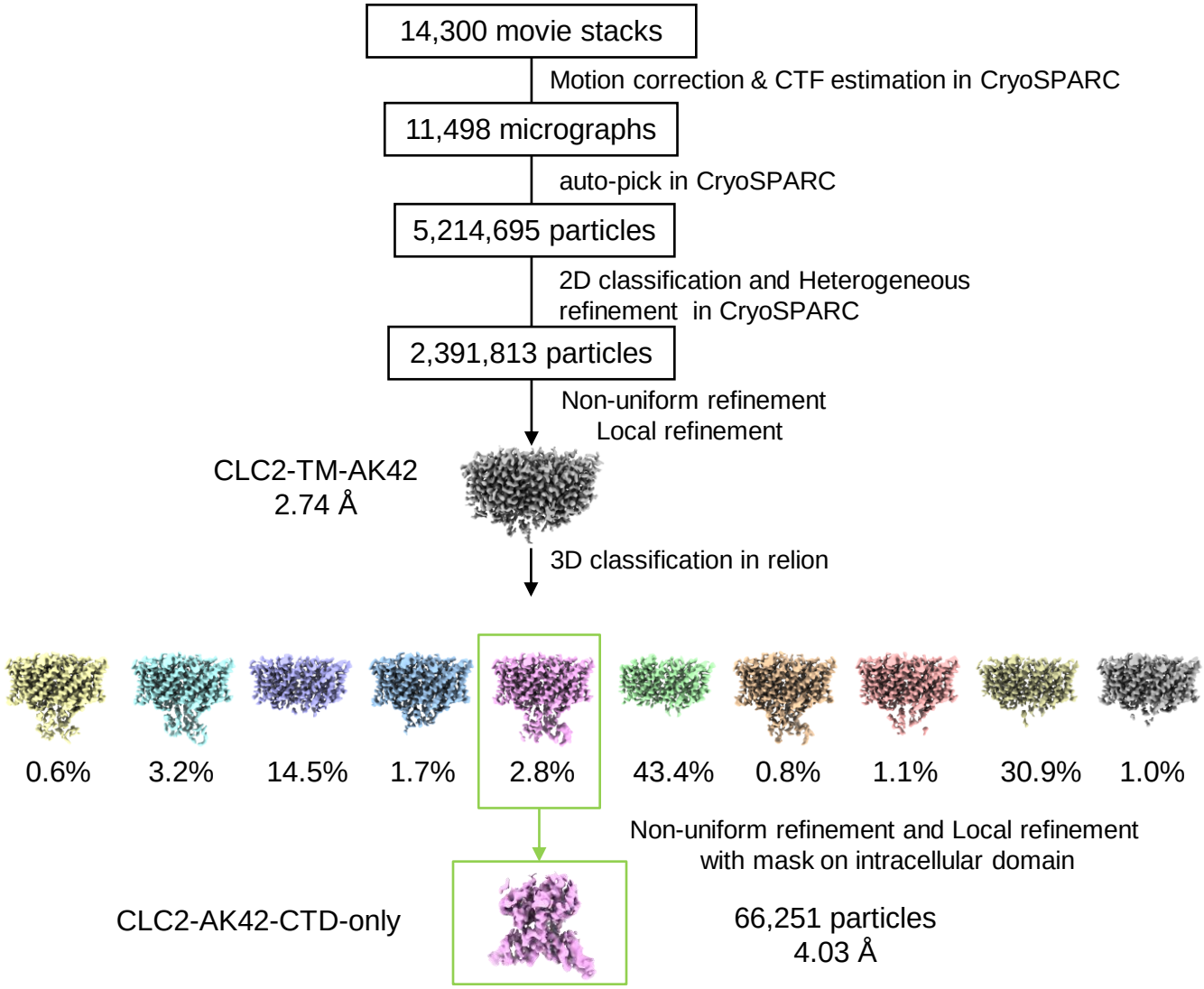

Figure 7 - figure supplement 1. cryoEM workflow of the CLC2-TM-AK42 single-particle cryo-EM data processing. A total of 14,300 movie stacks were collected on a 300 kV Titan Krios cryo-electron microscope. cryoSPRAC was used for 2D classification and CLC2-TM-AK42 density map was obtained after 2D classification. Relion was used for 3D classification.

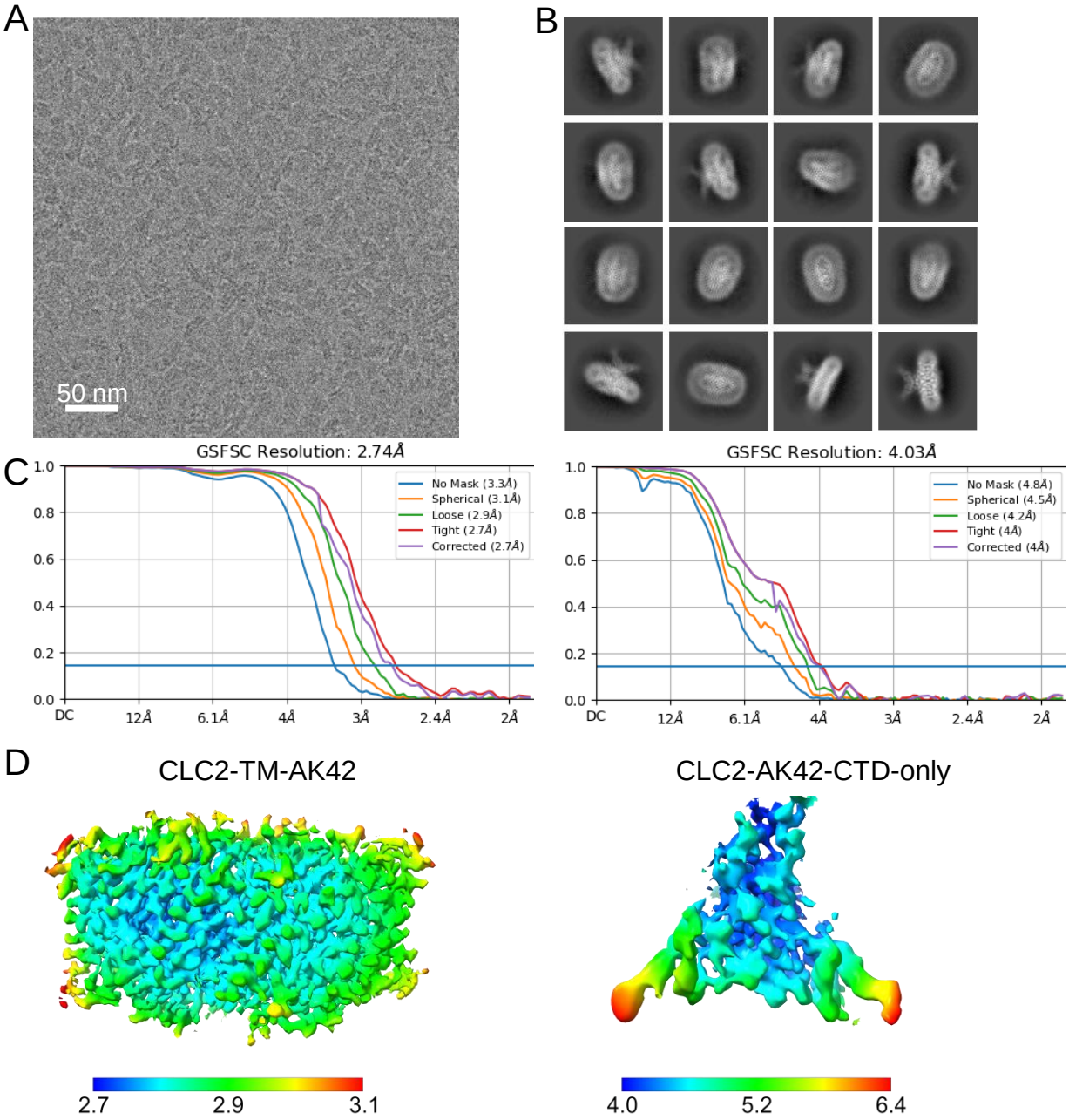

Figure 7 - figure supplement 2. Micrograph and 2D classes and structure validation of CLC2-AK42. (A) Representative motion-corrected cryo-EM micrograph. (B) 2D class averages. (C) Gold standard FSC plots calculated in cryoSPARC for CLC2-TM-AK42 (left) and CLC2-AK42-CTD-only (right). (D) Local resolution of the cryo-EM map for CLC2-TM-AK42 (left) and CLC2-AK42-CTD-only (right)

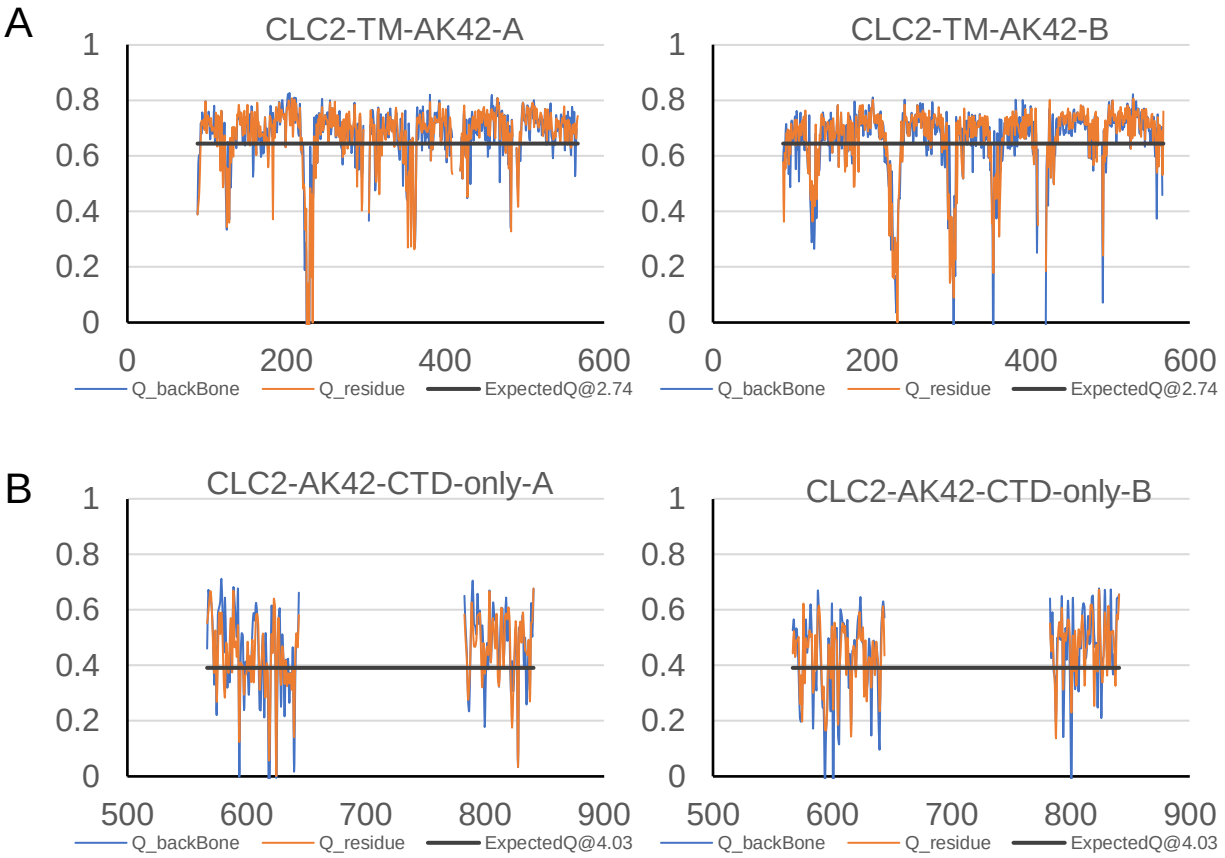

Figure 7 - figure supplement 3. Model validation using Q-scores. (**A**) Q-scores of CLC2-TM-AK42 for subunit A (left) and subunit B (right). (**B**) Q-scores of CLC2-AK42-CTD-only for subunit A (left) and subunit B (right). The black line represents the expected Q-score at respective resolution based on the correlation between Q-scores and map resolution.

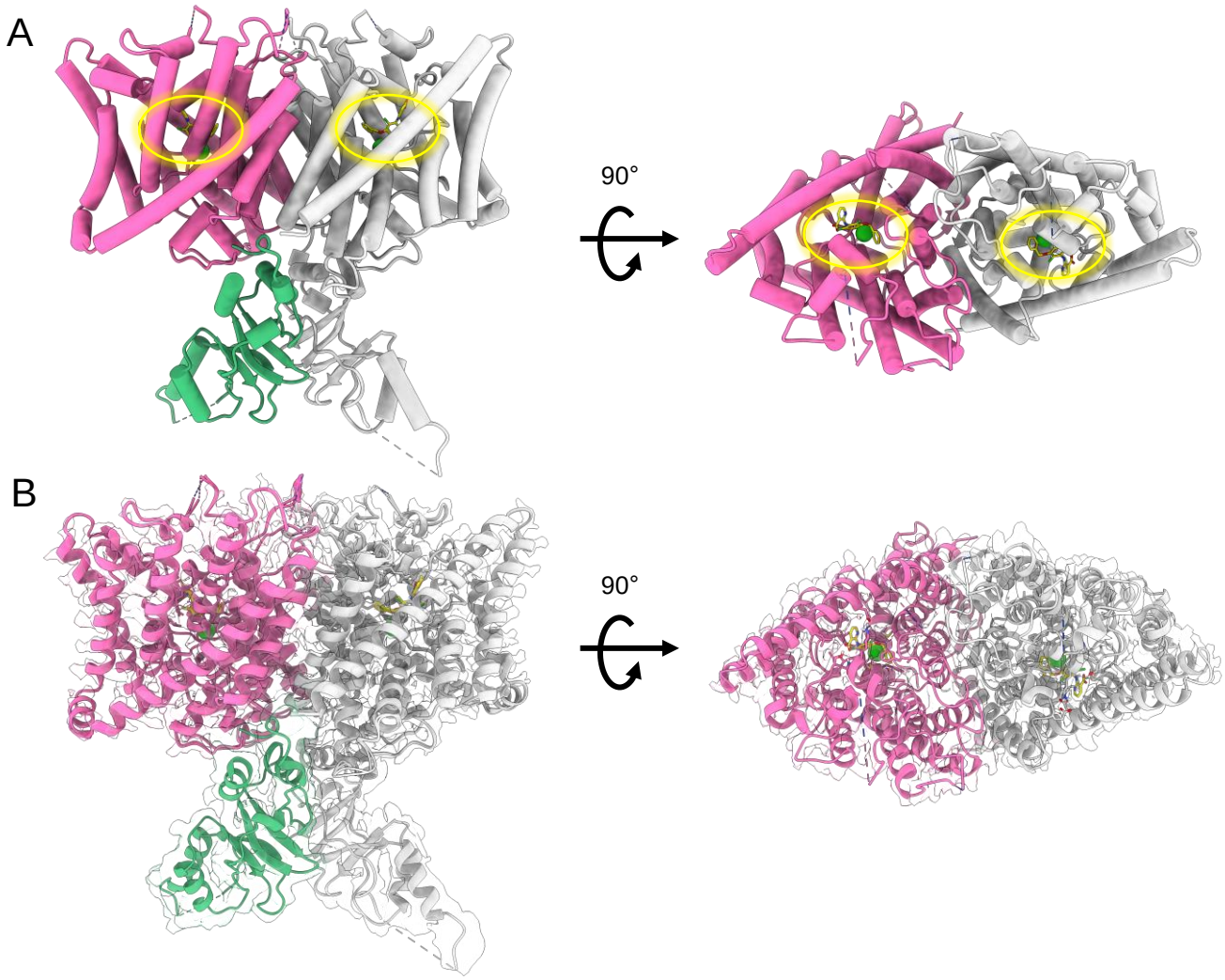

Figure 7 - figure supplement 4. cryoEM map and structure of CLC2-AK42. (**A**) cryoEM model of CLC2-TM-AK42 with docked CTD. The transmembrane region is shown in hot pink and gray. The CTD is shown in green and gray. AK-42 is shown in yellow and highlighted by yellow circles. Chloride ions are shown in green. (**B**) cryoEM model overlay with density map of CLC2-AK42. Contour level: 0.83, 6.8 σ (TM region); 0.35, 14 σ (CTD).

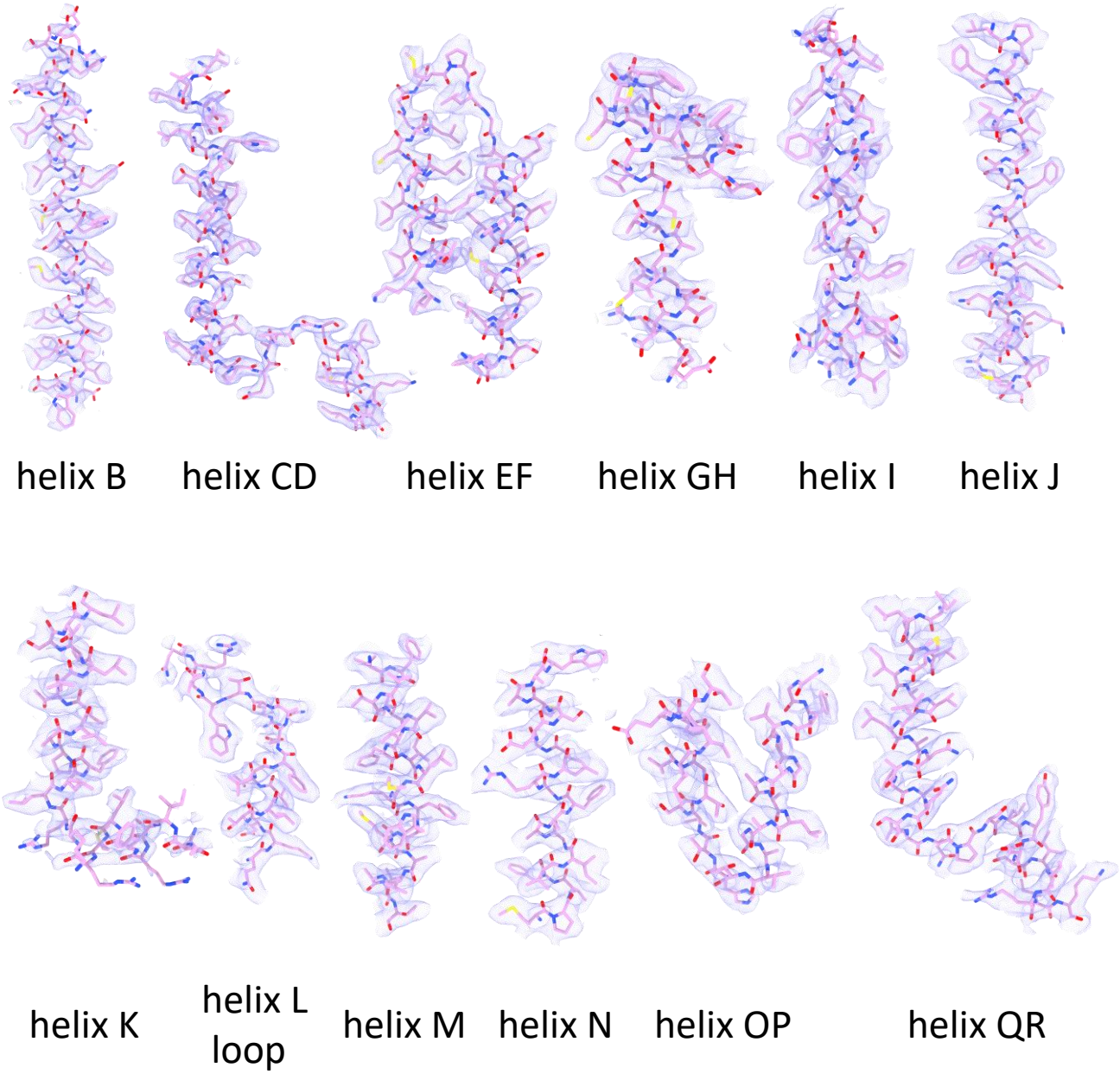

Figure 7 - figure supplement 5. Helix map of CLC2-TM-AK42. cryo-EM densities and model of CLC2-AK42 transmembrane helices (contour level: 0.52, 3.4 σ).

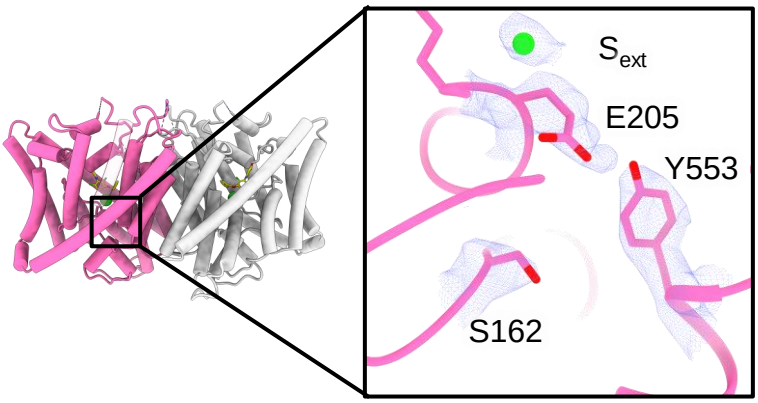

Figure 7 – figure supplement 6. Density overlay at key Cl^--pathway residues. Zoomed-in view highlighting residues S162, E205, Y553, and the bound chloride ion, with cryoEM density overlay (contour level: 1.4, 9.0 σ).

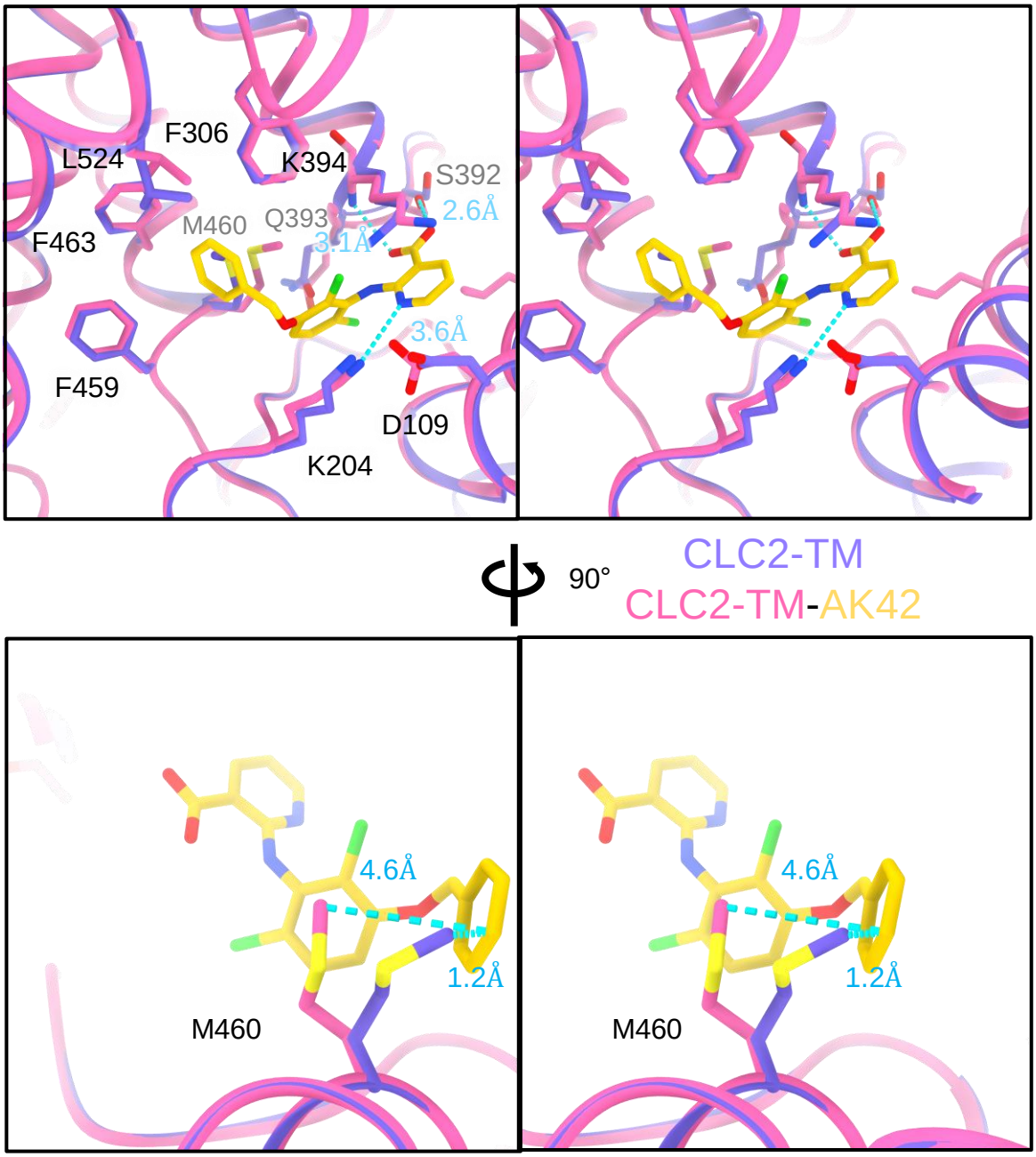

Figure 7 - figure supplement 7. AK-42 binding site comparison between CLC2-TM and CLC2-TM-AK42. Top: Stereo view of structural overlay at the AK-42 binding site. Hydrogen bonds between AK-42 and residues K204,S392,K394 are indicated by blue dashed lines. Bottom: A view highlighting the movement of residue M460 to make space for AK-42.

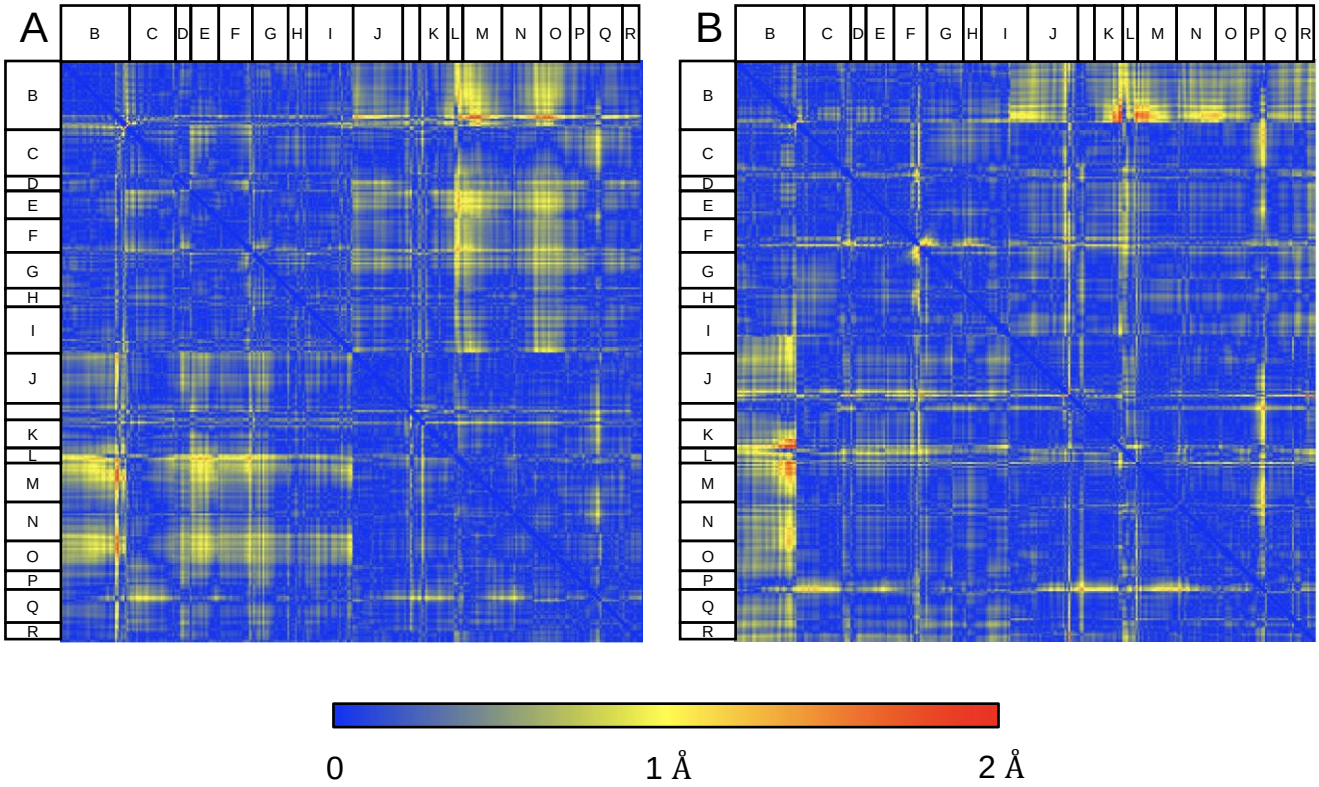

Figure 7 - figure supplement 8. Structural comparison of CLC2-TM and CLC2-TM-AK42. Difference distance matrices comparing Cα residues on TM helices between CLC2-TM and CLC2-TM-AK42 in subunits A (**A**) or B (**B**). Residues in loops connecting helices, where there is low confidence in the model building (Q score lower than the expected Q score of 0.65), were omitted from the matrices.

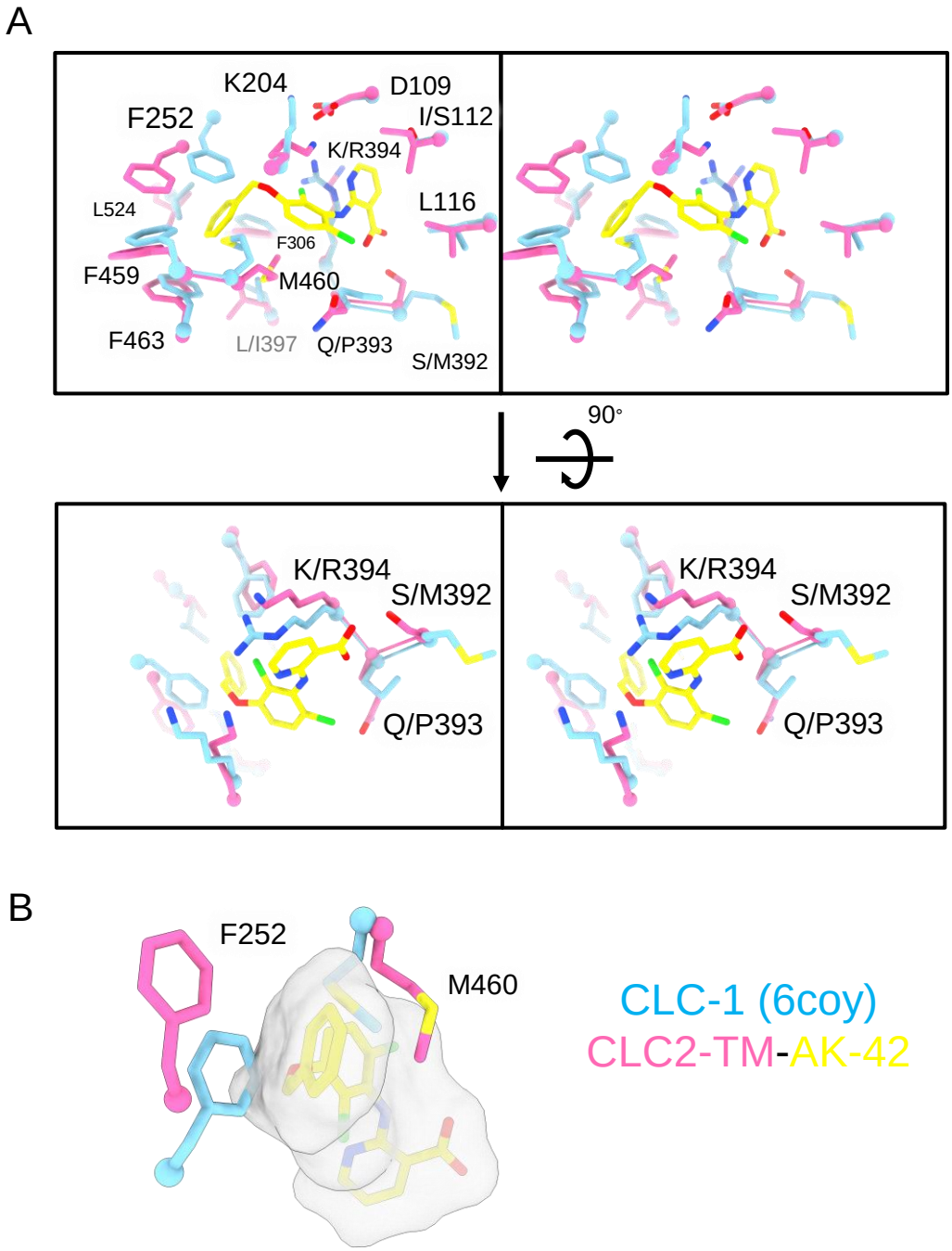

Figure 7 - figure supplement 9 AK-42 binding site comparison between CLC-2 and CLC-1. (**A**) Top: Stereo view of the AK-42 binding site in CLC2-TM-AK42 (hot pink) overlaid with the same region in CLC-1 (blue, PDB:6coy). Residue numbers correspond to those of CLC-2. The five residues that differ between CLC-2 and CLC-1 are: I112 (S139), S392 (M419), Q393 (P420), K394 (R421), and L397 (I424). Bottom: Rotated (stereo) view of AK-42 binding site to compare residues S392, Q393 and K394 in CLC-2 versus M419, P420 and R421 in CLC-1. These three were calculated to contribute most significantly to the AK-42 binding energy (Ma, 2023). (**B**) Residues in CLC-1 predicted to clash with AK-42. AK-42 is shown in yellow sticks and white surface. F252 and M460 in CLC-2 correspond to F279 and M485 in CLC-1.

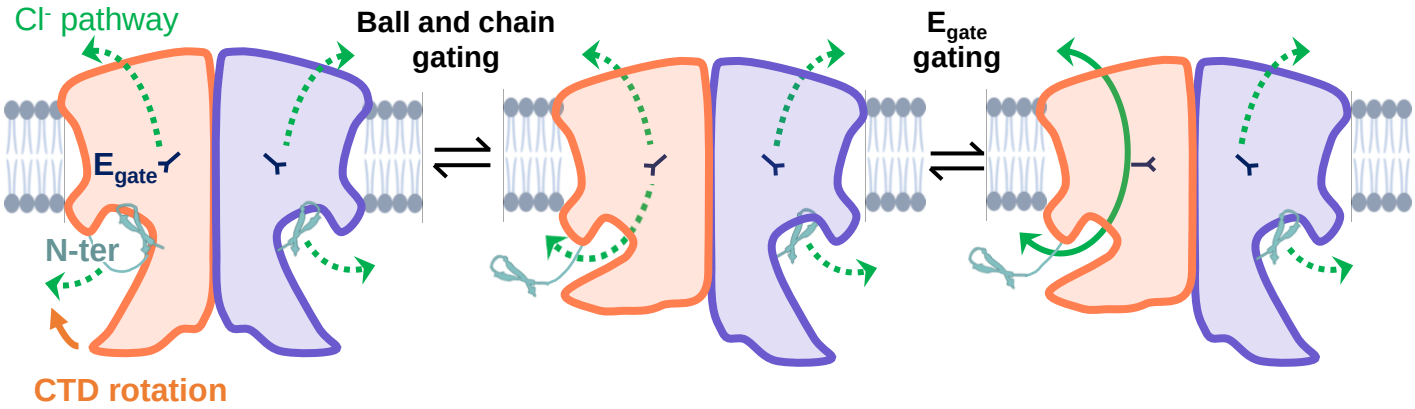

FIGURE 8: CLC-2's gating is illustrated based on our new structural data. Opening of each protopore requires at least two events – unblock by the N-terminal hairpin ("N-ter") and rotation of E_{gate} away from the permeation pathway. The dashed green arrow represents the Cl^- conduction pathway. Hairpin unblock (ball and chain gating) is coupled to conformational change of the CTD: rotation of the CTD towards the membrane precludes hairpin binding, thus facilitating channel opening. Opening of the channel pore following these two events is depicted for one subunit of the homodimer (filled green arrow).